Offshore Methane Pyrolysis

A techno-economic analysis to assess the feasibility of offshore methane pyrolysis for the production of hydrogen

A. Stroo

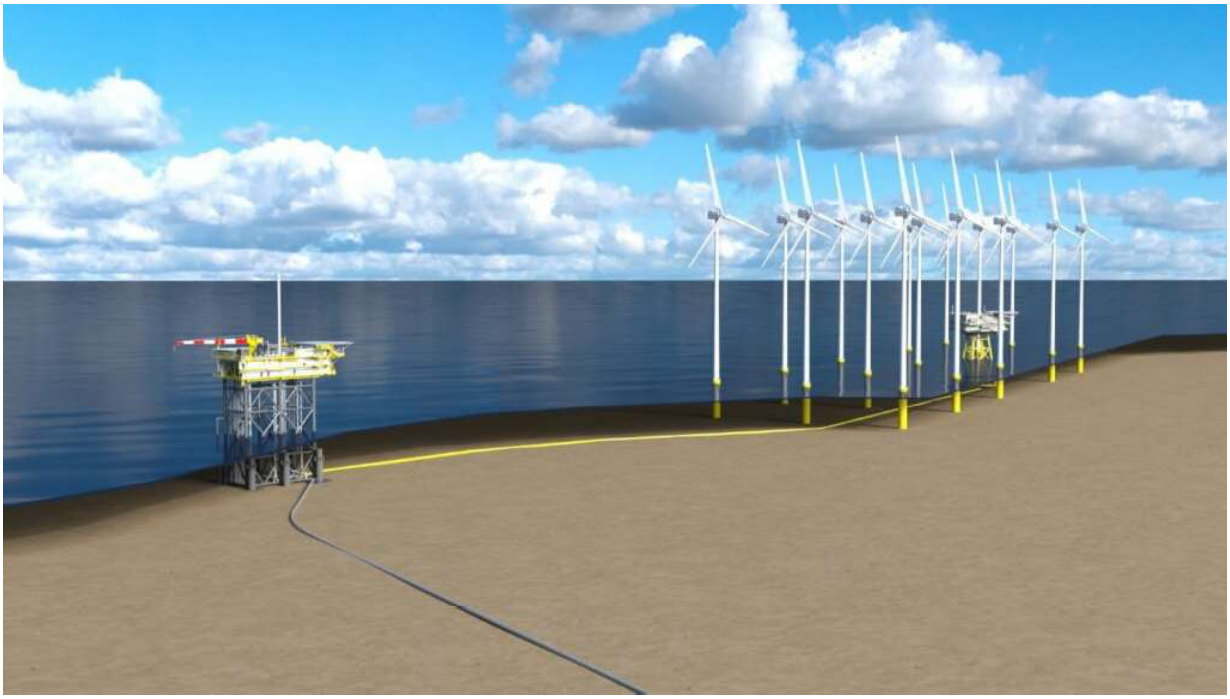

TU Delft

one dyas

Offshore Methane Pyrolysis

A techno-economic analysis to assess the feasibility of offshore methane pyrolysis for the production of hydrogen

Thesis report

by

A. Stroo

to obtain the degree of Master of Science
at the Delft University of Technology
to be defended publicly on January 26, 2023 at 12:30

Thesis committee:	
Chair:	Dr. A.J.M van Wijk
Supervisor:	Dr. ir. E.L.V. Goetheer
Quality control:	Ir. A.C.M. van der Stap
Company supervisor:	Ir. C.I. van Wijk
Place:	Faculty of 3mE, Delft
Student number:	4492471

An electronic version of this thesis is available at `http://repository.tudelft.nl/`.

Cover image: Render of N05-A and the connection to the Riffgat offshore windfarm by ONE-Dyas

Delft University of Technology

Preface

Throughout the course of my studies, my interest has been sparked the most by the global energy system and large scale energy transition opportunities there are offshore. Therefore, for me personally, it was no surprise my Master Offshore and Dredging Engineering at the Delft University of Technology would come down to a thesis on offshore hydrogen production.

I would like to thanks my graduation committee for their guidance, feedback and expertise during the entire course of the thesis. I also had the pleasure to execute this project in collaboration with ONE-Dyas and especially Colin van Wijk. Many thanks for all advise and discussions we had over the past months, they have been vital to the final product.

At last, I would like to express my appreciation for all friend and family that have supported me along the way. A special thanks goes to the people who have helped with the report by proofreading and giving their input. Papa I would like to thank you for all extensive hours of proof reading, they pushed the report to a higher level. Erik for constant availability for discussions and feedback. Bart for his advice on structuring of the report and last Charlotte for the enjoyable last two weeks in the library.

Abstract

Methane pyrolysis is a relatively new technology for producing hydrogen from fossil fuels that has the potential to greatly reduce the CO2 emissions of sustainable hydrogen production on a large scale. This is because hydrogen production via methane pyrolysis generates solid carbon instead of gaseous, thereby inhibiting emissions and the process energy demand is relatively low. Next to the production also transportation of sustainable hydrogen is also important enabler for a hydrogen economy and using existing offshore natural gas pipeline infrastructure could help make the market more competitive. This research aims to investigate the feasibility of offshore methane pyrolysis to contribute to both the potential of hydrogen production and transportation.

In order to investigate the feasibility of offshore methane pyrolysis for sustainable hydrogen production, a three-step approach will be taken. Firstly, a model will be developed to evaluate the potential for converting methane into hydrogen under various design scenarios. Secondly, the model will be utilized as tool to create an offshore design for the methane pyrolysis reactor, which will include not only the reactor units responsible for converting methane into hydrogen, but also any necessary auxiliary equipment to make offshore methane pyrolysis technically feasible. The offshore design will finally determine the performance of the facility in terms of size. Finally, a calculation of the levelized cost of hydrogen for the offshore design will be conducted to compare the concept with conventional reforming technologies for hydrogen production and identify the conditions required for offshore methane pyrolysis to be cost competitive.

The development of a design tool for an offshore methane pyrolysis installation necessitated the replication and extension of a coupled hydrodynamic and kinetic model originally. This was accomplished in order to simulate the conversion rate of the installation and to account for the initial small bubbles that occur at the bottom of the reactor. Additionally, the model was also evaluated for molten salt as a reactor fill and it was determined that the model did not apply in this region.

The resulting design tool was then utilized to create an offshore design for the methane pyrolysis reactor and to determine the performance of the facility. Two designs were constructed to meet the methane conversion requirements within the limitations of the N05-A platform that was used as case. The design with the highest number of columns was found to be the most efficient, however, the auxiliary equipment required a significantly larger deck space than the reactor units responsible for the conversion. The least amount of extra deck space did require the equivalent of the offshore platform used for gas production and processing.

The performance of the designed reactor units and the necessary deck space were the base of an economical model that accessed the levelized cost of hydrogen for offshore methane pyrolysis based on the production flow of the gas platform N05-A. The offshore design with the least amount of installations offshore showed to be the least expensive option. However to be cost-competitive with conventional hydrogen production from natural gas, the LCOH

should be decreases. The sales of the carbon product, produced as by-product during methane pyrolysis, would be the most promising approach. Also, a governmental action like a CO_2 tax works, as it would increase the LCOH of conventional hydrogen technologies, whereas offshore methane pyrolysis is not affected by this measure. One of the scenarios resulting from the sensitivity analysis on the LCOH, was a CO_2 tax of 50€/mt CO_2 in combination with a carbon value of 29 €/mt C_s.

The separation and handling of the carbon stream offshore in the end will determine the quality of the carbon product, however this process and also the marketability of the carbon product in large quantities hold various uncertainties. It would be recommended to further investigate these to narrow down the solution space and bring back the LCOH of offshore methane pyrolysis to conventional.

Table of Content

Nomenclature

List of abbreviations

ATR	autothermal reforming
BOE	barrels of oil equivalent
CAPEX	capital expenditure
CCS	carbon capture and storage
DWT	deadweight tonnage
EC	European Commission
EU	European Union
GEMS	Gateway to the Ems (area of small fields both in the Dutch and German parts of the North Sea)
LCOH	levelized cost of hydrogen
LMP	Larson Miller parameter
NGT	NoordGasTransport (-pipeline)
OPEX	operational expenditure
PEM	Polymer electrolyte membrane electrolysis
PSA	pressure swing adsorption
SSCM	standard cubic centimetre per minute
SMR	steam methane reforming
UTC	unit technical cost
WACC	weighted average cost of capital

List of Chemicals

Bi	Bismuth
Br	Bromine
C	Carbon
CH_4	Methane
Cl	Chlorine
CO_2	Carbon dioxide
Cr	Chrome
Cu	Copper
H	Hydrogen
H_2	Hydrogen
K	Potassium
N	Nitrogen
N_2	Nitrogen
Na	Sodium

List of symbols

symbol	description	unit	Ref/formula
$\sum_{i(g)} v_i$	sum of the stoichiometric coefficients (= 1)	[-]	2.7
α	Gas holdup (m3 gas * m-3 reactor)	[-]	2.1
α_b	Gas holdup (at bottom of reactor)	[-]	fig 2.1
α_t	Gas holdup (at top of reactor)	[-]	fig 2.1
Δρ	density difference between metal and gas	[kg/m^3]	2.2
ε_m	mole fraction (of molecule "m") in the inflow	%	2.21/2.22 3.1/3.2/3.3
θ	mole ratio of the molecule		2.28/2.30
ν_l	liquid kinematic viscosity		2.26
ρ_g	density of gas	kg.m^{-3}	2.2/2.29/2.34
ρ_l	density of liquid (molten metal/salt)	kg.m^{-3}	2.2/2.34
σ	stress		2.25/2.32
σ_c	circumferential stress	N.m^{-2}	3.6
a_g	interfacial area (between gas and molten metal)	m^2.m^{-3}	2.5
C	CAPEX	million €	4.1
C_0	distribution parameter		2.11
C_d	Cost of debt	%	4.2
C_e	Cost of equity	%	4.2
C_x	Concentration of molecule "x" (ie. CH_4 or H_2)	mol.m^{-3}	2.6/2.30
D	diameter	metre	fig 2.1
d_b	orifice diameter	[m]	2.31
D_h^*	dimensionless hydraulic equivalent diameter		2.16
dL	differential height	[m^1]	2.1
d_o	initial bubble diameter	[m]	2.31
dP	change in pressure	[N/m^2]	2.2
dV	differential volume	[m^3]	2.1
d_{vs}	Sauter Diameter	[m]	2.23
dX_{CH4}	change in methane conversion	[-]	2.1
E	energy value of the produced hydrogen	million kg (H_2)	4.1
$E^a_{c,f}$	catalytic forward activation energy	J.mol^{-1}	2.8

$E^a_{n,f}$	catalytic forward activation energy	$J.mol^{-1}$	2.10
g	gravitational acceleration	$[m/s^2]$	2.2
H_c	column height	[m]	3.4
i	year indicator		4.1
J_g	superficial gas velocity of the flow		2.11
J_g^+	J_g made dimensionless	[-]	2.11/2.12
K	decomposition reaction equilibrium constant	[-]	2.3
$k^0_{c,f}$	catalytic forward pre-exponential factor	$m.s^{-1}$	2.8
K_c	decomposition equilibrium constant based on concentration	[-]	2.3
$k_{c,f}$	forward rate coefficient of the catalytic reaction	$m.s^{-1}$	2.6
$k_{n,f}$	non-catalytic forward rate coefficient	$m^{3(n-1)}.mol^{(1-n)}.s^{-1}$	2.9
$k^o_{n,f}$	catalytic forward pre-exponential factor	$m.s^{-1}$	2.10
K_p	decomposition equilibrium constant based on partial pressure	[-]	2.3
L	Height (in reactor from bottom up)	metre	fig 2.1
LCOH	levelized cost of hydrogen		4.1
LMP	Larson Miller parameter	3.2.2	3.5
Lt	Height (of reactor - total)	metre	fig 2.1
M_g	molar mass of the gas	$kg.mol^{-1}$	2.29/2.30
n	reaction order	[-]	2.10
n	lifetime of the project	[years]	4.1
N_{Bo}	Bond number	[-]	2.24/2.25
n_{CH4}	methane inlet flow rate	$mole.s^{-1}$	2.1
$n_{CH4,b}$	inlet flow rates of gas molecules (CH_4) at bottom	mol.s-1	2.20
N_{Fr}	Froude number	[-]	2.24/2.27
$N_{Fr,o}$	Froude number of the orifice	[-]	2.24/2.27
N_{ga}	Galilei number	[-]	2.24/2.26
N_{m2}	columns configuration	$-.m^{-2}$	3.4
$N_{we,o}$	Weber number of the orifice	[-]	2.31/2.32
N_μ	viscosity number		2.15
O	OPEX	million €	4.1
P_0	standard pressure (100.000 Pa)	$[N/m^2]$	2.7

P_b	Pressure (in reactor at bottom)	[N/m²]	fig 2.1
p_i	pressure (i = inside / o = outside)	[N/m²]	3.6
P_t	Pressure (in reactor at top)	[N/m²]	fig 2.1
Q_{H2}	total amount of hydrogen produced	Nm3 / day	4.3
Q_M	total amount of CH4 / N2 in inflow	Nm^3 / day	4.3
R	Reaction rate	$mole.m^{-3}.s^{-1}$	2.1
R	the "Gas constant" (= 8.314)	$J\ mol^{-1}\ K^{-1}$	2.3
r	discount rate	%	4.1
R_c	Reaction rate (catalytic)	$mole.m^{-3}.s^{-1}$	2.1/2.5
r_c	net catalytic reaction rate	$mol.m^{-2}.s^{-1}$	2.5
r_i	radius (i = inside / o = outside)	[m]	3.6
R_n	Reaction rate (non-catalytic)	$mole.m^{-3}.s^{-1}$	2.1
r_n	net non-catalytic reaction rate	$mol.m^{-2}.s^{-1}$	2.9
$R_{n,x}$	Reaction rate (non-catalytic) x = f (forward) & b (backward term	$mole.m^{-3}.s^{-1}$	2.9
T	Temperature (sub b at bottom sub t at top)	K	2.3
tr	operational lifetime at temperature T		3.5
t_w	wall thickness	[m]	3.6
U_b	velocity of the initial bubbles	m.s-1	2.33
V_d	value of the firm's debt		4.2
V_e	market value of the firm's equity		4.2
$V_{g,b}$	gas volume flow at the bottom of the reactor		2.20
V_{gj}	void-fraction weighted mean drift velocity	$m.s^{-1}$	2.11
V_{gj}^+	V_{gj} made dimensionless	[-]	2.11/2.13/2.17/2.18/2.19
W	Weight	[mt]	3.4
WACC	weighted average cost of capital		4.2
W_d	weight dependent on column height	$mt.m^{-1}$	3.4
W_i	weight independent on column	$mt.m^{-2}$	3.4
W_{max}	Max load spreading over platform surface	$mt.m^{-2}$	3.4
X_{CH4}	methane conversion	[-]	2.4/ 3.1/3.2/3.3
y_m	mole fraction in the outflow (of molecule "m")	%	3.1/3.2/3.3

List of figures

List of tables

1. Introduction

The excellent properties of hydrogen molecules exploit opportunities for transportation, storage and clean production of energy. Therefore, especially in hard-to-abate sectors like heavy industry and transport, the expectations of hydrogen are high and it is even labelled "fuel of the future". Most hydrogen today still comes from methane reforming in which methane is converted into hydrogen and CO_2, resulting in a lot of greenhouse gas emissions during production. However to utilize hydrogen for decarbonization the production of CO_2 in the process has to be mitigated. Two options could be taken to decarbonize the production of hydrogen: (i) mitigate the CO_2 emissions entering the atmosphere by carbon capture and storage (CCS) and (ii) apply a more sustain technology for the production of hydrogen.

Hydrogen from reforming with CCS is called blue hydrogen and has much value in the current production build-up, however reducing all emissions to zero is very difficult with CCS. On the other side electrolysis is a sustainable technology that produces hydrogen (and oxygen) by splitting water with electricity. When the electricity is produced by renewable energy sources such as wind turbines and solar panels, electrolysis is carbon-free and it produces green hydrogen. Nevertheless, the renewable electricity supply is not yet up to scale therefore additional technologies are necessary to pave the way for a mature, affordable infrastructure and market for hydrogen (H-Vision, 2019).

A relatively immature technology for producing hydrogen from fossil fuels called methane pyrolysis shows great potential to mitigate the CO_2 output of sustainable hydrogen production on a large scale. Hydrogen production by methane pyrolysis produces solid carbon instead of gaseous, therefore emissions are prevented, and the process energy demand is up to 7 times lower than electrolysis. Hydrogen from methane pyrolysis is called turquoise hydrogen, indicating that is in-between blue and green hydrogen from a sustainable point of view.

Not only the production but also transportation of sustainable hydrogen benefits the emerging hydrogen economy as transport would enhance the market competitiveness of hydrogen. Transportation in the current offshore natural gas pipeline infrastructure could be one of the methods to make the market more competitive. This research will try to contribute to both potentials by investigating the feasibility of offshore methane pyrolysis.

1.1 Research partner and location

This research will be executed in cooperation with ONE-Dyas. ONE-Dyas is an oil and gas exploration and production company and the largest privately owned in the Netherlands. Their strategical position in North Sea gas both in the Netherlands and the UK makes them an interesting partner to investigate offshore methane pyrolysis.

The research is based on ONE-Dyas their latest project in the GEMS-area. The N05-A project will operate the eponymous field and neighbouring prospects and will be connected to the NGT-pipeline which transports natural gas from the Dutch North Sea to Uithuizen on the Dutch shore. Furthermore, the platform operations will be near zero-emission due to electrification by integration with an electricity supply from the German Riffgat windfarm. A

possible onshore comparison will be necessary during the research, when this occur the Q16-Maas project location in the Maasvlakte will be utilized as a reference. Both cases are shown in Figure 1.

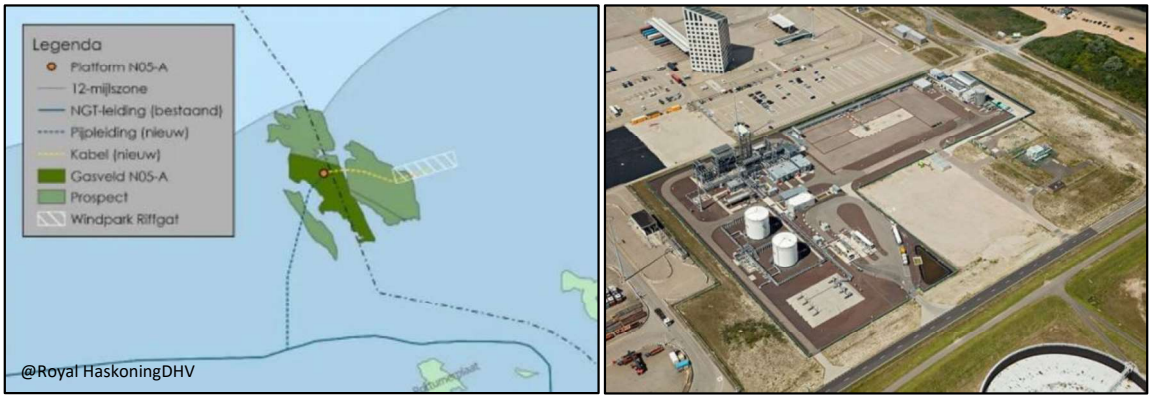

(a) N05-A gas field (b) ONE-Dyas Maasvlakte

Figure 1.1: *(a) The proposed platform (orange) on the N05-A gas field (dark green). The bottom blue line indicates the connection to the NGT-pipeline (bottom blue line). (b) The onshore location where ONE-Dyas processes natural gas from Q16 Maas.*

1.2. Problem statement and research goal

Nearly a third of the current global CO_2-emissions can be accounted to heavy-duty transport (trucking, shipping, aviation) and the heavy industry (cement, steel, chemicals, aluminium) and with various other sectors decarbonizing this share could double to two-thirds by 2050 (Energy Transition Commission, 2018). Finding low-carbon energy sources for these hard-to-abate sectors will, therefore, be vital to meet the Paris climate agreement and keep global warming by 2050 to a 2°C or the even tougher 1.5°C limit. A comprehensive approach to decarbonization will demand electrification of equipment, but also clean molecular energy when electrification is not applicable (Molloy & Baronett, 2019). Hence, the EC has adopted a hydrogen strategy for fostering a market for clean molecular energy. Hydrogen is very suitable, since it can be applied as fuel for instance for (very-)high temperature heating installations, but also as feedstock without emitting greenhouse gasses into the atmosphere (European Commission, 2020). In addition, hydrogen has an essential function as energy carrier. Since suitable places for large-scale renewable energy generation are commonly located far away from the demand clusters, e.g. solar power in the Sahara, transmission with electricity would induce major losses. The losses associated with long-distance hydrogen transport however are mostly related to preparation for shipping, like compression or liquifying of the hydrogen or bonding it to other molecules, making it outstanding for distance transport of energy in comparison to electricity.

Even though hydrogen will be essential to obtain climate neutrality, currently only a modest fraction of the EU energy mix is represented by hydrogen. For hydrogen to decarbonize the hard-to-abate sectors, a far larger scale and a fully decarbonized production process needs to be in place. However, starting a hydrogen economy in Europe tends to be difficult considering that green hydrogen is not yet cost-competitive with current energy sources. To become cost competitive large-scale implementation and production of hydrogen is needed, but the situation can be best described as a chicken-and-egg problem (Hydrogen Council, 2020). Production of sustainable hydrogen needs large-scale customers, but the industry is reluctant

due to the immense investments required to adjust their installation for hydrogen implementation when the supply is not up to scale (Burgess, 2021).

Methane pyrolysis, with the potential to produce emission-free hydrogen with a relative limited process energy demand, can serve as intermitted step until a hydrogen economy based on green hydrogen from electrolysis is established. Even though it utilizes natural gas, the technology has no gaseous CO_2 waste stream as methane decomposes into hydrogen and solid carbon. Depending on the quality of the solid carbon, it can be sold as feedstock for tires and paint or to increase the richness of soils however when sales options are unavailable it can be easily sequestrated.

Next, to production for the growth of a sustainable hydrogen economy also international trade would be a beneficial influence. By repurposing the current North Sea pipeline infrastructure, hydrogen transport through these pipelines would be enabled which fosters market competition, security of supply and security of demand. Specifically with N05-A in mind, also the operating company of the NGT pipeline has investigated the possibilities to accelerate the development of windfarms further offshore by accommodating a hydrogen volume equivalent to multiple GW offshore wind (Noordgastransport, 2022). By repurposing their pipeline to hydrogen from offshore wind, the infrastructure could be operational around 2030 and the pipeline has already received the necessary Certificate of Fitness to transport hydrogen (Aberdeen Business News, 2022).

Even though the current gas fields in the North Sea are depleting, North Sea natural gas production will be relevant in the next decades, especially with the intentions of the Dutch government to become more independent of Russia's supply. Hence the stream in the NGT-pipeline would be a blend with a high percentage of hydrocarbons due to mixing of the offshore wind hydrogen and platform gas stream. To accelerate the availability of the North Sea pipeline infrastructure for a high-concentration hydrogen flow, future natural gas production needs to be converted into hydrogen offshore. Consequently, the current offshore pipelines would become available for hydrogen transport, moreover the additional flow of hydrogen would be very beneficial for kick-starting a sustainable hydrogen economy.

Taking into account the different potentials this research is interested in and the specific location it will focus on, the research goal can be defined. The goal is to research the technical feasibility of offshore methane pyrolysis by designing a facility for the N05-A platform and quantifying the performance, also in terms of cost. The conventional reforming technologies will be utilized as reference, with and without CCS, to compare the potential of methane pyrolysis as intermitted production technology of hydrogen. The research goal is modified to a research question and relevant sub-questions in Section 1.4 Research question.

1.3. Research background

Before methane pyrolysis can be investigated for the production of offshore hydrogen production, background knowledge of the technology was necessary. Prior to the thesis, a literature research was executed to understand how methane pyrolysis works, to identify the

current technologies and maturity and to determine the most suitable technology for the offshore design. A summary is given in this section.

Methane pyrolysis demands a continuous heat input and is based on the thermal decomposition of methane. Due to the strong C-H bonds and the symmetry of its molecular structure, non-catalytic methane pyrolysis occurs only above 1100-1200 °C (Ashik et al., 2015). In the reaction, a molecule of methane (CH_4) converts into a solid carbon molecule (C) and two hydrogen molecules (H_2). Due to the different phases, the two products are easy to separate from each other. One of the main advantages over conventional reforming technologies is the lack of CO_2 production in the process. As the only reactant is methane, there is no oxygen present and bonding with split carbon molecules is avoided. After processing, the solid carbon can be sold as feed e.g. paint, tires or as fertilizer. The hydrogen needs to be separated from the unconverted natural gas and afterwards can be further processed depending on the purpose.

The process can be modified by a couple of important parameters. Since methane pyrolysis is an endothermic reaction, an increasing temperature would foster the reaction and improve the conversion rate of methane. An increase in pressure has the opposite effect on the reaction but improves the workability of the plant (Antzara et al., 2014). Fortunately, the temperature can be lowered when utilizing a catalyst. A good conversion ratio could already be reached at 1000 °C or even lower depending on the catalyst. On the other hand, the use of a catalyst increases the complexity of the reactor. The size and inflow of the reactor are also relevant for the conversion of methane. The longer a reactor, the more time the molecules have to convert enhancing the conversion ratio. Furthermore, a smaller flow or reactor diameter would also enhance the conversion rate as the number of molecules that could be converted is relatively reduced.

Due to the multiple catalyst and design possibilities, there are also multiple options for the application of methane pyrolysis. The options have a varying maturity as the range extends from laboratory scale to commercially successful facilities however the literature research focussed on the options that were working towards a pilot plant or larger to increase the reliability of the data. The five options satisfying this are listed with their operating companies to strengthen the understanding of the broad range. Monolith has a full commercial scale applying the plasma torch technology. The plasma torch results in the non-catalytic conversion of methane at around 2000 °C to produce hydrogen, this installation however focuses on the production of solid carbon (Schneider et al., 2020). BASF utilizes a solid catalyst that moves in the opposite direction of the gas flow. The gas reacts on the surface of the catalyst that has a temperature of 1400 °C (BASF, 2021). The performance of the current pilot plant is tested for different conditions, e.g. pressure and inflow. Hazer Group's fluidized bed installation produces hydrogen but also a more valuable carbon by-product. With an additional inflow of iron ores, Hazer group converts carbon and iron ores into valuable graphite. In comparison to other technologies, it has a smaller production of hydrogen due to the low conversion per pass partly explainable by the low 850 °C operating temperature (Daliah, 2021). C-Zero's reactor is filled with molten salt. Due to the molten state, the catalyst has a high heat capacity and viscosity, resulting in improved heat transfer and thermal inertia

of the catalyst. The company has planned a pilot plant for 2022 being the first pilot with a molten fill (Jones, 2021). At last, TNO also uses the benefits of molten catalysts by filling their tank with molten metal. This is even more catalytic than salt but can contaminate the produced carbon. To mitigate this the top of the reactor will be filled with molten salt which separates the metal from the solid carbon utilizing the beneficial properties of metal without contaminating the carbon (Bhardwaj et al., 2021). Their pilot plant is scheduled for 2023.

As only one technology can be applied, a multi-criteria analysis was executed to find the most suitable technology. The following criteria were important for offshore large-scale methane pyrolysis and therefore included: (i) reactor dimensions, (ii) reactor weight, (iii) reactor pressure, (iv) flexibility and operability, (v) reliability availability and redundancy, (vi) carbon outflow, (vii) conversion ratio, (viii) cost, (ix) energy demand, (x) emissions and (xi) technical readiness level. The analysis weighs each criterion on its significance and scores them per technology. The most suitable technology is the one with the highest overall score after summing the weighted criterion scores. The combined molten metal and salt technology from TNO emerged with the highest score. This is primarily due to the high catalytic behaviour of the molten metal as it reduces size, demands less energy and can operate at high pressure. The molten metal and salt technology is, therefore, taken as the starting point in this thesis for the design of a methane pyrolysis reactor and to determine the solution space that represents cost-competitive methane pyrolysis.

1.4. Research question

To execute a techno-economic analysis necessary to determine the technical and economic feasibility of offshore methane pyrolysis. A research question has been constructed which serves as a guideline for the entire project:

"Define the solution space that represents cost-competitive offshore methane pyrolysis in the Netherlands and what challenges methane pyrolysis should overcome?"

For a structural approach to answering the research question, additional sub-questions have been raised. They should make sure the important aspects of the research question are covered and the answer is founded with concrete arguments:

1. *How do the relevant properties of a molten metal and salt reactor influence the performance of methane pyrolysis?*
2. *What technical design characteristics would result from the integration of methane pyrolysis on an offshore platform at the N05-A field?*
3. *What would be the Levelized Cost of Hydrogen (LCOH) for offshore methane pyrolysis? And how would the LCOH of conventional technologies change when determined for the same conditions?*

1.5. Methodology and research outline

The sub-questions, all discussed in a separated chapter, are constructed such that they create a logical sequence throughout the report. Therefore, previous chapters provide important insights for the following chapters. All information comes together in the conclusion, where the sub-questions enable a solid answer to the research question.

First, a model will be developed in chapter 2, which describes the behaviour and performance of a molten metal and salt reactor. In chapter 3, the offshore limitations of the N05-A platform are translated into a model for offshore design. Integration of both the model for methane pyrolysis and the model for offshore design defines the technical design characterises and can determine the technical feasibility of offshore methane pyrolysis. The economic analysis in chapter 4 establishes the Levelized Cost of Hydrogen. By subjecting the analysis to multiple scenarios a range is created. The uncertainties, market fluctuations, etc. offer the opportunity to quantify the influence of the different cost flows in the project. The low, base and high scenarios are compared to the conventional reforming methods for producing hydrogen, steam methane reforming (SMR) and autothermal reforming (ATR) under the same conditions which provides the answer to the research question. In chapter 5, the writer reflects back on the report in the conclusion and last in Chapter 6 recommendations for future research are listed.

2. Modelling of methane pyrolysis

The decomposition of methane during pyrolysis in a catalytic molten bath depends on the interplay between the hydrodynamics and the reaction kinetics of the rising gas. As most activities occur on the catalytic interface between the gas and molten catalyst, predicting the reactive surface on the interface will be an important part of modelling methane pyrolysis. Next, inside the bubbles, non-catalytic decomposition occurs depending on the temperature. Both, the non-catalytic and catalytic decomposition depend on the gas holdup. However, modelling this gas holdup has shown to be difficult in previous research and, therefore, has been fixed at the bottom of the tank (Parkinson et al., 2017; Upham et al., 2017).

One approach has been found to include a changing gas holdup into a model. In two papers by Catalan and Rezaei (2020, 2022), a regression analysis of experiments with molten metal has been utilized to relate the flow velocity to gas holdup. Since this research would like to avoid large assumptions regarding the gas holdup, the varying approach by Catalan and Rezaei is replicated. The resulting model has been validated for similar conditions to prove the replicability of the model. The writer's perspective on the behaviour of the gas flow near the bottom of the reactor differs from Catalan and Rezaei's. The model is therefore modified according to this perspective on reactor behaviour at the bottom better. At last, the replicated model is calibrated for a metal reactor but as indicated in the 1.3 Research Background, molten metal and salt would be the best combination for filling the molten bath. Therefore, effort has been put into extending the model to include both metal and salt.

The model approaches the reactor as multiple thin horizontal slices filled with metal and gas and is based on material balance. By integrating the slices, the methane conversion, pressure, flow velocity and many more parameters can be determined over the height of the reactor. The liquid in the reactor is assumed to have a constant temperature over the height due to mixing and recirculation caused by the gas flow through the tank.

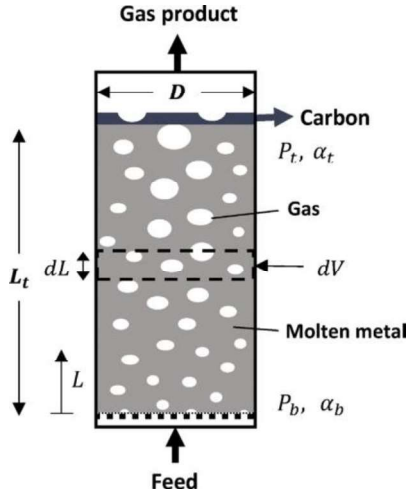

Figure 2.1 *Simplified representation of reactor with a single liquid molten medium (Catalan & Rezaei, 2020)*

2.1 Modelling of hydrodynamics and kinetics

This section starts with the explanation of the model design and ends with proof that shows the replicated model produces similar results for the same parameters as Catalan and Razaei obtained (2022). The model is based on the coupling of the hydrodynamics and the kinetics of the gas flow and is based on two differential equations that represent the material balance (Equation 2.1) and the pressure change over the height of the reactor (Equation 2.2).

The differential material balance equation looks as follows:

$$\dot{n}_{CH_4}\, dX_{CH_4} = (R_c + R_n)\alpha dV = (R_c + R_n)\alpha \frac{\pi D^2}{4} dL \tag{2.1}$$

Where $\dot{n}_{CH_4}$ is the methane inlet flow rate at the bottom of the reactor (mole.s^{-1}) and dX_{CH_4} the change in methane conversion (-). On the right side, the R_n and R_c represent the non-catalytic and catalytic reaction rates (mole.m^{-3}.s^{-1}) of the gas volume, which is described by the gas holdup α (m^3 gas. m^{-3} reactor) and the differential volume dV (m^3).

The change in pressure depends on the hydrostatic pressure from the molten metal. As gravity pushes the volume down, the bottom of the tank will endure the largest weight and has the highest pressure.

The differential pressure change is described by:

$$d\mathrm{P} = -\left[\rho_\mathrm{l}(1-\alpha) + \rho_g\alpha\right] g d\mathrm{L} = -(\rho_1 - \alpha\Delta\rho) g dL \tag{2.2}$$

where dP is the change in pressure (N/m^2), ρ_l is the molten metal density (kg/m3), ρ_g is the gas density, $\Delta\rho$ the difference between the metal and gas and last gravity comes into play as g represents the gravitational acceleration (m.s^{-2}).

The system boundaries are the bottom and the top of the reactor. At L=0 the X_{CH_4} =0 and P=P_b at the bottom and L=L_t at the top. By solving both differential equations for the stated situation, the methane conversion and pressure at the outlet of the reactor are found. To do so, the unknown parameters must be related to the known parameters.

2.1.1 Kinetics of non-catalytic and catalytic methane decomposition

Together the non-catalytic and catalytic reaction rates determine how much methane is converted into hydrogen and carbon given a certain gas flow volume. However, only in very rare situations, all methane is converted into hydrogen. This section starts with defining the conversion limitation, which is mainly due to temperature and pressure. Afterwards, the specific reaction rate, both for non-catalytic and catalytic decomposition, in various liquids is discussed. With both effects on the conversion rate included in the model, it will mimic the influence of the molten metal on the pace of conversion but will be thermodynamically consistent as the reaction rate will be zero when the limitation is reached.

Limitations

The limitations on the decomposition of methane are defined by the reaction equilibrium constant based on partial pressure K_P or concentration based K_c. This constant defines the equilibrium between the product and reactants of a reaction, in other words, the maximum conversion ratio. The equilibrium between methane on the reactants side, and hydrogen and solid carbon on the product side, depends on temperatures and pressures. As the methane pyrolysis reaction is endothermic, the equilibrium shifts towards the products (hydrogen and carbon) when increasing the temperature and shifts towards the reactant (methane) upon increasing pressure. This behaviour is called the Le Chatelier's principle (Liu et al., 1996). In the temperature range from 900 to 1200 ˚C, the K can be very accurately described as followed:

$$\ln K = 13.2714 - \frac{91204.6}{RT} \tag{2.3}$$

where R is the gas constant (8.314 J mol^{-1} K^{-1}) and T is the temperature in Kelvin. The empirical slope and intersect for the inverse of the temperature are found by data regression in the temperature range and lead to less than 0.41% relative difference in comparison to the actual K values (Catalan & Rezaei, 2020; Smith, 1950).

To show the relationship between methane conversion, pressure and temperature, the equilibrium constantly needs to be related to these parameters. K is defined by the difference in partial pressures between the products and reactant of the methane pyrolysis reaction. Where partial pressure depends on the molecule concentration, the gas constant and temperature. For methane pyrolysis, K_p is shown in Eq. 4. The entire derivation behind it can be found in Appendix A1.

$$K_p = \frac{P \cdot \left(4{X_{CH_4}}^2\right)/\left({X_{CH_4}}^2 + 2X_{CH_4} + 1\right)}{\left(1 - X_{CH_4}\right)/\left(1 + X_{CH_4}\right)} \tag{2.4}$$

By solving Equation 2.4 for the methane conversion, X_{CH_4}, with the equilibrium constant according to Equation 2.3, the maximum conversion can be plotted against the temperature for different pressures. This is done in Fig. 3, again showing that methane pyrolysis is an endothermic process since with increasing temperature and decreasing pressure the conversion ratio increases.

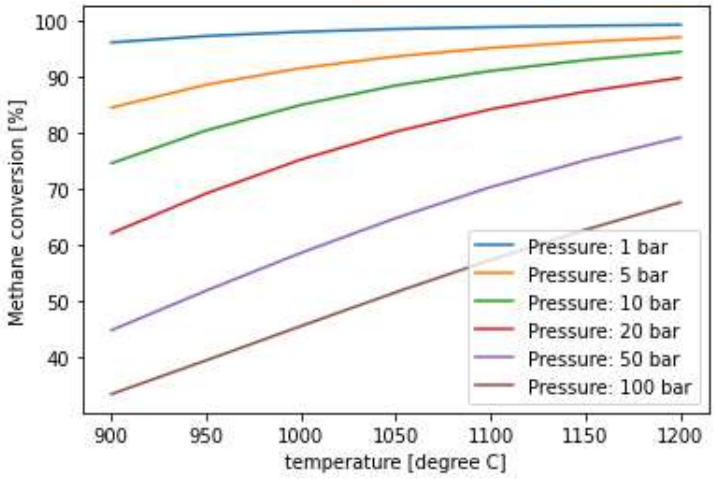

Figure 2.2: Methane pyrolysis equilibrium conversion considering varying temperature and pressure

The catalytic reaction rate

As catalytic methane pyrolysis happens on the interface of the gas bubbles, not only the gas volume in the reactor is important, but also the reactive surface area of this interface between gas and the molten metal. The larger this interfacial area, a_g ($m^2.m^{-3}$), relative to the total gas volume, the more methane is converted into hydrogen. The catalytic reaction rate, R_c (mol $CH_4.m^{-3}.s^{-1}$), therefore, consist of the a_g, describing the interfacial area, and the net catalytic reaction rate, r_c ($mol.m^{-2}.s^{-1}$), describing the influence of the molten metal on the conversion ratio:

$$R_c = a_g r_c \tag{2.5}$$

The interfacial area in molten metal is determined by the rising bubble size, hence gas flow with a similar volume but smaller bubbles results in a larger reactive surface. Since the bubble size is related to superficial velocity via an experimental correlation in the model of Catalan & Razaei, this topic will be discussed in 2.1.3 Superficial velocity of gas flow in the reactor.

The net catalytic reaction rate will be elaborated in this paragraph. It consists of a term that indicates the forward reactions, but as hydrogen and solid carbon also partly convert back into methane, also a term for a backward reaction is included. This backward reaction is important as it makes sure that when reaching the thermodynamic equilibrium, the net reaction rate tends towards zero, as discussed in the previous paragraph. Experiments with two alloys, Nickel-Bismuth ($Ni_{0.27}Bi_{0.73}$) and Copper-Bismuth ($Cu_{0.45}Bi_{0.55}$), as molten metal have shown that the relationship between the forward catalytic rate and the concentration of methane is of the first-order (Catalan & Rezaei, 2022). The net catalytic reaction rate can therefore be described by:

$$r_c = r_{c,f} - r_{c,b} = k_{c,f} C_{CH_4} - \frac{k_{c,f}}{K_C} {C_{H_2}}^2 = k_{c,f} C_{CH_4} \left(1 - \frac{{C_{H_2}}^2}{C_{CH_4} \cdot K_C}\right) \tag{2.6}$$

Where $k_{c,f}$ is the forward rate coefficient of the catalytic reaction ($m.s^{-1}$) and depends on the type of material. Molten $Ni_{0.27}Bi_{0.73}$ and $Cu_{0.45}Bi_{0.55}$ are taken into account to be in line with the

experimental results the parameters are based on. C_{CH_4} and C_{H_2} represent the concentration of the representative molecules (mol.m^{-3}) and K_C is the equilibrium constant, but based on the concentration and not the partial pressure. Kc is therefore determined by a modified version of Equation 2.4:

$$K_C = K\left(\frac{P_0}{RT}\right)^{\sum_{i(g)} \nu_i} \tag{2.7}$$

$\sum_{i(g)} \nu_i$ describes the sum of the stoichiometric coefficients in the methane pyrolysis reaction. However, as the carbon occurs in solid form, it is taken out so $\sum_{i(g)} \nu_i = 2 - 1 = 1$. P_0 is the standard pressure (100.000 Pa).

The catalytic forward rate coefficient follows the Arrhenius equation, which is an expression for the dependence on temperature of reaction rates:

$$k_{c,f} = k_{c,f}^0 \exp\left(-\frac{E_{c,f}^a}{RT}\right) \tag{2.8}$$

The catalytic forward pre-exponential factor $k_{c,f}^0$ and the catalytic forward activation energy $E_{c,f}^a$ are experimentally determined for molten $Ni_{0.27}Bi_{0.73}$ and $Cu_{0.45}Bi_{0.55}$. These experimental values are found by Palmer et al. (2019) and Upham et al. (2017) and can be found in Table 2.1.

A possible limitation for the catalytic forward rate coefficient would be the mass transfer rate within the bubbles. With the nonporous liquid metal surrounding the bubble, mass transfer limitation only occurs on the gas side of the bubble surface. When diffusion inside the bubble, depending on the diffusion coefficient of the molecules but also internal flow in the bubbles, is too low, the reaction on the surface of the bubble is limited by the mass transfer of the molecules. Such mass transfer limited reactions respond differently to temperature and flow conditions and demand an additional correction factor to account for the reduction in efficiency. Parkinson et al. (2021) tested this behaviour for methane decomposition in a molten salt combination of Sodium-Bromide (NaBr) and Potassium -Bromide (KBr). In the range of interfacial area ag between 600 and 1200 m^2.m^{-3}, the results indicate that catalytic methane decomposition is very likely, not mass transfer limited but just reaction limited. Since the activation energy of the NaBr:KBr combination is only slightly higher than the $Ni_{0.27}Bi_{0.73}$ and $Cu_{0.45}Bi_{0.55}$, therefore, it is assumed that the same condition can be applied. Taking into account this assumption and the fact that mass transfer would only improve when smaller diameters are applied, the catalytic methane decomposition will be reaction limited in this research when bubbles do not exceed 9.6 mm in diameter, corresponding to a_g = 600 m^2.m^{-3}. A correction factor for reduced efficiency is, therefore, not necessary and Equation 2.8 is utilized in its current form.

Table 2.1: *Kinetic parameters for catalytic methane decomposition in $Ni_{0.27}Bi_{0.73}$ (Upham et al., 2017) and $Cu_{0.45}Bi_{0.55}$ (Palmer et al., 2019)*

Parameter	Units	Value Ni0.27Bi0.73	Value Cu0.45Bi0.55
$k^0{}_{c,f}$	m.s-1	7.88×10^4	4.32×10^5 [a]
$E^a{}_{c,f}$	J.mol-1	208,000	222,000

[a] Palmer et al. (2019) calculated the pre-exponential factor in a different unit by assuming $d_b = 0.007$ m. The $k^0 = 3.7 \times 10^8\ s^{-1}$ is converted by $k^0{}_{c,f} = k^0/a_g$ with $a_g = 6/d_b$. Since they kept the conversion below 10% the backward reaction was minimized in the experiments

The non-catalytic reaction rate

Non-catalytic decomposition of methane, R_n, happens inside the gas bubbles and is, therefore, always reaction limited as no transfer from the bubble interface is necessary. The set-up of the net non-catalytic reaction rate R_n is similar to the net catalytic reaction rate r_c, with both a forward $R_{n,f}$ and backward term $R_{n,b}$ to represent the conversion but also the equilibrium limitation. However, the empirical relationship with the forward non-catalytic term is not linear but the order n this time:

$$R_n = R_{n,f} - R_{n,b} = k_{n,f} {C_{CH_4}}^n - \frac{k_{n,f}}{K_C} {C_{H_2}}^2 {C_{CH_4}}^{n-1} = k_{n,f} {C_{CH_4}}^n \left(1 - \frac{{C_{H_2}}^2}{C_{CH_4} \cdot K_C}\right) \quad (2.9)$$

Where most parameters have already been discussed in the previous paragraph except for the non-catalytic forward rate coefficient $k_{n,f}$ ($m^{3(n-1)}.mol^{(1-n)}.s^{-1}$). The forward rate coefficient again follows the Arrhenius equation, as in Equation 2.7:

$$k_{n,f} = k^0_{n,f} \exp\left(-\frac{E^a_{n,f}}{RT}\right) \quad (2.10)$$

The non-catalytic forward pre-exponential factor $k^o{}_{cf}$ and the non-catalytic forward activation energy $E^a{}_{cf}$ and also the reaction order n are based on experimental data (Keipi et al., 2017). A regression analysis has been executed to minimize the sum of squares regarding the difference between the experimental and the predicted methane conversion by Catalan & Razaei (Catalan & Rezaei, 2020) resulting in the parameter values shown in Table 2.

Table 2.2: *Kinetic parameters for non-catalytic methane pyrolysis (Catalan & Rezaei, 2020).*

Parameter	Units	Value
$k^0{}_{n,f}$	$m^{3(n-1)}.mol^{(1-n)}.s^{-1}$	1.4676×10^{10}
$E^a{}_{n,f}$	$J.mol^{-1}$	284,948
n	-	1.0809

Note. Determined by Catalan and Razaei (2020) based on experimental data from (Keipi et al., 2017)

2.1.2 Gas holdup in molten metals

Since the heat and mass transfer processes are heavily dependent on the gas holdup, it makes sense to see that gas holdup is part of the differential material balance equation. Research on two-phase flows with for instance water and air is relatively common, however considering

this research focuses on molten metal, relevant research regarding gas holdup is limited. In this section, the gas holdup correlation from Kataoka and Ishii (1987) will be discussed as this is the only available research that determined the gas holdup correlation in molten metal, according to Catalan and Rezaei.

The research found a strong relation between gas holdup, α, and the superficial gas velocity of the flow J_g. When assuming that the superficial gas velocity is much higher than the superficial velocity of the metal the equation becomes:

$$\alpha = \frac{j_g}{C_0 j_g + V_{gj}} = \frac{{j_g}^+}{C_0 {j_g}^+ + {V_{gj}}^+} \tag{2.11}$$

The distribution parameter C_0 is determined by the reactor geometry and V_{gj} represents the void-fraction weighted mean drift velocity (m.s^{-1}). Also, dimensionless parameters, ${j_g}^+$ and ${V_{gj}}^+$, can be utilized to calculate the gas holdup. The superficial gas velocity and drift velocity are modified for the molten metal properties, i.e., surface tension σ and molten metal density ϱ_l, and look as follows:

$${j_g}^+ = \frac{j_g}{(\sigma g \Delta\rho / {\rho_l}^2)^{1/4}} \tag{2.12}$$

$${V_{gj}}^+ = \frac{V_{gj}}{(\sigma g \Delta\rho / {\rho_l}^2)^{1/4}} \tag{2.13}$$

This research utilizes a cylindrical reactor, as pressure is equally divided over the surface of the wall when utilizing a round shape. The distribution parameter is therefore defined by the following equation:

$$C_0 = 1.2 - 0.2\sqrt{\rho_g / \rho_l} \tag{2.14}$$

Various correlations for the dimensionless drift velocity have been found (Kataoka & Ishii, 1987). The different regimes for these correlations are defined by ${j_g}^+$, the viscosity number and the dimensionless hydraulic equivalent diameter D^*_h:

$$N_\mu = \frac{\mu_l}{\left(\rho_l \sigma \sqrt{\sigma/(g\Delta\rho)}\right)^{0.5}} \tag{2.15}$$

$${D_h}^* = \frac{D}{\sqrt{\sigma/(g\Delta\rho)}} \tag{2.16}$$

In the first regime, molten metal baths with substantial liquid recirculation are considered, i.e., ${j_g}^+ >> 0.5$. V_{gj}^+ is described by three correlations. When the ${D_h}^*$ surpasses the threshold ${D_h}^* = 30$, the gas flow is no longer affected by the walls of the reactor, except close to the wall:

$$V_{gj}^{+} = 0.030\left(\rho_g/\rho_f\right)^{-0.157} N_{\mu,f}^{-0.562} \qquad for\ N_{\mu,f} \leq 2.2\text{x}10^3 \qquad (2.17a)$$

$$V_{gj}^{+} = 0.92\left(\rho_g/\rho_f\right)^{-0.157} \qquad for\ N_{\mu,f} \geq 2.2\text{x}10^3 \qquad (2.17b)$$

Moreover, when Dh is below the threshold, Vgj+ does depend on Dh*:

$$V_{gj}^{+} = 0.0019 D_H^{*0.809}\left(\rho_g/\rho_f\right)^{-0.157} N_{\mu,f}^{-0.562} \qquad for\ N_{\mu,f} \leq 2.2\text{x}10^3 \qquad (2.17c)$$

The second regime considers a situation with small liquid recirculation which is defined as $j_g{}^{+} < 0.5$. In this case, two equations have been constructed describing a churn-turbulent and bubbly flow. The equations constructed, by Ishii in preceding research (1977), accurately predict $V_{gj}{}^{+}$ according to the experiments and are defined by:

$$V_{gj}^{+} = \sqrt{2}(1-\alpha)^{1.75} \qquad for\ bubbly\ flow \qquad (2.18a)$$

$$V_{gj}^{+} = \sqrt{2} \qquad for\ turbulent\ flow \qquad (2.18b)$$

Due to the opaque properties of molten metal, visualization of gas bubbles and gas holdup in molten metals is hard to achieve as optical and photographic methods are impossible. Conventional measurements of the gas holdup compared the molten metal surface height during testing with the original surface height, however, Hibiki et al. (2000) were able to visualize the gas holdup with neutron radiography, which can visualize the gas flow through a solid reactor wall. The results can be found in Fig. 2.4. The liquid convection in the tank is induced by the momentum exchange between the rising gas bubbles and the reactor fill, i.e., molten metal. Smaller bubbles move upwards and will coalesce with each other temporarily forming resulting in larger bubbles, before breaking up and dispersing towards the wall. The induced convection significantly affects the gas holdup profile in the pool.

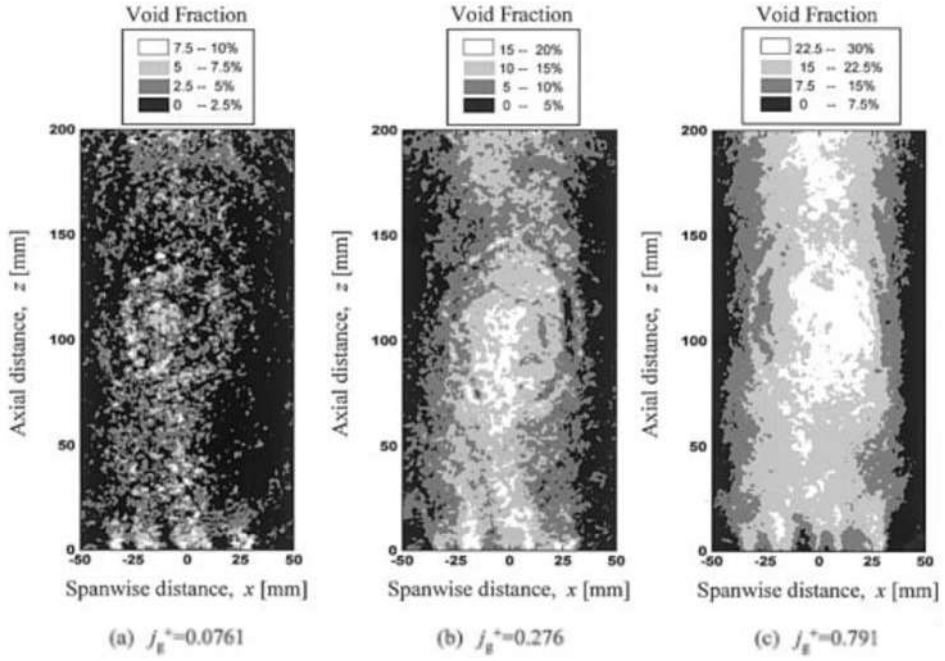

Figure 2.3: *Gas holdup of nitrogen in molten PbBi (Hibiki et al., 2000)*

Additionally, the regimes that describe V_{gj}^{+} are combined to create one equation, applicable for reactors with and without substantial liquid recirculation (substantial when $j_g^{+} > 0.5$). The equation was, therefore, able to describe the entire j_g^{+} range:

$$V_{gj}^{+} = V_{gj_{Eq.2.17}}^{+} exp(A\, j_g^{+}) + V_{gj_{Eq.2.18}}^{+} (1 - exp(A\, j_g^{+}) \quad (2.19)$$

The parameter A has been set to -1.39 to guarantee that $exp\left(Aj_g^{+}\right) = 0.5$ when $j_g^{+} = 0.5$.

In the research by Hibiki et al. (2000), Equation 2.11 has also been compared to experimental results to determine the accuracy. They utilized their experimental data in a system with a molten Tin-Bismuth mixture and nitrogen as gas, but also data from Saito et al. (1998), where molten Gallium was utilized with nitrogen. Considering both data sets, the relative error of the equation was determined to be approximately 30% within the range of dimensionless superficial gas velocities from 0.001 to 2 and gas holdup from 0 to 32%. Experimental data to validate behaviour outside this region is not available, therefore, the model is limited to both ranges as the relative error beyond them is unknown.

2.1.3 Superficial velocity of gas flow in reactor

In the papers by Lionel Catalan and Razaei, the superficial gas velocity correlation depends on the volumetric gas flow and volume of the reactor. It defines how fast the gas passes through the molten layer at a specific height. Due to the increasing conversion of methane molecules over the height, the volume flow will increase over the height and therefore, also the conversion ratio is reflected in the volumetric gas flow and superficial gas velocity.

Gas flow volume and velocity

The volume flow at the bottom of the reactor depends on the molar inflow, which can consist of multiple molecules. Foremost, this is methane, but the inflow can be supplemented with impurities from the natural gas, e.g. nitrogen, or hydrogen when the system has multiple cycles or in series connected reactors. The equation follows the ideal gas flow, taking into account the inflow pressure and temperature:

$$\dot{V}_{g,b} = \frac{\left(\dot{n}_{CH_4,b} + \dot{n}_{H_2,b} + \dot{n}_{I,b}\right)RT_b}{P_b} \quad (2.20)$$

where $\dot{n}_{CH_4,b}$, $\dot{n}_{H_2,b}$ and $\dot{n}_{I,b}$ are the inlet flow rates (mol.s^{-1}) of the respective molecules (methane, hydrogen or an inert molecule such as nitrogen). R is the gas constant, T_b is the bottom temperature (K) and P_b is bottom pressure (Pa).

With an increasing height also the number of methane molecules decreases because of the conversion into hydrogen. To take this into account, the gas volume flow at the bottom is combined with the conversion ratio at the specific height. The volume will therefore increase as one methane molecule converts into two hydrogen molecules:

$$\dot{V}_g = \dot{V}_{g,b}\left(1 + \varepsilon X_{CH_4}\right)\left(\frac{P_b}{P}\right)\left(\frac{T}{T_b}\right) = \left(\dot{n}_{CH_4,b} + \dot{n}_{H_2,b} + \dot{n}_{I,b}\right)\left(1 + \varepsilon X_{CH_4}\right)\left(\frac{RT}{P}\right) \quad (2.21)$$

Dividing the actual gas volume flow over the cross-sectional area of the reactor, a circular reactor in this research results in the superficial gas velocity. Representing the average velocity of the gas flow through the molten fill of the reactor at a specific height:

$$j_g = \frac{4\left(\dot{n}_{CH_4,b} + \dot{n}_{H_2,b} + \dot{n}_{I,b}\right)\left(1 + \varepsilon X_{CH_4}\right)}{\pi D^2}\left(\frac{RT}{P}\right) \tag{2.22}$$

Interfacial area of gas bubbles

Measuring the gas bubble size to determine the related interfacial area in the opaque liquids, e.g., molten metal, is difficult as earlier discussed in the last paragraph of Subsection 2.1.2 Gas holdup in molten metals. However, a few methods exist based on acoustics or pressure differences. Jamailahmadi et al. (2001) made an empirical correlation for bubble size in systems with water, water-alcohol or water-glycerol as liquid fill of the reactor. This has been compared to bubble measurements of helium bubbles in tin for a molten metal bath with a temperature between 400 and 700 ˚C and showed to be quite accurate as the average deviation was just below 5% (Sun et al., 2020). It is assumed that the conditions can be used in general more widely range of fluids. Correlations derived from liquids with lower density and surface tension are also be applied to the molten metal reactor in this research.

Since the bubbles are not perfect spheres and differ in size, the interfacial area ag (m^2 reactive surface.m^{-3} gas) is calculated based on the Sauter Diameter, d_{vs}. The Sauter diameter (m) averages the diameter of all bubbles to represent a flow of bubbles that has the same volume/surface area ratio as the entire flow. A_g, therefore, is described by:

$$a_g = \frac{6}{d_{vs}} \tag{2.23}$$

Catalan and Razaei (2022) have applied the correlation for d_{vs} experimentally found by Akita and Yoshida (1974). This research based their correlation on bubble size measures at 1.5 m in three different squared tanks with a side length (D = 0.077m, D = 0.15 and D = 0.3 m). The correlation is based on lower density and surface tension liquids, but as stated before, this should still make a relatively good estimation on the behaviour in molten metals. Moreover, the measured height is substantially above the reactor bottom and, therefore, the bubbles are independent of the initial bubble size which is defined by the orifice:

$$\frac{d_{vs}}{D} = 26\,(N_{bo})^{-0.50}\left(N_{ga}\right)^{-0.12}\,(N_{Fr})^{-0.12} \tag{2.24}$$

The correlation depends on the reactor size and three dimensionless parameters: (i) Bond number (N_{bo}), (ii) Galilei number (N_{ga}) and (iii) Froude number (N_{Fr}). These parameters depend on the liquid properties of the medium, the shape of the reactor and the gas flow superficial velocity.

First, the Bond number N_{bo}, quantifies the importance of surface tension and gravitational forces. In previous calculations of the Bond number on the same reactor fill, the Bond number was below one. This typically indicates a system that is surface tension dominated.

Second, the Galilei number N_{ga} determines the importance of viscous forces acting on the bubble in relation to gravitational forces. The Galilei number is a suitable parameter to describe rising bubbles as, in contrast to for instance the Reynolds or Weber number, a precise bubble velocity is not necessary. That would be impossible with the varying bubble size in the reactor.

Third, the Froude number N_{Fr} defines the ratio between inertia forces and gravitational forces. Since the superficial velocity of the flow enhances the inertia of a bubble, the effect of this parameter on bubble size is taken into account via the Froude number.

$$N_{Bo} \equiv \frac{gD^2\rho_l}{\sigma} \tag{2.25}$$

$$N_{ga} \equiv \frac{gD^3}{{v_l}^2} \tag{2.26}$$

$$N_{Fr} \equiv \frac{j_g}{(gD)^{0.5}} \tag{2.27}$$

The only new term is the liquid kinematic viscosity v, which is the dynamic viscosity divided by the liquid density.

Akita and Yoshida found that their correlation was in agreement with experimental data they acquired in previous work (Akita & Yoshida, 1973) where wider variations of system properties, column size, and superficial gas velocity were tested. Hence, the d_{vs} correlation was experimentally validated for the dimensionless parameters by combining the results of their two articles within the ranges N_{bo} = 7.98 e^2 – 4.85 e^4, N_{ga} = 6.25 e^6 – 1.79 e^{10} and N_{Fr} = 8 e^{-4} – 1.35 e^{-1}.

2.1.4 Expansion of the differential material balance equation

The catalytic and non-catalytic reaction rate, Rc and Rn, and the gas holdup have been related to the material properties or to the parameters related to the reactor design. The differential material balance can be written in the following form:

$$\begin{aligned}\dot{n}_{CH_4}\frac{dX_{CH_4}}{dL} = \frac{\pi D^2}{4}\Bigg\{&\frac{a_g\, k_{c,f}(1-\mathrm{X_{CH_4}})}{\left(\dot{n}_{CH_4,b}+\dot{n}_{H_2,b}+\dot{n}_{I,b}\right)\left(1+\varepsilon X_{CH_4}\right)}\left(\frac{P}{RT}\right)\\ &+k_{n,f}\left[\frac{(1-\mathrm{X_{CH_4}})}{\left(\dot{n}_{CH_4,b}+\dot{n}_{H_2,b}+\dot{n}_{I,b}\right)\left(1+\varepsilon X_{CH_4}\right)}\left(\frac{P}{RT}\right)\right]^n\Bigg\}\\ &\cdot\left\{1-\frac{\dot{n}_{CH_4,b}\left(\theta_{H_2}+2X_{CH_4}\right)}{\left(\dot{n}_{CH_4,b}+\dot{n}_{H_2,b}+\dot{n}_{I,b}\right)\left(1+\varepsilon X_{CH_4}\right)\left(1-X_{CH_4}\right)\cdot K_c}\left(\frac{P}{RT}\right)\right\}\end{aligned} \tag{2.28}$$

All parameters can be determined by the equations stated in the previous paragraphs of the section in combination with the metal and gas material properties and the reactor dimensions from the design.

These properties and dimensions are constant over the height of the reactor except for the gas density as the molar mass of the gas changes (M_g). The rising gas bubbles are exposed to an increasing hydrogen content as methane converts, resulting in a lower weight and a lower volume (one mole CH_4 converts to two mole H_2):

$$\rho_g = \frac{PM_g}{RT} \tag{2.29}$$

where:

$$\begin{aligned} M_g &= \frac{C_{CH_4}M_{CH_4} + C_{H_2}M_{H_2} + C_I M_I}{C_{CH_4} + C_{H_2} + C_I} \\ &= \frac{\left(1 - X_{CH_4}\right)M_{CH_4} + \left(\theta_{H_2} + 2X_{CH_4}\right)C_{H_2}M_{H_2} + \theta_I C_I M_I}{1 + \theta_{H_2} + X_{CH_4} + \theta_I} \end{aligned} \tag{2.30}$$

where M indicates the molar masses ($kg.mol^{-1}$) of the respective molecules (methane, hydrogen or an inert molecule such as nitrogen), C represents the concentration of the respective molecules and the θ is the mole ratio of the molecule with regards to methane in the inflow of the reactor at the bottom.

The system that constitutes these coupled differential equations can be numerically solved due to the known boundary conditions at the bottom. Resulting in the methane conversion and pressure at varying heights, with the methane conversion at the top of the reactor as prime interest.

2.1.5 Replication validation

The discussed coupled system of differential equations has been coded in python to mimic the approach of Catalan and Razaei. Before expanding the model, the results were validated to determine how accurate the model is. The validation compares results from the replicated model to figures from the last paper. By showing that the results are accurately aligned the replication, it proves the replicability of Catalan and Razaei their research.

For the validation, a reactor operating at 1040 ˚C and 2 bar (equivalent to 200 kPa) feed pressure filled with $Ni_{0.27}Bi_{0.73}$ was used. The 0.03m in diameter and 1.15 m in height reactor was fed with a 10 cm^3 $_{(STD)}$/min gas mixture consisting of 80 mol% CH_4 and 20 mol% argon. The conditions match the conditions of the below graphs of Figure 2.5 coming from the last paper (Catalan & Rezaei, 2022).

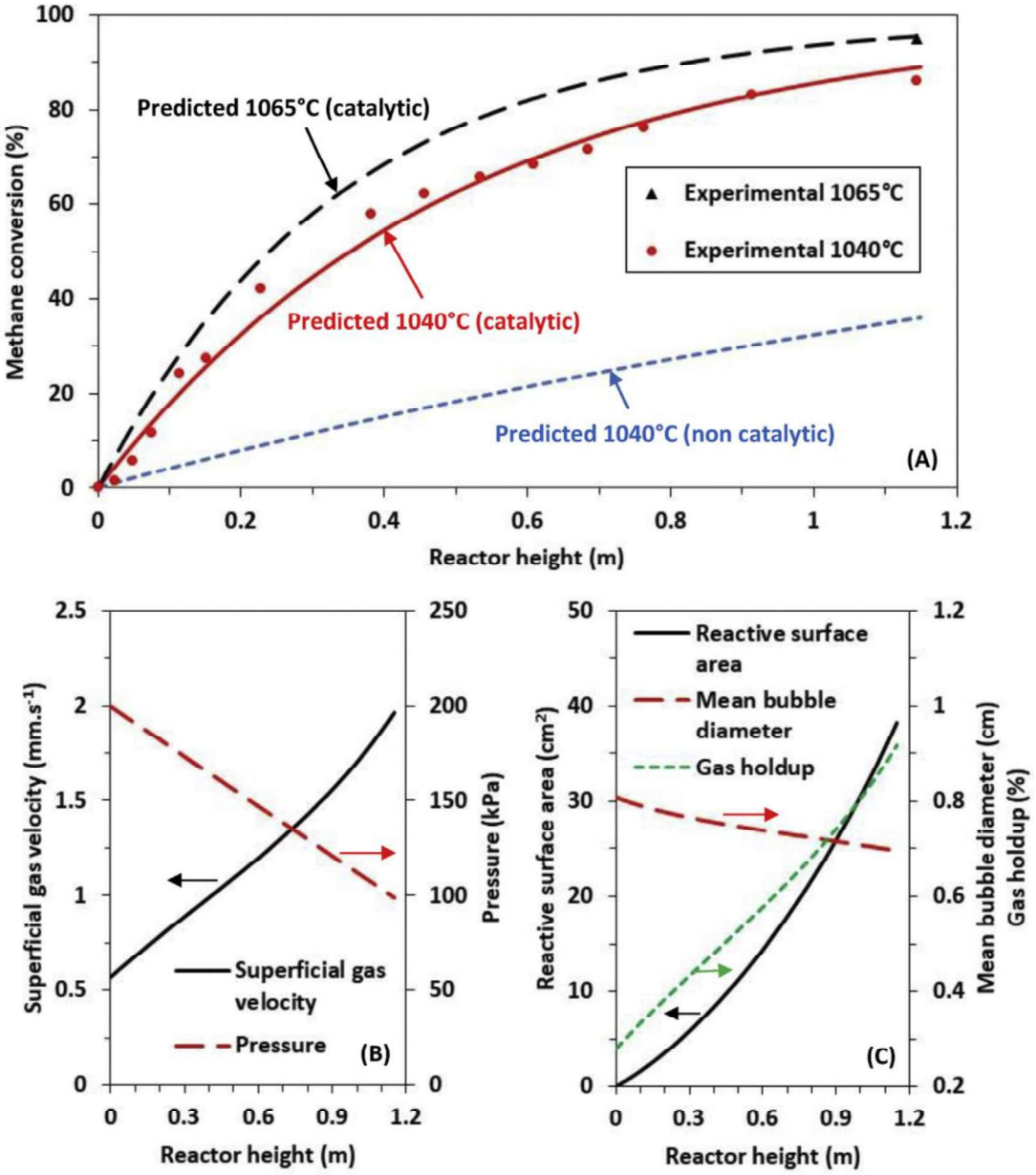

***Figure 2.4**: The profiles show (A) methane conversion, (B) superficial gas velocity and pressure, and (C) mean bubble diameter, gas holdup and reactive surface in a 0.03 m in diameter and 1.15 m in height reactor at 1040 °C. Operating at 2 bar (equivalent to 200 kPa) and with a 10 cm3 mixture feed consisting of 80 mol% CH_4 and 20 mol% argon. The figure is made by Catalan and Rezaei (2022) in which their predictions are compared with the experimental results from Upham et al. (2017) shown as markers, therefore, the conversion at 1065°C is added in (A).*

The results from the replicated model in python are shown in Figure 2.6, in a similar style and fashion to make a visual comparison possible.

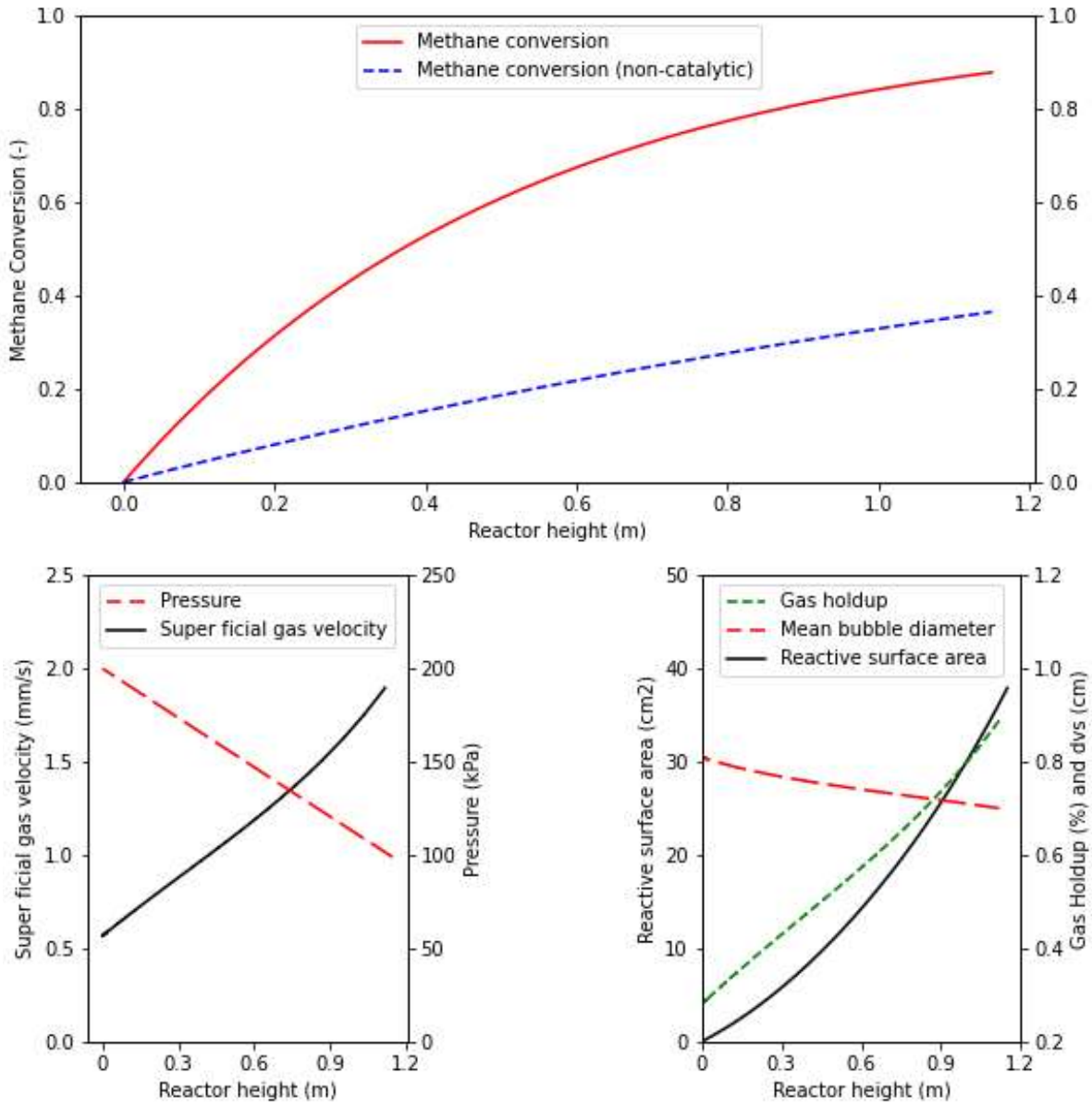

Figure 2.5: *The profiles show (A) methane conversion, (B) superficial gas velocity and pressure, and (C) mean bubble diameter and gas holdup in a 0.03 m in diameter and 1.15 m in height reactor at 1040 °C. Operating at 2 bar (equivalent to 200 kPa) and with a 10 cm3 mixture feed consisting of 80 mol% CH_4 and 20 mol% argon. The figure is generated in python to compare the replicated model with the original coding from Catalan and Rezaei (2022), which is shown in Figure 2.5.*

Comparing Fig.5 with Fig.6 directly the identical appearance of both figures stands out, indicating that the model is accurately replicated. As this suggestion is solely based on a visual comparison, a discussion with Lionel Catalan was arranged to strengthen the support for this conclusion (Catalan, 2022). The discussion resulted in the same conclusion, therefore, the model was applied as basis for expansions and utilized further in the rest of this research, to eventually design an offshore methane pyrolysis installation.

2.2 Modelling of the transition zone and sparger plate

One of the aspects that has been simplified in Catalan and Razaei their model is the transition zone. This zone extends from the bottom of the reactor until the height where the bubbles are no longer affected by the inlet. The bubble size varies in this zone due to continuous coalescence and break-up of the bubbles. At the bottom, the size equals the small local bubble size that is determined by the inlet of the reactor. Over the height, due to a large number of bubbles, more bubbles will coalesce than breakup resulting in an overall increase in bubble size until the balance is achieved at the top of the transition zone.

Catalan and Razaei assume it only covers the first few centimetres and therefore neglect it. However, even though this transition zone could be limited in size, the fact that the tiny bubbles result in a major increase in interfacial area of the gas bubbles, a large percentage of the total conversion could happen close to the bottom. These tiny bubbles are made by a sparger and the dominant effect has been seen in Serban et al. (2003) where the conversion ratio at the top of the reactor increased by over 40% due to the addition of a Mott sparger in comparison to a single hole injector.

This section will first investigate the transition zone to determine when the flow of bubbles reaches the top of the transition zone, and also how the gas bubbles behave from the bottom to the end. Secondly different possible spargers are discussed to see how a specific design varies the results. Both topics should in the end lead to an improvement of the model, with increased reaction rates at the bottom of the reactor.

2.2.1 Transition zone

Due to the optical test limitations of the opaque molten metals, the acquisition of data on the bubble size and gas holdup in molten metals is limited and within the rare research that was available, none has been found that quantifies the transition zone in these conditions. In Fig. 6 for instance, the behaviour in the bottom 200 mm of a 530 mm tank is shown, however the flow profile of the bubbles still changes with the height at the top of this figure, indicating the end of the transition zone was not yet reached.

Taking into account the current situation, research on bubble behaviour and gas holdup in the transition zone in low density liquids is utilized under the same assumptions as in subsection Interfacial area of gas bubbles from 2.1.3. Thorat et al. (1998) created a test set-up with air-water and two air-salt solution systems. The research examined the transition zone in bubble columns by measuring gas holdup and visually analysing the bubble behaviour by lowering the static surface height for varying flow velocities. As the liquid surface height was alternated it created eight test variations with a Hd/D ratio from one to eight.

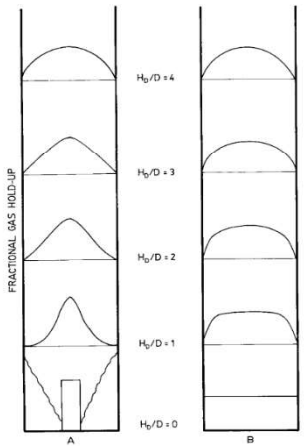

Figure 2.6: *Bubble distribution for single (A) and multipoint sparger (B) (Thorat et al., 1998)*

Tested for flow velocities up to 0.3 m/s, both for single and multipoint spargers, the bubbles reached an equilibrium regarding coalescence and breakup of the gas bubbles at a reactor height of approximately Hd/D = 5. The effect of a sparger will, therefore, be taken into account until the top of the transition zone in the model. The turbulent behaviour in the transition, however, makes it extremely difficult to describe the gas holdup and bubble size change between the bottom of the tank and Hd/D = 5. It is worth noting that a balance between bubble breakup and coalescence does not necessarily occur beyond the transition zone in a methane pyrolysis bubble tank. Due to the larger decrease in pressure when rising, related to heavy fill, and additional methane conversion, the volume flow could still significantly increase. Eventually, this could lead to bubble breakup forced by the surface tension on the bubble surface.

2.2.2 Sparger design

The addition of a sparger to the model should modify the bubble size and gas holdup in the transition zone. Even though the bubble behaviour in the transition zone is extremely difficult to describe, at the bottom they are strongly determined by the sparger. The correlation between the initial bubble diameter, d_b, and orifice diameter, d_o, in molten metal has been determined by Andreini et al. (1977). The correlation is based on data acquired in molten Tin, Lead and Copper and, therefore, assumed to be applicable for the current system with $Cu_{0.45}Bi_{0.55}$ or $Ni_{0.27}Bi_{0.73}$:

$$\frac{d_b}{d_o} = (N_{Fr,o})^{0.224}(N_{we,o})^{-0.109} \tag{2.31}$$

Where d_o is the hole diameter of the orifice, $N_{Fr,o}$ the Froude number of the orifice, and $N_{we,o}$ the Weber number of the orifice. N_{Fr} is the same formula as seen before (Equation 2.27) and the $N_{we,o}$ is described by:

$$N_{we,o} = \frac{d_o {U_o}^2 \rho_g}{\sigma} \tag{2.32}$$

Andreini et al. also found the velocity of the initial bubbles ($cm.s^{-1}$) to be described by:

$$U_b = 29.69(d_b)^{0.316} \tag{2.33}$$

There are various designs for spargers in bubble columns, however, to create the most uniform distribution a plate can best be installed. This can be seen in Fig. 7 where the gas bubbles are much better distributed over the width of the column.

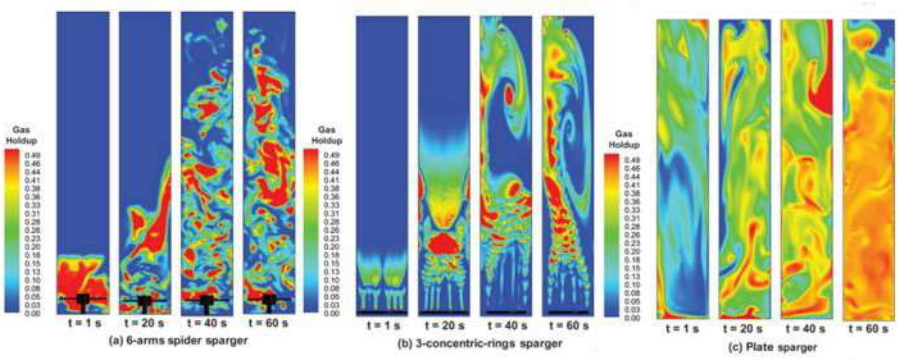

Figure 2.7: *Gas distribution in bubble columns for different sparger: 6-arms spider sparger, 3 concentric rings sparger, plate sparger (Basha & Morsi, 2017)*

For the plate sparger, the two available options have been implemented in the model: a perforated plate and a porous plate. The largest difference between the two is the hole size, as the perforating holes are larger compared to the natural micro size pores of porous material. The smaller holes of the porous plate, result in smaller bubbles at the bottom of the reactor and thereby in superior conversion performance therefore this design will be discussed.

The ceramic metal used to produce porous spargers can operate at temperatures up to 1500 ˚C (Mott Corporation, 2022). In order words catalytic methane pyrolysis is well in the operating range of the material, this also counts for the pressure range. The hole size and porosity resulting from the selection of the ceramic metal consequently determines the gas flow through each hole. The micro size of the pores comes from Serban et al. (2003) and is set to 0.5 μm. The porosity is set to 40% by consulting with a methane pyrolysis expert (Goetheer, 2022b).

2.2.3 Model expansion with transition zone and sparger plate

Since no correlations for bubble size and gas holdup over the height of the transition zone have been found, two different implementations have been proposed to include a transition zone and sparger in the model. Both are be introduced in this paragraph and compared. The implementation that results in the most comparable results to what has been seen in experiments, is kept as a permanent expansion of the replicated model from 2.1 Modelling of hydrodynamics and kinetics.

Implementation 1

The first implementation only adjusts the bubble size in the transition zone. At the bottom, the Sauter diameter will equal the d_b calculated by Equation 2.31, as all bubbles are assumed to have the same diameter just above the sparger plate. Afterwards the d_b will increase linearly to the Sauter diameter at L = 5D. Subsequently, the superficial gas velocity is still based on the gas flow in the tank and thereby the correlation for the gas holdup stays the same as outside the transition zone.

Implementation 2

The second implementation adjusts both the bubble size and gas holdup in the transition zone. The Sauter diameter follows the same method as option 1 and is equal to d_b at the bottom and aligns with the replicated model from L=5D on. The initial bubble size can be converted to an

initial bubble velocity by Equation 2.33 and as the initial bubbles are all the same size this equals j_g. The velocity, just as the mean bubble diameter, will increase linearly to equal the original superficial gas velocity at L=5D. The gas holdup is, following the current formula, directly related to the superficial gas velocity, meaning the gas holdup will differ in this option.

To compare the two implementations with each other and the original situation, a similar situation as Fig. 5 has been analysed. In Fig, 5, the conditions result in a system that performs close to the reaction equilibrium. The effect of the additional conversion in the bottom of the tank due to the sparger plate and transition zone would, therefore, be less visible in the overall conversion ratio. As a result, the low gas inflow and pressure but also the high H/D ratio are modified, to create a system that performs further from the maximum conversion, i.e., the methane hydrogen ratio at reaction equilibrium.

The gas inflow is set to 10.000 $cm_{(STP)^3}$/min, the pressure is set to 10 bar and the results are generated for both 0.4 m height and 1.15 m height to show the relative influence of the sparger plate and transition zone is larger when the height is reduced. The temperature at 1040 ˚C and the feed composition, consisting of 80 mol% CH_4 and 20 mol% argon, are the same as Fig. 5

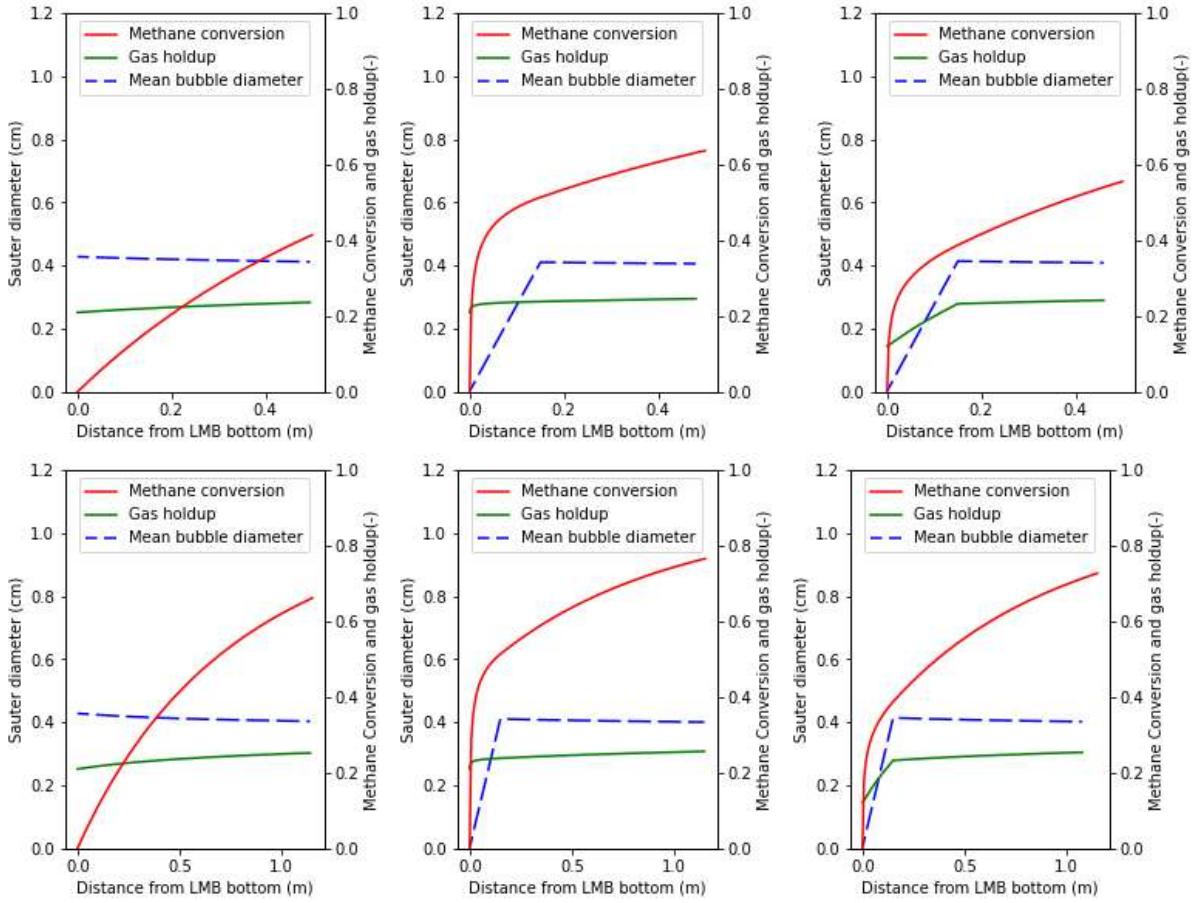

Figure 2.8: *Model results with different implementations of the transition zone and sparger plate in a 0.03 m diameter tank operating at 1040 C and 10 bar. The flow consists of 80 mol% methane and 20 mol% argon. From left to right the results for the replicated model, implementation 1 and implementation 2 have been visualized with at the top a reactor height L = 0.4 m and at the bottom 1.15 m.*

Independent of the way the sparger plate is integrated with the model, it shows a significant increase in methane conversion. Due to the small bubbles, the interfacial area at the bottom of the reactor is massively increased transferring a large portion of the total conversion to this region. This also explains the relatively larger contribution to the conversion by the sparger plate when a shorter reactor is considered, as only a small part of the conversion is acquired in the top region.

In all graphs, a slightly decreasing mean bubble diameter (Sauter diameter) can be identified in the part of the reactor outside the transition zone, e.g., above L = 0.15 m. This can theoretically be explained by the Froude number (N_{Fr}) in Eq. 26. The empirically found correlation states that with an increasing superficial gas velocity, the $(N_{Fr})^{-0.12}$ decreases and, consequently, the mean bubble size. A physical explanation for this phenomenon is harder to assess. Potentially the increase in volume flow could be brought forward. As the volume of the bubble increases, the bubbles become more susceptible to breaking up, potentially resulting in a decrease in the Sauter diameter of the gas flow.

An analysis of the methane conversion in both implementation 1 and implementation 2 reveals that the primary conversion occurs near the bottom of the reactor, where the bubble diameter is the smallest. This is in line with the background of the transition zone and sparger plate. Therefore, the comparison between the different implementations will be based on the difference in the gas holdup. The design of implementation 1 results in a rapid increase in gas holdup in the beginning and diminishes over the reactor height. This comes as no surprise taking into account that conversion is the driving force behind the volume flow increase. The adjustments to the flow velocity in implementation 2 result in a linear gas holdup increase. This linear increase ends at L = 0.15 m where the gas holdup aligns with the gas holdup correlation from the original replicated model. When comparing this gas holdup behaviour with the neutron radiology from Fig. 4, the actual behaviour is far from linear in this region. The ongoing convection and coalescence and breakup lead to a different trend than linear. Therefore, implementation 2 does not accurately describe the behaviour regarding gas holdup in the transition zone.

2.2.4 Results of implementation and Discussion/ Limitations:

Modelling the effect of a sparger plate at the bottom of the reactor until the end of the transition zone, results in the desired improvement in the methane conversion due to the higher gas-liquid interfacial area of the small bubbles, especially at the bottom, which has been seen in previous experiments (Leal Pérez et al., 2020) and also brought forward by methane pyrolysis experts (Goetheer, 2022b). From a design perspective, this offers the opportunity to decrease the height of the tank as most reactions happen near the bottom. Bringing the actual and model gas holdup behaviour closer together was harder, especially in comparison to what happens according to Hibiki et al. (2000). To maintain the quality of the model, the original correlation between gas holdup and the superficial gas holdup is maintained over the entire reactor heigh. In other words, implementation 1 is utilized to include the transition zone and sparger plate. It is important to note that there is some change in behaviour in the original gas holdup. This change is due to the increased volume flow, which is related to the early conversion of methane. As a result, the gas holdup is still indirectly affected.

2.3 Modelling of molten salt layer

The main goal of the molten salt layer is to reduce the metal content in the solid carbon. As a side catch some extra conversion could result from the additional residence time. As the molten metal is washed in the molten salt layer, it is separated from the solid carbon and falls back into the molten metal layer below due to its larger density.

To select the best salt, four characteristics should be taken into account. (i) With solid carbon removal at the top of the reactor, the density should be between the carbon and molten metal. (ii) Wetting of the carbon by the salt can be a problem therefore a low adhesion to carbon is preferred. (iii) The residence time in the salt wash should be long enough to wash the metal. (iv) A melting point below and low vapour pressure at the operational temperature. Especially NaBr and NaCl are preferable salts due to their low wettability and can be separated by flotation from the carbon when necessary, therefore, in the remaining part of the section, these two salt will be considered (Bhardwaj et al., 2019; Rahimi et al., 2019).

2.3.1 Parameters of a salt layer

Due to the change in properties between the metal and salt layers, the various parameters e.g., density, surface pressure, and viscosity, should be modified when the gas transfers through the metal-salt interface. The material properties of both molten NaBr and NaCl can be found in Appendix A2.

Possible both the non-catalytic and catalytic conversion in the molten salt layer attributes to the overall performance of the reactor. To quantify the added conversion for NaBr and NaCl, the catalytic activation energy and catalytic forward reaction rate will be integrated into the model in the next paragraph.

Parkinson et al. (Parkinson, Patzschke, Nikolis, Raman, & Hellgardt, 2021) have investigated the catalytic behaviour of different salt during methane pyrolysis, including NaBr, and NaCl. The behaviour was determined for the range 900-1000 ˚C, however as the operating temperature of a methane pyrolysis reactor could be higher also the behaviour outside this range is to be known. The operational temperature is expected to stay within a reasonable range, up to around 1050 ˚C, therefore, the materials are assumed to react similarly, and the current correlations are implemented.

Table 2.3: *Catalytic behaviour of molten NaCl and NaBr, determined in a 900-1000 ˚C temperature range (Parkinson, Patzschke, Nikolis, Raman, Dankworth, et al., 2021)*

Salt	Units	NaCl	NaBr
$k^0{}_{c,s}$	m.s-1	2.1×10^5 [a]	1.3×10^7 [b]
$E^a{}_{c,s}$	j.mol-1	231,300	277,600

The pre-exponential factor is converted according the same method as Table 1.

[a] With a d_b = 0.00564 m in the experiment for NaCl. The research found a pre-exponential factor $k^0 = 2.2 \times 10^8\ s^{-1}$

[b] With a d_b = 0.00545 m in the experiment for NaBr. The research found a pre-exponential factor $k^0 = 1.4 \times 10^{10}\ s^{-1}$

2.3.2 Implementation in model

To effectively filter the metal from the carbon molecules, the salt layer must have a significant height. After a consult with a methane pyrolysis expert, the salt layer height in the model is set to 25% of the total liquid height (Goetheer, 2022a).

Both non-catalytic and catalytic conversion contribute to the salt layer, however as the non-catalytic conversion happens inside the bubble, the R_n stays the same for both metal and salt. The catalytic parameters are adjusted in the salt layer since the catalytic forward rate coefficient depends on the medium surrounding the gas bubbles and that changes. The coefficient again follows the Arrhenius equation (Upham et al., 2017), therefore, the equation looks similar to Equation 2.7 however it takes the salt characteristics into account:

$$k_{c,s} = k_{c,s}^{0} \exp\left(-\frac{E_{c,s}^{a}}{RT}\right) \tag{2.34}$$

Extra attention has been given to the change from metal to salt, considering the current correlation for gas holdup in the replicated model has been assessed in molten metal. Therefore, also an additional correlation has been considered to identify which method would be best applicable in a molten salt layer. This correlation has been found in $NaNO_3$ and KCl (Sada et al., 1984), nevertheless, it is assumed to be applicable for NaCl and NaBr as the E_a and $K_{c,s}$ of KCl lie in the same range as NaCl and NaBR:

$$\frac{\alpha}{(1-\alpha)^4} = 0.32(N_{bo})^{0.121}\left(N_{ga}\right)^{0.086}\left(\rho_g/\rho_l\right)^{0.068} N_{Fr} \tag{2.34}$$

Where N_{bo} is the Bond number, N_{ga} the Galilei Number and N_{Fr} the Froude number for the salt layer. The ρ_g and ρ_l represent the density of respectively gas and the applied salt at the operational temperature.

2.3.3 Effect on reactor behaviour

The model, including the transition zone and sparger plate, was executed twice to facilitate a comparison between the two correlations for gas holdup in the salt layer. The first time, the original correlation assessed for molten metal applies across the entire height. The second time the molten metal correlation applies until the interface between metal and salt, afterwards the correlation from Eq. 34 is utilized. NaBr is applied since it is more catalytic and denser as fill than NaCl and, therefore, comes closer to the metal properties of the first 75% of the reactor. In this comparison, the same conditions are utilized as in Subsection 2.2.3, therefore the reactor is 0.03m in diameter and 1.15 m in height and operates at 1040 ˚C. The 10,000 $cm^3_{(std)}$/min gas flow has a composition of 80 mol% CH_4 and 20 mol% argon and bottom fed at 10 bar.

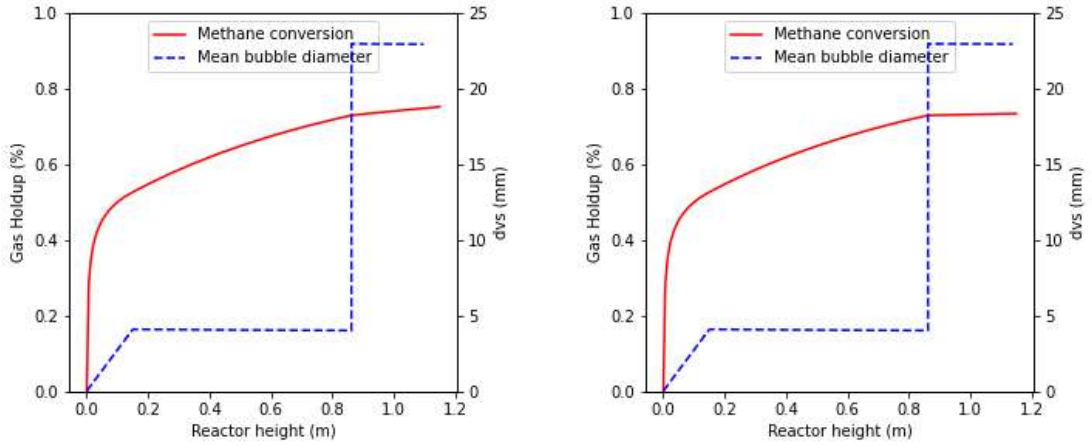

Figure 2.9: *Model results for different correlations for the gas holdup in the top salt layer of the molten metal and salt reactor*

Due to the addition of the salt layer, the top 25% of the liquid has different properties in comparison to the first 75% filled with metal. This influences the various parameters. When the reactor was completely filled with methane the top conversion reached 77.4%, however, the salt reduces the conversion. A kink in the methane conversion can be identified in Figure 2.9 at 0.8625 m, which corresponds to the height of the interface between metal and salt for a 1.15 m reactor completely filled with liquid. At the interface, 73.0% was converted. With salt the increase in conversion was reduced over the last 25% to only 2.3% in Figure 2.9a and 0.5% in Figure 2.9b The decrease in conversion has multiple explanations. As the salt layer will be at top of the reactor, a large portion of the methane molecules has already been converted into hydrogen assuming a high conversion rate is in place. The additional conversion acquired at the top is therefore limited. Also, the reduced catalytic activities of NaCl or NaBr in comparison to metal further diminishes the conversion in this region. Overall, the conversion change in the salt layer is assumed to be neglectable. The conversion present in Figure 2.9a can be allocated to the unrealistic high gas holdup (see Figure 2.10) as this is not present in Figure 2.9b where the gas holdup is much lower.

The size of the gas bubbles is determined by multiple parameters which also include the properties of the surrounding liquid. As these properties change when the bubbles pass from the molten metal layer to the molten salt layer, the mean bubble diameter thereby also changes. Especially, the density of the liquid has a large influence (Scheiblehner et al., 2022). In higher liquid densities the bubble diameter tends to be smaller. In line with this background, the mean bubble diameter in Figure 2.9a and 2.9b increases when the bubbles pass through the interface. Entering the relatively low-density salt, in comparison to the high-density metal.

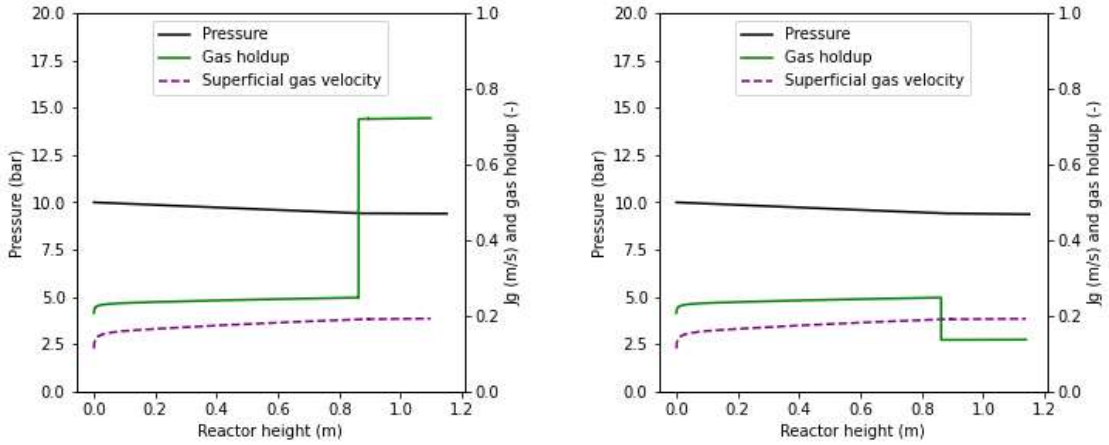

Figure 2.10: *Model results for different correlations for the gas holdup in the top salt layer of the reactor*

Since the volume stays the same, considering no step in conversion or pressure is noticed over the interface, the superficial gas velocity and, therefore, the gas flow does not differ. This continuous flow is also seen in Figure 2.10.

For the gas holdup, an upward step has been recorded in Figure 2.10. Taken into account, the superficial gas velocity has no step in the current conditions, a sudden change in gas holdup is not expected and the correlation for gas holdup assessed in molten metal does not work for molten salt. As a result, Equation 2.34 becomes relevant, which is a correlation for gas holdup in molten salt. Consequently, from the height of the metal-salt interface, this correlation has been implemented in the model instead of the original correlation assessed in molten metal. Since the same condition for gas flow again applies, a sudden step is still not expected. The results in Figure 2.10b still show a step. Even though it is downward this time, the correlation from Equation 2.34, therefore, also does not seem to accurately describe the expected behaviour regarding gas holdup in a molten metal and salt reactor.

2.3.4 Results of implementation and discussion

Replacing the molten metal with molten salt in the top 25% of the liquid height decreases the conversion in this region significantly. The conversion becomes so small that the layer is considered not necessary for determining a valid methane conversion at the top of the reactor. Not only does the salt layer in the model not contribute to the conversion ratio, but also the model expansion with salt has shown to be discontinuous with the current gas holdup correlations. Even examining a new gas holdup correlation, specifically for molten salt, modelling of the molten salt layer does still not align with the gas holdup at the top of the molten metal layer. Hence both correlations seem inapplicable to represent gas holdup in a molten salt layer. Based on the two arguments, the contribution of salt is neglected and excluded from the model.

As the goal of the model was to describe a molten metal and salt model, salt should come in somewhere to make the model applicable for its purpose. The molten salt layer will therefore be included as a physical layer to include the size and weight. The model is run until 75% of the liquid height, afterwards, the parameters, e.g., methane conversion, gas holdup, etc., are assumed to remain the same for the last 25%.

2.4 Model final results, discussion and limitations

Altogether, the effort to create a design tool for an offshore methane pyrolysis installation has led to a replication and expansion of the coupled hydrodynamic and kinetic model by Catalan and Razaei (2022). In this last section of chapter 2, final results, a discussion and limitations are presented. The conclusion explains the findings of the research and their implications on the coupled model and how the results should be interpreted. In the discussion, the model is validated with experimental research on molten metal and salt methane pyrolysis. The section is completed with a listing the model limitations to make sure the model is applied within the operating conditions.

2.4.1 Final results

The original model by Catalan and Razaei couples the properties of the gas and reactor fill with the characteristics of methane pyrolysis. This results in a combination of theoretical and experimental correlations that jointly determine the methane conversion at the top of the reactor. Since these experimental correlations are prone to test set-up boundaries, especially the kinetic correlations, result in multiple limitations of the model.

Research implications

Taken into account the extremely small bubble size at the bottom, due to the holes (in the sparger plate) the gas is injected through, which initially has been disregarded and assumed to be in balance with the hydrodynamics of the surrounding medium. As the literature indicates this is not the situation when selecting the right sparger plate for injection in the reactor. The model has been expanded with a transition zone and sparger plate, to include the small bubble sizes at the bottom as they have a large influence on the top methane conversion in the reactor. The transition zone is the region where bubbles continuously coalesce and break up which results in varying bubble diameters and gas holdup in this bottom region. Due to this seemingly chaotic behaviour, no proper correlation has been found in previous research to describe both parameters. Therefore, to describe the mean bubble diameter, the assumption has been made that it grows linearly grows from the bottom bubble diameter, defined by the sparger plate, to the balance diameter at the end of the transition zone. Furthermore, to describe the gas holdup the original correlation has been kept in place, relating the gas holdup to the velocity of the gas flow as adjustments did not improve the model. The transition zone extends to a height with a relatively steady motion that is not influenced by the bottom but just by the change in conversion and pressure. Due to a lack of information on this height in molten metals, the height is based on experiments in lower density and viscosity liquids and set to L = 5D.

With 1.3 Research background in mind, which indicated a molten metal and salt reactor as best methane pyrolysis technology, the replicated model should not only apply to molten metal but also to molten salt. As the latter was not yet included, the model was tested for these conditions. Firstly, the model showed that methane conversion in a top salt layer was neglectable. Secondly, the gas holdup did not align with the preceding gas holdup in the molten metal layer. The current correlation, based on metal experiments, led to a large jump in gas holdup when passing through the interface between the metal and salt, even though the gas holdup is expected to be a continuous function. When incorporating a different gas

holdup correlation in the molten salt layer, specifically determined in molten salt, the jump turned into a drop in gas holdup. Still resulting in discontinuous gas holdup behaviour. Since both efforts did not succeed the choice has been made to include salt outside the model by assuming the parameters, e.g., conversion, gas holdup, do not change after the interface between metal and salt. The molten salt layer is, therefore, solely in place to separate the molten metal from the carbon particles.

Interpretation of model

Overall, the final model that embedded the principles from Catalan and Razaei extended with the transition zone and sparger plate determines multiple parameters of the height of the reactor based on the operating and starting conditions. These include the methane conversion, pressure, superficial flow velocity, gas holdup and mean bubble diameter. The main goal of the model is to predict the methane conversion at the top of the reactor, therefore, the output, can be reduced to only print that specific figure. The parameters can be determined for different conditions and reactor designs. The variable input parameters are volume, composition and pressure of the gas feed, reactor temperature, reactor fill and reactor dimensions (diameter and height). The reactor is always a cylinder with a bottom feed and the reactor fill is assumed to reach the top of the reactor.

2.4.2 Discussion

In this final paragraph, on the modelling of methane pyrolysis, the results of the model are validated, and limitations of the variable input parameters are discussed. All to get a comprehensive idea of the boundaries of the model for future research. This discussion starts with the validation and afterwards, the limitations are examined by discussing each step separately. These shortcomings should be taken into account as exceeding the set limits would result in calculated operating conditions beyond the validated ranges, hence leading to results with unknown accuracy.

Validation

The model is validated by recent research listed in the paper "Recent Advances in Methane Pyrolysis: Turquoise Hydrogen with Solid Carbon Production" (Korányi et al., 2022). This contained one research that utilized a molten metal and salt reactor with the same reactor fill as the current model is designed for (Noh et al., 2022). The results are listed in Table 4 with two different inflows in the reactor.

Table 2.4: *Top methane conversion ratio in 8mm diameter molten metal and salt reactor at 985 ˚C and ambient pressure. The reactor is filled with a 65mm $Ni_{0.27}Bi_{0.73}$ layer and a 31mm NaBr layer.*

Research	$\dot{n}_b = 9\ sccm$ [a]	$\dot{n}_b = 18\ sccm$ [a]
Noh et al. (2022)	32.1%	18.6%
This research (Current model) [b]	13.2%	12.5%
This research (Model by Catalan and Razaei)	4.5%	4.4%

[a] The flow, in standard cubic centimetre per minute (sccm) at the bottom of the reactor has a 2:1 ratio CH_4:Ar
[b] The hole diameter of the porous sparger plate is modified to d_b = 3μm, hence it matches the diameter of the sparger plate in Noh et al. (2022).

The model results in conversion ratios differing from the experimental test results. These differences have multiple explanations. First, the reactor in the experimental test setup has a total height of 650 mm. Leaving a massive headspace for non-catalytic methane decomposition. Second, as the flow turns into bubbles in the molten medium, it is much less dependent on the volume of the flow, however, in the free-flowing headspace, this is not the case. The differences can therefore become much larger when considering a different inflow. The conditions of the experiment are also applied to the original coupled model from Catalan and Razaei. The model of course includes no sparger plate, therefore, the hole diameter of the porous plate cannot be implemented. The results indicate a methane conversion even further away from the ratio found in the experiments.

Considering just 4.5% of the 32.1% happens in the first 96 mm, the number of reactions in the molten medium and the free-flowing headspace is comparable relative to the height. Since the molten medium is added to foster the conversion and at the bottom, the number of reactions is always higher due to the abundant number of unconverted methane molecules, a much higher ratio would be expected. This behaviour is better represented in the current model with a transition zone and sparger plate as the 13.2% accounts for around 40% of the total conversion for $\dot{n}_b = 9\,sccm$ and even 67% for $\dot{n}_b = 18\,sccm$**.** Taking this into account, in combination with the fact that adjustments to the sparger plate are represented, the expansion with a transition zone and sparger plate is qualified as a valuable improvement of the original coupled model. Therefore, in the rest of the research, this will be utilized.

2.4.3 Limitations

The applied experimental correlations in the replicated model are validated for various ranges in both papers by Catalan and Razaei (2020, 2022) or earlier work they referred to, e.g. (Hibiki et al., 2000). Behaviour beyond these ranges results in major error margins or is simply unknown, therefore, the applicability of the model is limited to the same experimental validations ranges that come forward from the experimental correlations.

The estimation for the equilibrium constant of methane pyrolysis for various temperature and pressure conditions has a very high accuracy with an error margin maximum of 0.41%. This limited error margin only applies to the 900 – 1200 ˚C temperature range. Considering this range, the operating temperature should stick to the same limitation. This however does not include any physical limitations from a reactor material which could limit the operating temperature further.

Previously research set a fixed gas holdup at the bottom of the reactor and let it differ with the pressure and volume of gas flow. A fixed holdup could be an accurate approach for a single design. However, as the dimensions and parameters of the system have a broad range, in this research a superficial gas velocity-dependent correlation is applied. The correlation is based on molten metal experiments and correlation applies in a $0-32\%$ gas holdup range and 10^{-2} and 2 for the dimensionless superficial gas velocity, where it has a maximum error margin of ±30%. As the behaviour beyond these boundaries is unknown, utilization of this model should be kept to the same boundaries. Both gas holdup and indirectly also the superficial gas velocity are therefore limited. A result exceeding one of the two ranges is determined to be unusable. Since the correlation has been determined in molten metal, the applicability in molten salt was a question mark in this research. The results showed unexpectedly high and

therefore non-continuous figures in comparison to the metal phase. Hence this correlation is not applied for gas holdup in molten salt.

The Sauter diameter is important for the limiting mechanism of reactions. With large bubbles, the mass transfer could become a limit, leading to an additional efficiency reduction factor. This has not been included in the model therefore the maximum allowed bubble size is 9.6 mm as the system has been confirmed to be reaction limited below this threshold diameter. The dimensionless numbers that determine the mean bubble diameter should stay within the following ranges: N_{bo} = 7.98 e^{2} – 4.85 e^{4}, N_{ga} = 6.25 e^{6} – 1.79 e^{10} and N_{Fr} = 8 e^{-4} – 1.35 e^{-1}. Especially the Froude number at the top of the reactor has been a limiting factor (Catalan and Razaei). The mean bubble diameter is assumed to increase over the length of the transition zone due to the large increase in volume as a result of the conversion, but also the coalescence of the abundant number of bubbles from the sparger plate. Even though this correlation will not be perfectly linear, the linear modification is assumed to be a more accurate description than the previous correlation that assumed a balance situation over the entire height of the reactor. The linear increase from the bottom bubble diameter to the top of the transition zone does include the increase of the mean bubble diameter whereas the balance mean diameter does not include this behaviour over the first part of the reactor.

Reactor fill

Regarding the molten metal fill of the reactor two metals are included in the model. NiBi and CuBi are added with their respective catalytic parameters. If a different metal fill would be preferred, it could be added to the model when their catalytic parameters are known in the same units. Two salts have been considered in the research, e.g., NaCl and NaBr. The conclusions regarding molten salt are therefore based on these two, however, they are assumed to apply to comparable salts. The molten salt layer covers 25% of the liquid height, however, when a reactor becomes very small, the height of the salt layer could become insufficient to effectively separate the molten metal from the carbon molecules. This has been neglected. When assessing the weight of the molten salt layer, the gas holdup is important as salt is replaced by lighter gas. The difference is expected to be limited, but as the gas holdup at 75% of the liquid height is assumed to apply in the salt layer, the difference between the assumed and the real percentage has a minor influence on the weight.

3. Design of offshore installation

Offshore methane pyrolysis in the Dutch North Sea offers a range of opportunities. Converting natural gas production platforms into hydrogen production facilities would make the current offshore pipeline infrastructure available for hydrogen transport. Furthermore, the hydrogen flow would accelerate hydrogen implementation in neighbouring area close to the onshore connection of the pipeline.

The research will use the natural gas platform from Dutch gas company ONE-Dyas at the N05-A field as case study. The natural gas field, located 20 km offshore from Dutch island Schiermonnikoog and has been set-up to be connected to the NGT-pipeline for transport of the natural gas to shore. The location and top view of the platform design can be found in Figure 3.1.

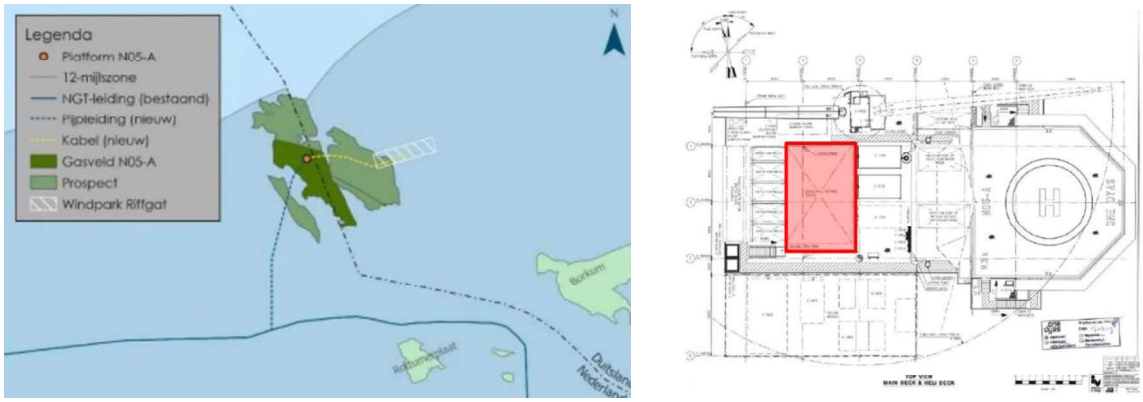

Figure 3.1: *N05-A platform from ONE-Dyas: (a) location with relevant gas field and prospects. The blue lines indicate the pipeline transport to shore, (b) top view with designated deck space for methane pyrolysis in red.*

The highlighted area in red is the designated space for methane pyrolysis and the related installations, which covers an area of 15 m x 10 m. Due to the crane's operational range on the platform, the height is limited. The available height is taken to be equal to the height of two shipping containers and therefore, set to 5.20 m. Due to the platform design, the 150 m^2 is prone to a weight limitation of 3.5 $mt.m^{-2}$.

The state-of-the-art platform is designed to reduce operational emissions significantly. Hence, a connection with the nearby German offshore wind farm Riffgat for electricity is established. In case of an electricity shortage the onshore connection to the German grid will provide the necessary electricity. The available electricity is also taken as a basis for the design for the offshore methane pyrolysis facility therefore the reactor will be heated with electricity.

The production plateau is limited to 6 million Nm^3 per day of natural gas and is satisfied by the N05-A field and neighbouring prospects. The flow will be kept at the limit for 2 years. Afterwards the flow will gradually decrease over time as the fields are depleted. Considering the model can cope with methane, nitrogen and hydrogen as inflow molecules, the gas composition is generalized to an easier composition. All hydrocarbons are assumed to be CH_4, as they also decompose into hydrogen and solid carbon. The rest has been assumed to present

1.3 mol% CO_2 is lumped into the inert N_2. Since this CO_2 percentage is limited, the assumption is made that no dry reforming will occur in the reactor. Overall, the gas composition in the model is described by 74.3 mol% CH_4 and 25.7 mol% N_2. The measured gas composition from gas samples of the field can be found in Appendix A3.

The deliverables consist of a flow scheme, reactor design and an assessment on the necessary auxiliary equipment for a complete overview of the offshore design. The flow scheme will foster understanding on the order of equipment and different flows on the platform, especially with an additional carbon outflow. The specifications at each step are pressure, gas composition, temperature and flow. The design considerations are explained in Section 3.2, ending with a model that can estimate design dimensions. Afterward, the model is applied to the specification of the flow designs adjacent to the flow scheme, which results in the most optimal design and required deck space for methane pyrolysis on itself. The auxiliary equipment necessary to connect the reactor to the current gas processing equipment and to make the hydrogen flow suitable for transport is last listed. The size of these installations will determine the spatial distributions and translates into a necessary deck space to process the entire natural gas flow. In case, the necessary deck space for all installations, including the installation for methane pyrolysis, exceeds the 150 m^2 currently available. The deck space should be extended to make offshore methane pyrolysis possible. Depending on the scale of the additional deck space, this could be an additional deck or an entire platform.

3.1 Flow scheme

The flow scheme on the platform includes both the installations currently applied on platforms for processing of gas flow from the well and also the new installations related to methane pyrolysis and processing of the hydrogen mixture. The different steps are indicated in blue and the installations in grey. The various reactants and products are shown in red. The entire flow is described below and afterwards visualized in the Figure 3.2.

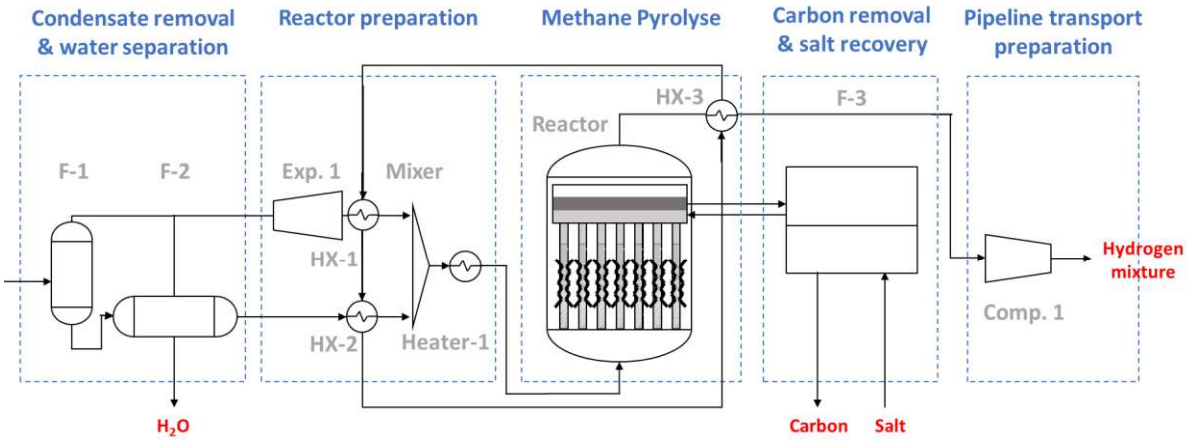

Figure 3.2: *flow scheme of the offshore methane pyrolysis facility*

Step 1: As the gas is a mixture at high pressure and temperature a part of the flow becomes condensate and water. This is separated and collected in the first step of the process. The water flow is filtered up the current standards and offloaded into the sea.

Step 2: When the flows are separated into water, condensate and natural gas, the natural gas is decompressed to reduce the pressure down to the operational pressure of the reactor. Normally the condensate flow is added to the natural gas in the final step and transferred along as a liquid to shore. However, the reactor can also convert the higher hydrocarbons in the condensate into hydrogen and solid carbon, natural gas and condensate are mixed before entering the reactor. Optionally the nitrogen can be rejected from the hydrocarbon stream, this would decrease the volume flow. As a result, the following equipment could be smaller. In the process it is important to heat the flow to already reach temperatures closer to the operational temperature of the reactor.

Step 3: Since the flow is ready for decomposition in the reactor, it is injected into the molten metal layer. In the process a hydrogen mixture is produced, containing hydrogen but also the remaining flow of unconverted methane and inert gas from the original flow. The percentage inert gas will differ depending on the application and application of nitrogen rejection. To prevent damage on subsequent installations, the hydrogen mixture is cooled. The heat losses in the process can be lowered by exchanging the heat with the inflow for the reactor preparation.

Step 4: The second flow produced by the reactor is the solid outflow containing mostly carbon and possible a small amount of salt which is still stuck due to adhesion. This high temperature solid outflow is again reduced and possible exchanged in the carbon handing process. The

carbon purity is increased by filtering the flow, and the remaining salt is brought back into the reactor. The salt volume in the reactor is still expected to very slowly decrease therefore a periodic inflow of salt could be necessary. The carbon outflow is shipped to shore. During maintenance, these ship can also deliver new salt to replete the molten salt level.

Step 5: At last, the hydrogen mixture containing hydrogen, unconverted methane and a remaining part of inert gas is pressurized and cooled to meet the operational conditions of the pipeline to shore. Depending on the pipeline purpose, an additional hydrogen purification step is necessary. This would result in high purity hydrogen, meeting the pipeline requirements and the waste flow would be brought back to the begin of step 2.

3.1.1 Specifications

The specifications of a flow scheme refer to the design and operational parameters that define how the system should function. In the context of the current scheme, the specification of the flow scheme will depend on the properties of the incoming gas, the requirements of the pipeline that transports the produced hydrogen to shore, and the requirements for shipping the carbon by-product.

In order to meet the desired gas composition requirements, a certain methane conversion is expected to be produced by the (multiple) reactor units in the flow scheme. The necessary conversion of methane can be calculated using the following formula, which assumes that the inflow consists only of methane and nitrogen:

$$y_{H_2} = \frac{2\,X_{CH_4}}{\varepsilon_{CH_4}(1 - X_{CH_4}) + \varepsilon_{CH_4} 2\,X_{CH_4} + \varepsilon_{N_2}} \tag{3.1}$$

$$y_{CH_4} = \frac{\varepsilon_{CH_4}(1 - X_{CH_4})}{\varepsilon_{CH_4}(1 - X_{CH_4}) + \varepsilon_{CH_4} 2\,X_{CH_4} + \varepsilon_{N_2}} \tag{3.2}$$

$$y_{N_2} = \frac{\varepsilon_{N_2}}{\varepsilon_{CH_4}(1 - X_{CH_4}) + \varepsilon_{CH_4} 2\,X_{CH_4} + \varepsilon_{N_2}} \tag{3.3}$$

Where y (mol%) depicts the mole fraction in the outflow of the representative molecule, X_{CH_4} is the methane conversion in the reactor in decimal fraction, ε (mol%) indicates the mole fraction of the representative molecule in the inflow.

Methane pyrolysis on the platform should be able to produce at least a gas mixture with a similar mole fraction in the outflow as SMR. This means y_{H_2} should be at least 75.4 mol% (Rostrup-Nielsen, 1993). The gas composition from the 6 million Nm^3 per day gas flow from the processing facility is assumed to have $\varepsilon_{CH_4} = 74.7\ mol\%$ and $\varepsilon_{N_2} = 25.3\ mol\%$, the fore, the X_{CH_4} should be at least 81.0%. When installing a pressure swing adsorption unit before the reactor units to reject N_2 from the gas mixture. The minimum conversion ratio decreases as the gas flow becomes smaller. Assuming a N_2 recovery rate of 90% (Oni et al., 2022), the gas inflow is modified to $\varepsilon_{CH_4} = 96.7\ mol\%$ and $\varepsilon_{N_2} = 3.3\ mol\%$. This corresponds to $X_{CH_4} > 62.6$ % to equal or exceed the 75.4 mol% from SMR.

The carbon separation and handling, should assure a continuous process is maintained. According to previous research, losing more than 0.001 wt% of their $MgCl_2$ salt layer in the carbon would not be economically feasible (Kang et al., 2019). In this case with NaCl, the installation design has been set to the same threshold. Solid carbon and salt have a comparable density, the composition of the carbon outflow is therefore assumed to be: 99.999 mol% C_s and 0.001 %. The ships responsible for transporting the carbon to shore are assumed to handle the solid at a temperature of 55 °C or below, which is the maximum for coal cargo shipping (Ostrowicki, 2021).

The requirements of the NGT-pipeline, responsible for transport of the produced hydrogen mixture to shore, depends on the neighbouring activities. In the first scenario, surrounding activity is low. The hydrogen flow from the N05-A platform would be the most significant inflow. In this scenario the gas composition requirements are set to meet the SMR standard. In the second scenario, surrounding activity is high. For example due to hydrogen production from scheduled Dutch offshore wind farm. In this scenario the produced hydrogen from the platform should meet the hydrogen backbone requirements, to prevent significantly decreasing the hydrogen quality in the pipeline. This is minimum 98 mol% hydrogen and maximum 0.1% hydrocarbons. Gas provided to the NGT-pipeline should always be around 30 ˚C and a pressure of 80 bar.

Due to the setup of installations, and requirements, four flow designs have been considered with the current flow scheme. The design considerations and specifications of these flow designs will be described in this paragraph. The flow designs are:

Table 3.1: *Overview of flow designs*

Flow design	description
1	As depicted in Figure 3.2**Error! Reference source not found.**, without nitrogen rejection
2	90% of nitrogen is rejected from the flow, before entering the reactor.
2+	As per Flow design-2 with a conversion of 90%.
3	As per Flow design-2+ with a hydrogen purification step at the end.

Flow Design-1, flow design as depicted in Figure 3.2, therefore, direct conversion of the gas flow without nitrogen rejection. In this flow design the surrounding activities are assumed to be minor. Therefore, the flow will meet the hydrogen outflow of a SMR installation.

Table 3.2: *Specification for Flow Design-1. This includes no nitrogen rejection or offshore hydrogen purification. The surrounding activity is low; therefore, the produced hydrogen mixture can just meet the SMR standard.*

Step	Temperature [˚C]	Pressure [bar]	Composition [mol% CH_4:N_2:H_2] *[mol% C_s:NaCl]*	Flow [million Nm^3] *[mt]*
Gas processing	37	96	74.7 : 25.3 : 0	6.0
Decompression	37	10-30	74.7 : 25.3 : 0	6.0
Heating	900-1050	10-30	74.7 : 25.3 : 0	6.0
Methane pyrolysis [a]	900-1050	10-30	8.8 : 15.8 : 75.4	9.6
Carbon separation & handling	*55*	-	*99.999 : 0.001*	*1950*
Pipeline preparation	30	80	8.8 : 15.8 : 75.4	9.6

[a] The methane pyrolysis installation reaches a methane conversion of 81.0% to meet a similar hydrogen composition (75.4 mol%) in the outflow as SMR.

Flow Design-2, in this design the nitrogen is rejected from the flow, before entering the reactor. With a N_2 recovery rate of 90%, a large part of the nitrogen can be vented to the atmosphere. The reduced flow leads to a size reduction of installations downstream, Hence, the flow design could eventually come out on top of Flow Design-1. Also surrounding activities are also assumed to be low, the necessary conversion ratio goes down to produce gas with the same hydrogen mol% in the outflow as SMR in comparison to Flow Design-1.

Table 3.3: *Specification for Flow Design-2. This includes nitrogen rejection but no offshore hydrogen purification. The surrounding activity is low, therefore, the produced hydrogen mixture can just meet the SMR standard.*

Step	Temperature [˚C]	Pressure [bar]	Composition [mol% CH_4:N_2:H_2] *[mol% C_s:NaCl]*	Flow [million Nm^3] *[mt]*
Gas processing	37	96	74.7 : 25.3 : 0	6.0
Decompression	37	10-30	74.7 : 25.3 : 0	6.0
Nitrogen rejection	37	10-30	96.7 : 3.3 : 0	4.6
Heating	900-1050	10-30	96.7 : 3.3 : 0	4.6
Methane pyrolysis [a]	900-1050	10-30	22.5 : 2.1 : 75.4	7.4
Carbon separation & handling	*55*	-	*99.999 : 0.001*	*1500*
Pipeline preparation	30	80	22.5 : 2.1 : 75.4	7.4

[a] The methane pyrolysis installation reaches a methane conversion of 62.5% to meet a similar hydrogen composition (75.4 mol%) in the outflow as SMR.

Flow Design-2+, an installation only converting 62.5% of the methane conversion seems rather small. The same design is therefore also tested for a conversion of 90%. To see what would happen to the necessary deck space and in the end the economics.

Table 3.4: *Specification for Flow Design-2+. This is comparable to Flow Design-2, this includes nitrogen rejection but no offshore hydrogen purification, however the methane pyrolysis conversion ratio will be 90% instead of 62.5%.*

Step	Temperature [˚C]	Pressure [bar]	Composition [mol% CH_4:N_2:H_2] *[mol% C_s:NaCl]*	Flow [million Nm^3] *[mt]*
Gas processing	37	96	74.7 : 25.3 : 0	6.0
Decompression	37	10-30	74.7 : 25.3 : 0	6.0
Nitrogen rejection	37	10-30	96.7 : 3.3 : 0	4.6
Heating	900-1050	10-30	96.7 : 3.3 : 0	4.6
Methane pyrolysis [a]	900-1050	10-30	5.2 : 1.7 : 93.1	8.6
Carbon separation & handling	*55*	-	*99.999 : 0.001*	*2160*
Pipeline preparation	30	80	5.2 : 1.7 : 93.1	8.6

[a] The methane pyrolysis installation reaches a methane conversion of 90.0%.

Flow Design-3, in the last flow design, the platform is prepared on a situation with hydrogen production nearby N05-A, therefore a high purity hydrogen flow is demanded. To reach this a PSA unit is necessary for purification as methane pyrolysis will not be able to produce the set hydrogen backbone requirements (98%mol% H_2 with < 0.1 mol% of hydrocarbons) (Pijkeren, 2020). The waste stream from the PSA unit, could be recycled in the flow scheme. It could be re-injected in the system after the decompression step. This would increase all other installations as the system would include more flow. Optionally this flow could be transferred with a dedicated pipeline, as mixing with the NGT-pipeline would decrease the hydrogen carbon mol% below the threshold.

Table 3.5: *Specification for Flow Design-3, this includes both with nitrogen rejection and offshore purification. The design is comparable to Flow Design-2+ however a hydrogen purificaton step is added to produce high purity hydrogen as the surrounding activity is high.*

Step	Temperature [˚C]	Pressure [bar]	Composition [mol% CH_4:N_2:H_2] *[mol% C_s:NaCl]*	Flow [million Nm^3] *[mt]*
Gas processing	37	96	74.7 : 25.3 : 0	6.0
Decompression	37	10-30	74.7 : 25.3 : 0	6.0
Nitrogen rejection	37	10-30	96.7 : 3.3 : 0	4.6
Heating	900-1050	10-30	96.7 : 3.2 : 0	4.6
Methane pyrolysis [a]	900-1050	10-30	5.2 : 1.7 : 93.1	8.6
Carbon separation & handling	*55*	-	*99.999 : 0.001*	*2160*
Cooling	30	10-30	5.2 : 1.7 : 93.1	8.6
Purification [b]	30	10-30	0.01 : 1.9 : 99.8	7.2
Recycle stream	30	10-30	35.0 : 0.7 : 64.3	1.4
Compression	30	80	0.01 : 1.9 : 99.8	7.2

[a] The methane pyrolysis installation reaches a methane conversion of 90.0%.

[b] The PSA unit separates the hydrogen from the gas mixture with a 90% recovery rate (Oni et al., 2022).

3.2 Reactor design

Conventional industrial installations are often large and heavy. However, with the limitations from the offshore platform a compact but relative light reactor is needed.

The design is based on a shell and tube concept where a shell creates a close environment. In the closed environment, heat transfer within the shell is not accounted as lost since the heat will still contribute to the system. The shell can be filled with multiple columns of molten metal and salt which has multiple benefits: (i) Due to the reduced volume per column the wall thickness can be reduced which eases heating, (ii) the weight is more easily distributed in comparison to one big reactor, enabling a larger volume of melt on the platform and (iii) the installation can be run on a reduced number of columns, offering a larger window for maintenance as operation are only reduced but not paused. For methane pyrolysis the top of the shell and tube concept was be modified to make carbon removal at the top possible. Therefore, the reactors are interconnected at the top to enable passive removal with an overflow. Since the "shell and tube" concept also exist for other industrial equipment to prevent confusion in the rest of the research, the shell and tube concept is called "reactor unit" to indicate it concerns the reactor. The dimensions of a single reactor unit are limited to 5 m width, 4 m depth and 5.2 m height. The natural gas flow is divided over multiple reactor units. This is more convenient for production and transport purposes but also creates redundancy, so the installation stays operational when an element of one reactor unit breaks down without violating the security limits. Also maintenance can be executed on the reactor unit struck by a problem or failure.

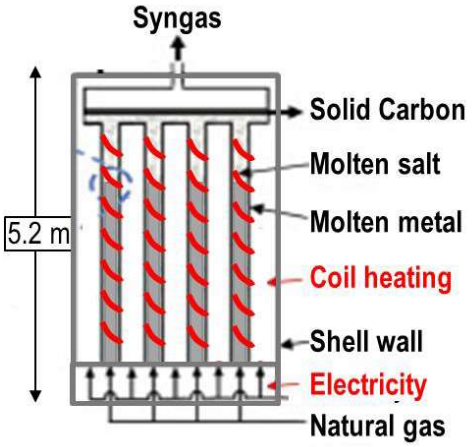

Figure 3.3: *Reactor design based on concept from (Catalan & Rezaei, 2022)*

The shell will be covered with a thick thermal cover as heat losses from the shell will reduce the system efficiency. The insulation design is based on a program from the North American Insulation Manufacturers Association (Murphy, 2018). The main component will be the ceramic fibre insulation in between a silica cloth on the cold side and a cover of Inconel wire on the hot side, moreover the thread will be from quartz or Nextel. The total thickness is assumed to be 0.1 m and density is assumed to be mostly determined by the ceramic fibre insulation therefore the entire pack is assumed to be weight 0.25 mt / m^3 (Asian insulations, 2017). This does reduce the surface of a reactor unit to 4.8 m x 3.8 m.

Various properties should be defined for a reactor unit to utilize the methane pyrolysis model from Chapter 2. The properties are: natural gas flow per column, temperature, pressure, column diameter and column height. The natural gas flow per columns depends on number columns, therefore the latter is also an important property. In this section the number of columns and column height of a single reactor unit are related to the starting properties temperature, pressure and column diameter. In the next section, these properties are used as

in the final model from Chapter 2 to determine how much methane is converted in hydrogen and carbon within the model limitations.

In order to determine the appropriate number of columns and height under varying starting conditions, it is important to ensure that these variables are balanced in order to avoid exceeding the weight limit of the platform. As excessive height with a high number of columns may result in a weight exceeding the allowable limit, it is necessary to consider this constraint as depicted in Equation 3.4. Not only the weight of the columns but also, the weight of constant components of the reactor unit, such as the carbon black removal system, the natural gas inlet, and the hydrogen outlet should be taken into account.

$$W_{max} > W_i + W_d \times H_c \times N_{m2} \tag{3.4}$$

Where, the maximum weight is W_{max} = 3.5 mt.m^{-2}, Wi (mt.m^{-2}) describes the weight independent of the number of columns, W_d (mt.m^{-1}) the weight which depend on the height of the columns, H_c the column height (m) and N_{m2} the columns configuration (m^{-2}). The columns will be evenly distributed over the reactor unit, therefore, an increase in columns would increase the N_{m2}. All parameters will be discussed in the next chapter.

3.2.1 Weight independent of the number of columns

The bottom and top compartments are spread across the entire surface area of the reactor unit. Therefore, they are independent on the number of columns and their configuration. The independent weight of the reactor unit has been separated in top compartment, bottom compartment, insulation and additional weight. The vertical walls of the shell are not taken into account. This has been assumed to be acceptable as the weight of the columns is overestimated in this region by N_{m2} due to spacing near the walls.

Bottom compartment

The bottom compartment has a height of 0.1 m and ensures that the gas flow is evenly distributed over the installed columns by the present piping and instrumentation. For the compartment specifically the floor and roof are taken into account. They match the thickness of the column walls to simplify manufacturing of the reactor unit.

Top compartment

The top compartment is slightly larger compared to the bottom compartment due the constant present of the salt layer that connects all columns and the solid carbon top layer. The clearance between the roof and floor is 0.15 m. The salt layer is assumed to be 0.03 m and the solid carbon layer 0.05 m. A thicker layer should lead to less salt contamination at the top. For the top compartment the roof and floor plate are taken into account, in combination with the salt and solid carbon. Since the salt layer in the compartment and the columns is in direct contact, there is no sheet material but salt on these places. This has been included in the model.

Insulation

The ceramic fibre insulation cover outside the reactor unit shell is also subtracted from the maximum weight load before determining the column configuration. As the layer is 0.1 m thick on all sides and therefore the distributed weight equals 0.050 mt / m^2.

Extra

Additional equipment like the piping and instrumentation in the bottom, the coil heating elements and overflow in the top are all incorporated by assuming they have a combined weight of 0.1 mt / m^2.

3.2.2 Weight dependent on number of columns

The column weight depends on the wall thickness and reactor fill consisting of molten metal and molten salt. Even though the contribution to the conversion rate is neglected by excluding the salt layer from the methane pyrolysis model, the layer is still present in the design to separate the molten metal from the solid carbon.

Reactor fill

With a varying column configuration the total volume of the reactor fill changes and therefore the related weight. The current two alloys included in the model for the reactor fill are $Cu_{0.45}Bi_{0.55}$ and $Ni_{0.27}Bi_{0.73}$. Both alloys are a combination of a metal with high catalytic activity and an inert metal without substantial catalytic effect, as the catalytic activity does not significantly diminish in an alloy with an inert metal this creates a molten metal catalyst that operates at a low temperature. The inert metal also reduces the price as the catalytic metal is most of the time more expensive. To select the best alloy to fill the first 75% of the reactor the catalytic behaviour and the price are compared. Since $Cu_{0.45}Bi_{0.55}$ is the cheapest, Cu is around 3 times cheaper than Ni (*Daily metal prices*, 2023), and also a slightly more active alloy, it is selected as molten metal in the analysis. The salt selection is less critical as both NaBr and NaCl are assumed to perform in preventing metal contamination of the solid carbon product and can be filtered in the same manner. NaCl is a more common salt and cheaper, see Appendix A2, therefore, the top 25% is filled with NaCl.

The total volume of metal and salt in the reactor is determined by a combination of factors, including the diameter and number of columns, as well as the gas holdup percentage in the reactor. With a higher gas holdup, the necessary fill would decrease to fill the same reactor column, therefore, a higher gas holdup percentage results in lighter columns, which allows for an increase in the number of columns in a single reactor unit. Initially the weight of a column is largely overestimated as they are completely filled. This has been corrected by doing the analysis again with the gas holdup from the a run of the methane pyrolysis model with the filled columns. The lowest gas holdup percentage, found at the bottom of the column, is used as a baseline to prevent underestimation of the weight of a column. This process is then applied in subsequent iterations, resulting in an increase in the number of columns. After repeating this process several times, the number of columns tends to converge to a single value or oscillate between two values. In this case, the lower value is chosen to ensure that the weight of the columns is not underestimated.

Wall thickness

The thickness of the column walls and shell of the reactor unit will determine the weight of the reactor. However, the thickness is not a constant factor but is defined by the operating pressure and strength of the material. In this research the HP-40 grade Centralloy G4852 R alloy from Schmidt+Clemens Group is utilized (2013). The high percentage of Cr and Ni in

the alloy make it resistant against the high operating temperature. The material is applied in methane reforming installations which are exposed to temperatures up to 1050 ˚C (Schmidt + Clemens Group, 2013).

The initial strength of the material however reduces over project lifetime due to difficult operating conditions. The behaviour depends on the Larson Miller parameter, LMP, which generalizes the impact of operating time and temperature. For the specific material utilized in this research the LMP looks as follows:

$$\mathrm{LMP} = \frac{\mathrm{T}(22.9 + \log \mathrm{tr})}{1000} \tag{3.25}$$

Where T represents the temperature in Kelvin and tr the operational lifetime at this temperature. The constant 22.9 in the equation depends on the selected material and would for instance decrease if a low alloy steel was applied. The operational lifetime is set to 200,000 h. This covers the 20-year operational lifetime and eventually a short extension of the project, preventing difficult and expensive offshore replacement operations of the reactor units.

The correlation between material strength and LMP of the Centralloy G 4852 Micro R alloy can be seen in Figure 3.4. The combination of project lifetime and high temperature (1050 °C) could exceed the current range for which the material strength-LMP correlation has been determined. Since the correlation is very consistent, therefore, it is assumed that the use of the formula can be extrapolatable beyond the maximum LMP of 36.8 in the material data sheet, to determine the material strength for 1050 °C.

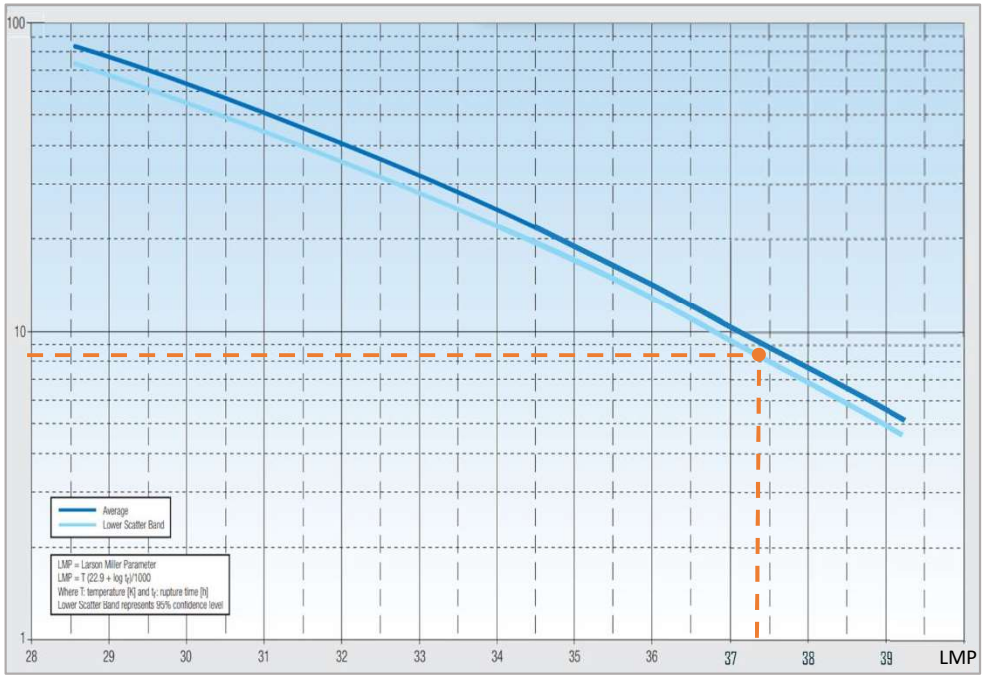

Figure 3.4: *Strength (MPa) on the vertical axis determination for wall material Centraloy G4852 Micro R depending on Larson Miller parameter (LMP) on the horizontal axis at 1050 ˚C (Schmidt + Clemens Group, 2013)*

It has been determined that among the three potential failure directions considered, circumferential failure is the most dominant (Engineering Toolbox, 2005). When the reactor pressure increases to a point where the internal hoop stress exceeds the tensile strength of the

reactor wall, a rupture will occur in the column. In the current scenario, internal pressure is the primary factor that will cause failure. However, with the right wall thickness of the column, this can be prevented. The circumferential stress (σ_c) in the column can be determined by utilizing the varying diameter and pressure, together with the wall strength, that depends on temperature, the necessary wall thickness for various operational conditions is obtained.

$$\sigma_c = \frac{\left(P_i r_i^2 - P_o r_o^2\right)}{r_o^2 - r_i^2} - \frac{r_i^2 r_o^2 (P_o - P_i)}{r^2\left(r_o^2 - r_i^2\right)} \tag{3.26}$$

Where the internal pressure, P_i, differs per design and equals the set pressure inside a column. Po is outside pressure and assumed to equal atmospheric pressure. Three different radii have been stated, the inner radius r_i equals to half of the varying inner diameter. Therefore the wall thickness (t_w) should be added to the other two resulting in $r = r_i + ½*t_w$ and $r_o = r_i + t_w$

Safety factors

The structural integrity of the reactor units is ensured by introducing safety factors, both on the load (driven by the pressure) and the strength of the installation (material strength of Centralloy G4852 R). The safety factors reduce the chance the installation fails, provide additional operational safety and accounts for unforeseeable risks. The strength, divided by the material safety factor should be larger than the stress multiplied by the load safety factor.

The Centralloy G4852 R has been quantified as a reliable material, for the pressure the range is not too extreme in comparison to other installation and is constant. At last, the environmental impact is low due to the protection by the insulation layer. Overall the material falls into the lowest division and is therefore reduced with a safety factor of 1.5 (Bauto, 2022).

A similar safety factor on the failure pressure for the pressurized reactor was harder to find therefore hydrogen pressure vessels have been taken as reference case. The insulated pressure vessel was both at high pressure and at cryogenic temperature (extremely low temperatures) and therefore seems to be at a comparable situation from the perspective of safety. Hence the applied safety factor of 2.25 on the burst pressure has been taken into account (Ross et al., 2021).

$$\frac{\sigma_{strength}}{1.5} > 2.25\ \sigma_{load} \tag{3.7}$$

The material strength and load of the pressure are represented in Equation 3.4 including the safety factors and the hoop stress from the previous paragraph. Solving these equations in python leads to the minimum wall thickness to withstand the set pressure. Despite for the lower range input values, such as a low temperature and pressure, the wall needs to rigid enough to withstand its own weight and can take incidental outside loads. Generally for a vessel diameter up to 1 m the wall thickness, therefore, needs to be at least 5 mm (Towler & Sinnott, 2008). This also accounts for a corrosion allowance of 2 mm. The function will therefore determine the minimum wall thickness to withstand the pressure over the entire lifetime of the project and be sufficiently rigid.

3.2.3 Column configuration and height

Two column configurations that have been considered in the analysis are: (i) maximum number of columns and (ii) maximum height of columns. The first configuration maximizes the total area of the columns reducing the flow per reactor, this benefits the conversion rate as the smaller flow results in a higher conversion rate. The second configuration maximizes the height of the reactor and therefore the residence time, this also fosters the conversion rate. Both configurations utilize the entire weight load that is maximum allowed. The radius of a column consist not only of the internal diameter but also the wall thickness and the heating coil wrapped around the wall. Therefore, $r = \frac{D_i + 2t_{wall} + 2t_{coil}}{2}$.

Maximum number of columns

For optimalization of the number of columns a triangular pattern is applied. This creates a close configurated pattern which can fit a larger number of columns than simple staking of rows with columns. The pattern can be seen in Figure 3.5.

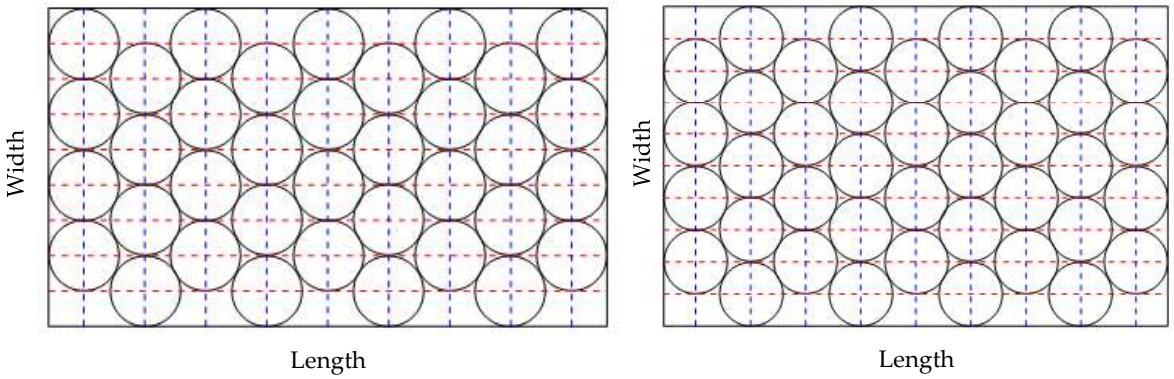

Figure 3.5: *Column distribution in limited reactor unit area to fit most columns as possible*

The configuration consists of rows with a $2 \times r$ (shown in red) and columns with a $2\sqrt{3} \times r$ (shown in blue) centre-to-centre distance. The number N of columns on width and length can therefore be described as followed (Engineering ToolBox, 2014):

$$N_{width} = \frac{(Width/r) - 1}{2} \tag{3.8}$$

$$N_{length} = 1 + \frac{(Length/r) - 2}{\sqrt{3}} \tag{3.9}$$

However, in case the number of columns on the width equals $\frac{(Width/r)}{2}$, the number can be alternated which is shown in Figure 3.5B. The orientation of the rows, either along the width or length side of the surface, determines the total number of columns, $N_{total\ columns}$. By considering both orientations, the maximum number of columns that can fit on the surface can be calculated. In other words, the maximum number of columns is determined by the orientation of the rows that results in the highest number of columns. This $N_{total\ columns}$ will be utilized to determine the flow per column in the next section.

When the columns are configured to fit the maximum of columns, N_{m2} equals $\frac{6}{(4r \times 3\sqrt{3}r)}$ based on the middle of the reactor unit. With equation 3.1, the adjacent reactor height, H_c can be

determined. This is utilized in the methane pyrolysis model in the next section to determine the performance of a reactor unit. Due to spacing near the shell of a reactor unit the weight in that region would be slightly overestimated. However, this is compensated by the fact that the weight of vertical walls for the shell is not accounted for.

Maximum height

The maximum height available for the columns is the remaining height after the height of the various components is subtracted from 5.2 m. The bottom and upper insulation layers each contribute for 0.10 m to the height, for a total of 0.20 m. The bottom compartment adds an additional 0.10 meters, and the top compartment adds 0.15 m. The thickness of the four reactor sheets on the outside of the compartments should also be taken into account in the calculation However, as the column goes through the bottom sheet of the top compartment, to transport the hydrogen and solid carbon, only three are subtracted from the remaining height. Overall, the maximum height of a column, $H_{c,max}$, can be expressed with $4.75 - 3t_{sheets}$.

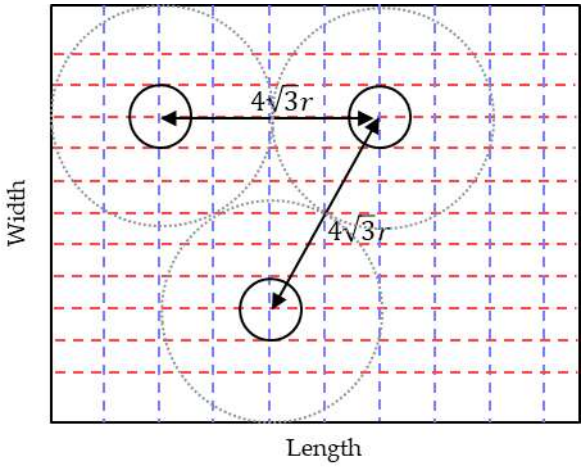

Figure 3.6: *Reduced column configuration for maximum height*

To prevent exceeding the maximum weight, the columns are given a perimeter with a total radius of $2\sqrt{3}r$. This reduces the N_{m2} by a factor 12. When it precisely equals $H_{c,max}$ equation 3.8 and 3.9 are utilized to determine $N_{total\ columns}$. However, the perimeter is taken into account by replacing r by $2\sqrt{3}r$. This only happens on rare occasions, therefore, the perimeter should be corrected with a correction factor to obtain the maximum number of columns with $H_{c,max}$. Therefore, $r = 2\sqrt{3}\left(\frac{D_i + 2t_{wall} + 2t_{coil}}{2}\right) \times \sqrt{\frac{H_{c,max}}{Hc}}$. This configuration would maximize the available weight together with $H_{c,max}$ in equation 3.4. The $N_{total\ columns}$ related to the corrected radius will be utilized in the next section.

3.3 Properties of reactor unit

The impact of various column configurations and temperature, pressure, and diameter on the number and height of columns is demonstrated in Tables 3.65 and 3.7, which present data generated under different conditions. These tables illustrate the effect of these factors on the number and height of columns.

Table 3.6: *The number of columns and column height at varying reactor unit conditions. The parameters are determined with a column configuration enabling the maximum number of columns, without exceeding the 3.5 mt.m^{-2}platform weight limit.*

Temperature [˚C]	Pressure [bar]	Diameter [m]	$N_{total\ columns}$ [-]	Hc [m]
900	5	0.1	1197	0.928
900	5	0.2	368	0.798
900	20	0.2	280	0.489
1000	5	0.2	351	0.737
1000	20	0.2	210	0.341

The data shows that an increasing temperature, pressure and diameter reduces the number of columns that fit in a reactor unit. Due to the closed configuration of the columns, to enable the maximum number of columns, the height is significantly reduced compared to the $H_{c,max} = 4.75 - 3t_{sheets}$. Also, a temperature increase from 900 to 1000 ˚C, has a smaller impact on the wall thickness than a pressure increase from 5 to 20 bar.

Table 3.7:*:number of columns and column height at varying reactor unit conditions. The parameters are determined with a column configuration enabling the maximum column height, without exceeding the 3.5 mt.m^{-2}platform weight limit.*

Temperature [˚C]	Pressure [bar]	Diameter [m]	$N_{total\ columns}$ [-]	Hc [a] [m]
900	5	0.1	319	4.735
900	5	0.2	90	4.735
900	20	0.2	36	4.680
1000	5	0.2	77	4.722
1000	20	0.2	16	4.618

[a] The column height will equal the $H_{c,max}$ at any condition in this column configuration

Again, also when maximizing the column height, the data shows that an increasing temperature, pressure and diameter reduces the number of columns that fit in a reactor unit. The wall thickness and therefore also the sheets depend on these parameters. At lower temperature, pressure and diameter the sheet thickness of the compartments equals the 5 mm minimum, even though for pressure failure it could be thinner. At more severe operating conditions, the thickness increases beyond the threshold, decreasing the column height further than 4.735 m. A visual example of a design can be seen in Appendix A4, this regards a design for maximum height.

3.3 Installation performance and deck space

By comparing the performance of both configurations in a range for column diameter, operating pressure and temperature a best performing offshore design is found within the necessary methane pyrolysis performance requirement. A couple of scenarios have been considered in the performance analysis. First, the performance of a single reactor unit was considered, both to see how much methane is converted and which column configuration works best. Second, the number of reactor units necessary for obtaining the required conversion rates was determined. This can be translated into deck space to evaluate the total deck space per flow design later in the chapter. This part of the analysis will only be executed for the best column configuration as the other will need more deck space and it therefore a worser option. All possible scenarios have been listed in Table 3.8:

Table 3.8: *All possible scenarios relevant to determine the performance of the methane pyrolysis installation.*

Scenario	Column configuration	Nitrogen rejection	Number of reactor units	Conversion rate [%]
6.1.X.MaxColumn	Max columns	No	1	***X***
6.1.X.MaxHeight	Max height	No	1	***X***
6.1.X.MaxColumn.NRA	Max columns	Yes	1	***X***
6.1.X.MaxHeight.NRA	Max height	Yes	1	***X***
6.X.81.MaxColumn	Max columns	No	***X***	81.0
6.X.81.MaxHeight	Max Height	No	***X***	81.0
6.X.62.5MaxColumn.NRA	Max columns	Yes	***X***	62.5
6.X.62.5MaxHeight.NRA	Max height	Yes	***X***	62.5
6.X.90.MaxColumn.NRA	Max columns	Yes	***X***	90.0
6.X.90.MaxHeight.NRA	Max height	Yes	***X***	90.0

The ***X*** indicates what parameter is unknown and should be identified in the analysis

To reduce execution time and the number of conditions tested, a logical range is applied to starting parameters. The temperature range is set to 900-1050 °C in intervals of 50 °C, as 900 defines the low limit of the equilibrium constant and 1050 the high of the reactor material. Since the N_{fr} decreases with a higher diameter, a high diameter would be preferred, however the N_{bo} and N_{ga} limit the diameter to 0.46 with the CuBi fill. Therefore, the diameter range is set to 0.20-0.46 m in intervals of 0.01 m. At last, the pressure range is increased from 5-50 bar by steps of 5 bar. The maximum pressure is reduced when the necessary conversion rate is above the maximum conversion obtainable at the pressure. When a possible interesting condition between the 5 bar intervals is spotted, the designs are also investigated between the initial pressure intervals. The performance of both single and multiple reactor units will be discussed separately.

3.3.1 Single reactor unit performance

The performance of a single reactor unit can be determined by execution of the model for column configuration considering ranges of temperature, pressure, and column diameter and subsequently filling the resulting properties in the methane pyrolysis model. Four different scenarios have been analysed since two modifications can be made. First the configuration of the columns can be set to be as close as possible, maximizing the number of columns or they are be designed to utilize the maximum possible height. Second, the performance can be determined when the reactor unit operates with the standard 6 Nm^3 natural gas but also with the reduced flow coming out of the nitrogen rejector. This flow is smaller and has a much higher methane mol% since 90% of nitrogen is rejected. The results with the highest conversion rate are shown in Table 3.9.

Table 3.9: *Performance of single reactor unit with varying column configuration and inflow*

Configuration	NRA	N_{units} [-]	T [°C]	P [bar]	D [m]	N [-]	Hc [m]	X_{CH4} [%]	t_{wall} [m]
Max columns	No	1	1050	5	0.45	65	0.74	73.9	0.035
Max height	No	1	1050	5	0.39	15	4.66	44.0	0.030
Max columns	Yes	1	1050	5	0.45	65	0.71	77.9	0.035
Max height	Yes	1	1050	5	0.39	15	4.66	49.7	0.030

Configuration	NRA	N_{units} [-]	T [°C]	P [bar]	D [m]	N_{fr} [-]	Jg+ [-]	$\alpha_{average}$ [%]	α_{top} [%]
Max columns	No	1	1050	5	0.45	5.014	72.7	75.3	76.5
Max height	No	1	1050	5	0.39	29.693	400.9	81.9	82.1
Max columns	Yes	1	1050	5	0.45	4.368	63.3	73.1	74.8
Max height	Yes	1	1050	5	0.39	25.739	347.5	81.5	81.8

Not surprisingly the highest methane conversion is reached at the maximum operating temperature 1050 °C and at lowest pressure. These conditions have repeatedly proven to improve methane conversion. Also, a large diameter was beneficial, however not he maximum diameter showed to be the most optimal. This is because a larger diameter results in less columns and probably also the increased wall thickness but this effect is smaller. Even though the conditions for Flow Design-2 are met, regarding 62.5% methane conversion, the current configuration of parameters does not result in an applicable scenario as the limiting parameters are exceeded, $N_{fr} < 0.135$, $Jg+ < 2$ and $\alpha_{top} < 32\%$.

A clear difference between the column configuration can be distinguished, maximizing the number of columns results in a much higher methane conversion than maximizing the height of the columns, furthermore the limiting parameters are much closer to their respective threshold. The columns configuration is therefore identified as the better design for reactor units. Moreover, nitrogen reduction has a positive influence on the methane conversion, due to the reduced flow and increased methane percentage the conversion increases with 3.1% for maximum column configuration and even 5.7% for maximum height configuration.

3.3.2 Multi reactor unit performance

Determining the minimum number of reactor units for a specific conversion, was more difficult. The same approach as for a single reactor unit was applied however with a varying number of reactor units until the necessary properties for a reactor unit design are found that meet the desired minimum conversion rate. Since the analysis for a single reactor unit showed that the column configuration for maximum columns performs better, both regarding conversion rate as model boundaries, only this approach is considered. The results in **Table 3.10**, show the design that can produce the minimum conversion rate with the lowest number of reactor units within he model boundaries.

Table 3.10: *Minimum number of reactor units to meet the required methane conversion of the flow designs (81.0% without NRA, 62.5% and 90.0% with NRA)*

Configuration	NRA	N_{units} [-]	T [°C]	P [bar]	D [m]	N [-]	Hc [m]	X_{CH4} [%]	t_{wall} [m]
Max columns	No	19	1000	12	0.44	54	0.25	81.1	0.056
Max columns	Yes	10	950	19	0.39	68	0.23	66.6	0.060
Max columns	Yes	33	1000	5	0.46	68	0.47	91.4	0.027

Configuration	NRA	N_{units} [-]	T [°C]	P [bar]	D [m]	N_{fr} [-]	J_g+ [-]	$\alpha_{average}$ [%]	α_{top} [%]
Max columns	No	19	1000	12	0.44	0.134	1.97	20.8	22.6
Max columns	Yes	10	950	19	0.39	0.134	1.80	20.8	22.5
Max columns	Yes	33	1000	5	0.46	0.129	1.89	16.2	17.8

The reactor designs had to be modified until all limiting parameters from the model, where below their respective threshold. Just as in Catalan and Razaei their research, the N_{fr} showed to be the most limiting boundary parameter. In contrast to the single reactor unit, manging the flow, and thereby the boundary parameters was important, therefore, the combination of highest temperature and lowest pressure was not necessarily the best approach as they do increase gas expansion and the wall thickness of the columns. Limiting space for columns and increasing the gas velocity inside them. As the N_{fr} is negatively correlated with the column diameter, the need for a larger diameters also showed just as with a single reactor unit. With an increasing number of reactor units, the impact of adding additional units decreases because each unit represents a smaller percentage of the total volume.

The reduced flow and lower conversion requirement made Flow Design-2 the least demanding design regarding deck space, followed by Flow Design-1 and Flow Design-3. A reactor unit had a deck space of 5 x 4 m, therefore the necessary deck space with a minimum weight capacity of 3.5 $mt.m^{-2}$ can be listed as followed:

Table 3.11: *Minimum number of reactor units to produce the required hydrogen for the different flow designs and the deck space related to these reactor units.*

Configuration	NRA	N_{units} [-]	Deck space [m^2]
Flow Design-1	No	19	380
Flow Design-2	Yes	11	200
Flow Design-2+	Yes	33	660
Flow Design-3	Yes	33	660

3.4 Auxiliary equipment

The focus of the chapter has been very much on the reactor as it is the core installation of the offshore methane pyrolysis facility. However, as shown in the flow scheme, multiple auxiliary installations to the reactor are necessary to make the design a success. Depending on the size of the reactor and the auxiliary installations, possibly the current 150 m^2 available for all equipment is too limited. This would demand additional deck space on the N05-A platform or an entire new platform next to it. The access this a rough estimation on the area is given with a floor plan of all installations. All auxiliary installations are discussed separately including an indication for size, in the next section, these sizes can be converted into necessary deck space depending on the specifications of flow designs.

3.4.1 Decompression and compression

The processed natural gas from the already in place equipment on the platform has a pressure beyond the operating pressure of the methane pyrolysis reactor. Hence, the pressure should be decreased to match the design pressure of the reactor units. The pressure will be the highest in the earlier stages of the gas field lifetime and drops over time. This continues until the compression module is activated to boost the natural gas production, afterwards the pressure once again drops until the field is abandoned.

Before transporting the produced hydrogen on the platform to shore, the hydrogen mixture (outflow gas with nitrogen, methane and hydrogen) should meet the operating pressure of the pipeline to shore. To make this possible next to the compression module which boost the production, an additional compressions station should be installed.

The sizing of the decompression and compression installations is based on the compression module, designed as a module for N05-A. The current pressure gauge of the compression module on N05-A has been assumed to be able to bridge the pressure gap between the outflow of the reactor rand the pipeline operating pressure. Therefore, for a flow of 6 million Nm^3 of gas the same dimensions apply. The decompression installation in the design should do the exact opposite of the compression installation, as the gas was at pipeline conditions before entering the methane pyrolysis facility, including the reactor and auxiliary equipment. Therefore, the decompression unit is assumed to have the same flow capacity at the same size.

Table 3.12: *Capacity of decompression and compression station relative to their size*

Installation	Max capacity (M Nm3)	Size (m)		
		Width	Depth	Height
Decompression station	6	12	15	4
Compression station	6	12	15	4

3.4.2 Heating

Taking into account the N05-A platform will be emission free under standard operating conditions, the conventional methane burners cannot be applied as it would emit CO_2. Therefore, initially electrical heating has been chosen to provide the necessary thermal energy to heat up and keep the reactor temperature at the preferred level.

There are not many electrical heating methods that can reach the demanded temperature for this project. One of the existing methods is an electric arc furnace (EAF). In steel making for instance the scrap steel is melted due to the high-voltage electrified arcs produced by the electrodes in the furnace. For offshore methane pyrolysis, this however induces a disadvantage as the method demands of continuous moving reactor fill between the reactor and the electric arc furnace to keep the medium at temperature. This is difficult with the current design that includes a large number of columns. Moreover, moving equipment tends to lead to more unscheduled maintenance (Karlberg & Pacey, 1989).

Next to EAF, also coil heaters have been indicated as electrical heating capable of meeting the demanded operational temperature (Phillips et al., 2020). Thick metal spirals, that are wrapped around the reactor, can maintain a temperature up to 1400 ˚C in long life usage (Micopyretics Heaters International, n.d.). The research focusses on the development of the reactor therefore extensive designing on the coil heating is out-of-scope. Since the coil will be integrated with the reactor the direct spacing is not included. However to process the incoming flow of electricity a transformer and rectifier unit will be necessary to convert the high-voltage inflow of electricity to the coil required specifications. For a gross estimation the sizing of a transformation station for offshore wind has been utilized as reference (Siemens, 2017). Two units are necessary to process the electricity produced by 588 MW of wind turbines. Assuming they operate at maximum capacity the sizing is listed in Table 3.13.

Table 3.13: *Capacity of transformer and rectifier unit relative to its size.*

Installation	Max capacity (MW)	Size (m)		
		Width	Depth	Height
Transformer and rectifier unit for heating	7 GWh [a]	13.1	7.3	7.7

[a] Two units are installed at the 588 MW wind farm Beatrice. When operating at maximum capacity for 24h, 14.1 GWh of electricity is processed.

Next to electrical heating, possibly, a part of the produced hydrogen could be burned to provide the necessary heat for the reactor. In a flame of hydrogen, the molecules would react with oxygen resulting in water, still preventing any harmful emissions. This does require a complex redesign of the reactor unit, as it should fit multiple burners in the limited space between the reactor columns, and both air with oxygen and water should be able to enter and exit the reactor unit. Moreover, burning hydrogen, even though the reactor unit is in a close compartment, would require significant extra safety measures.

3.4.3 Cooling

Before entering process equipment, the hydrogen mixture coming from the reactor units should be cooled to prevent equipment thermal damage that may be caused by high temperatures. Also, heat can be exchanged with the natural gas flow to decrease the initial heat demand. Hence, cooling improves both the efficiency and the durability of a facility.

The temperature can be reduced by transferring the heat to a cooling medium. This medium could be water, as it has a high thermal conductivity, but also air or the natural gas before it enters on of the reactor units. Heat transfer depends on surface area and therefore a large contact surface is necessary, most of the time resulting in a large vessel consisting of a larger number of small pipes. When heat is transferred to the air, no outer layer around the pipes is needed. However, when the heat is exchanged with water or natural gas, an outer layer around the pipes is installed to contain the cooling medium. Also, direct quench cooling exist, wherein cool gas or water is sprayed into the hot gas. However, this is not preferred for the current design as the added molecules would hinder the later purification steps for high-purity hydrogen.

Figure 3.7: *(a) Syngas cooler. The smaller cylinders perpendicular to the pipes are for inlet and outlet of the cooling medium. (b) Top view of a syngas cooler. It shows the large number of pipes, present to create a large contact surface with the cooling medium are visible (Weidenfeller et al., 2016)*

The dimensions of the cooling installation are based on a syngas cooler, which cools the gas from SMR. Analysing the pictures from Figure 3.7, the sizing for a single syngas cooler is estimated to contain 240 pipes with a 0.05 m diameter, and a length of 20 m. This results in a total contact surface between the pipes and the cooling medium of 754 m^2.

Table 3.14: *Cooler capacity relative to its size.*

Installation	Max capacity (M^2)	Size (m)		
		Width	Depth	Height
Cooler	754	3	3	20 [a]

[a] When water as cooling medium is applied, a vertical configuration is preferred as gravity helps to continuously refresh the cooling medium.

3.4.4 Carbon handling

Even though the carbon can only contain a minor percentage metal due to the filtering molten salt layer at the top of the reactor, the solid carbon outflow of the reactor unit does contain a percentage salt. Research on separation of salt and solid carbon does exist on a laboratory scale. There, filtration efficiency in separating salt and carbon from each other has been tested, with promising results. A filter was able to separate salt from a carbon-salt homogeneous mixture with the rate of filtration depending on the pore size of the filter. The salt content can be further decreased by a water wash step. NaCl and NaBr in this case would be separated by floatation (Bhardwaj et al., 2021).

To estimate the size of the carbon handling installation, preferable a comparison with a currently operational commercial methane pyrolysis plant would be made. However, since the only existing plant from Monolith, utilizes a different technology, this is impossible. The plasma arc in a purely gas filled reactor, decomposes the methane molecules with a very high temperature, therefore, no mixing between metal, salt and solid carbon occurs.

The second-best option was an advanced design of a methane pyrolysis installation. The installation from C-ZERO has many similarities with the molten metal and salt design in this research. The reactor is filled with molten salt with an operational pressure between 10-20 bar and temperature of 1000 ˚C (Jones, 2021). The carbon handling in their design is therefore assumed to be comparable for a molten metal and salt reactor. The grey installation next to the reactor in Figure 3.8, handles the solid carbon. The system seems to contain a backflow of salt to keep the melt level at the preferred height looking at the yellow and red piping with the reactor. The grey installation is assumed to produce solid carbon with a 0.001 mol% salt just as in Section 3.1. The actual composition of the outgoing solid carbon flow can however be much larger. This is research gap, that will be further outlined in the discussion.

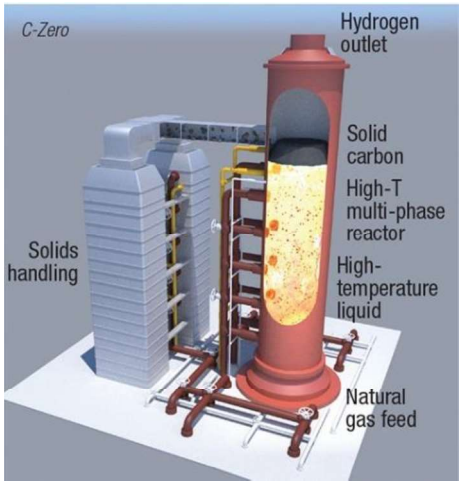

Figure 3.8: *Molten metal reactor design from C-ZERO (Jones, 2021)*

The size of the carbon handling station has been determined based on the sizing of the reactor. Hence such a station is expected to need twice the deck space of a reactor but with a lower height.

Table 3.15: *Size of carbon handling relative to the reactor sizing.*

Installation	Max capacity (-)	Size (m) [a]		
		Width	Depth	Height
Carbon handling	-	$D_{reactor}$	$2D_{reactor}$	$0.75H_{reactor}$

[a] Sizing depends on the scale of the methane pyrolysis reactor. D indicating the reactor diameter and H the reactor height.

3.4.5 Carbon transport

As the carbon properties are depending on the filtration process, the transport component of the carbon chain is still unsure. However, two methods have been identified that could potentially transport the carbon both for carbon with a high viscosity and for the dry-powder carbon. Continuous transportation will be necessary since the weight limitation on the platform restrict storage. The transport from the platform to shore will be executed by a coaster vessel or an offshore supply vessel, which will operate well in the close to shore area the N05-A platform is located. Long distant onshore transportation has been proven to be most efficient to execute by train (Jones, 2021). The most unsure step in the transportation chain of carbon will therefore be transport from the filtration station to the vessel. It would therefore be advisory to focus on this aspect of the chain in future research. Even though design of the carbon transport chain is out of scope the most applicable technologies have been stated in this section.

Offloading buoy

In case the filtration process will still result in carbon with a high viscosity, for instance due to a relative high contamination with salt, transporting will be difficult. As the high viscosity will result in sticky properties moving transport methods like a conveyer belt will be impractical. However, the oil and gas industry already have experience with the transportation of high viscosity like heavy crude oils. Heavy crude oils are offloaded from the platform by a direct pipeline to shore or an offloading buoy. Due to the limited volume production of carbon relative to heavy crude oil production an offloading buoy will be the most interesting options to investigate in case of a high viscous carbon.

Heavy crude oils cannot flow easily through a pipeline and therefore improvement the is improved. Some of these methods can be applied in case the viscosity of the carbon show to bother a continuous process (Saniere et al., 2004). One option is to mix the carbon with water. Water is abundant offshore and the emulsion will have time to settle in the vessel. Moreover, a more complex application of water called core annular flow exists. A water film creates a surrounding film that acts as a lubricant limiting the resistance of the carbon to a comparable level to just water. Furthermore, the carbon that leaves the reactor will have a temperature around 1000 °C, this eases transportability of the carbon as temperature decreases the viscosity. On the other side, the operating conditions of the transport system should be considered as the cargo ship cannot transport temperatures above 55 °C

Conveyer

Carbon in dry and clean conditions will act as a powder comparable to sand even though sand tends to contain larger particles (Ali et al., 2020). This enables the opportunity to transport the carbon with a pneumatic conveyer. This type of transport uses a vacuum or airflow to suck or blow the participles to another receiving compartment where the powder can settle down. One important aspect of applying this method is that using air to transport to carbon will induce the risk of reactions between carbon and oxygen in the air, resulting in production of CO_2. This is not in line with the vision of the research. Hence, the design options are limited

to inert gas, i.e. argon, nitrogen, as medium to transport the carbon without reactive behaviour with the transport gas. In a system with air as transport gas the gas in the receiving compartment can be vented. As the system uses an inert gas, recycling is most likely necessary.

(a) Offloading buoy

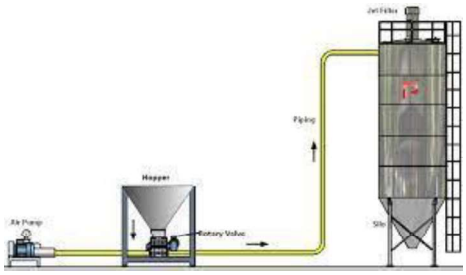

(b) Pneumatic conveyer system

Figure 3.9. *Different methods for transporting carbon black (NOV, 2022; Polimak, 2022)*

Due to the solid state of the carbon, a relative high density around 2100 $kg.m^{-3}$ is achieved. Hence the flow volume of the carbon will be much smaller than the gaseous hydrogen mixture flow. As example, even when all methane from the natural gas feed would be converted into solid carbon and hydrogen (~2400 mt C_s per day). A flow of 50 m^3 C_s per hour should be processed. The sizing of the transport system is therefore of neglectable scale in comparison to the installations related to the gas flow on the methane pyrolysis facility related installations and not included in the final estimation to determine the total necessary offshore deck space by the entire installation.

3.4.6 Purification of gas

The most utilized technology for separation and purifying of hydrogen in a hydrogen rich stream is pressure swing adsorption (PSA)(Kalman et al., 2022). By passing a mixture of gases over an adsorbent material, selectively one or more of the gases in the mixture is adsorbed. The process of adsorption occurs when gas molecules are attracted and held by the surface of an adsorbent material, such as activated carbon or zeolite. When selecting an adsorbent material to use in a PSA unit, it is important to consider the size of the gas molecules that need to be adsorbed. If an adsorbent material with the wrong pore size is used, it may not be able to effectively adsorb the desired gas molecules.

When separating hydrogen from hydrogen mixture, Zeolite 3A would be a suitable material since it has a pore size of 300 pm. The molecular diameter of methane (385 pm) and nitrogen (364 pm) are larger meaning they are adsorbed, whereas hydrogen (289 pm) passes through the system (Ismail et al., 2015). This results in a purified hydrogen stream. After the bed is saturated, the gas inflow is stopped and regeneration starts. By depressurizing the bed the larger molecules are discarded from the bed and the ability to adsorb fresh gases is restored. The outflow from the vessel with the larger molecules creates a second stream. Due to the need for regeneration (cleaning of the adsorbent bed), a continuous inflow of gas is impossible with a single vessel, therefore, most PSA system consist of at least two vessels.

Possibly, a separation step before all methane pyrolysis related installations, would reduce the necessary scale of the equipment. The gas flow of 6 million Nm3 is assumed to consist for 74.7 mol% of methane and 25.3 mol% of nitrogen. Therefore, separation of nitrogen would reduce the flow volume that requires processing massively. The air composition contains around 78 vol%. Nitrogen could therefore be vented to the atmosphere. The risk of producing harmful NOx is also extremely low, since the temperature of the gas flow is well below the reaction temperature of nitrogen and oxygen (Chou et al., 2007) . PSA units have also been employed to remove nitrogen from methane (Xiao et al., 2019), the same approach to determine the deck space as hydrogen purification is therefore applied. The installations will however have a different adsorption material fit for their purpose.

Figure 3.10: *The G4 model pressure swing adsorption unit from Xebec for hydrogen separation from SMR-syngas (2016)*

The sizing is based on the G4-model PSA unit from Xebec because it can purify a large flow of hydrogen rich syngas. The frame size of the equipment stays relative the same, also for smaller models, so with the deck space in mind, the largest model is the best choice. The sizing has been listed in Table 3.16.

Table 3.16: *Sizing pressure swing adsorption unit*

Installation	Max capacity ($Nm^3.hr$)	Size (m)		
		Width	Depth	Height
Pressure swing adsorption	29000	12.8	5.9	5.6

The G4 model is the best PSA from Xebec. It 9 beds with a 60″ diameter and a maximum operating pressure of 17 bar.

3.5 Total deck space

The design platform at N05-A contains two decks with equipment for processing the 6 million Nm3 natural gas. The height of installations on the top deck is limited to 5.2 m due the operational range of the crane and spacing between the two deck is 8 m. Each deck facilitates 45 x 27m of operational area, however on the current platform most space is already allocated to the gas processing equipment. Only 150m^2 would be available at the top deck for all reactor units and auxiliary equipment.

The necessary deck space is determined for the four flow designs from Section 3.1. Combining the specification with the sizing of the auxiliary equipment in this section defines the necessary deck space. The weight has not been taken into account in this analysis. Due to the varying requirements between the flow designs, the necessary deck space will also change. An extra installation such as the PSA unit for nitrogen rejection, demands significant extra deck space, however it reduces the flow downsizing the installations later in the flow scheme.

The build-up of total necessary deck space of the four flow designs are listed in the tables below.

***Table 3.17**: Necessary offshore deck space for methane pyrolysis according to Flow Design-1, with a 81.4% conversion rate.*

Installation	Maximum necessary daily capacity		Estimated deck space (m^2)
Gas processing equipment [a]	6 million	Nm^3 gas	2350
Decompression	6 million	Nm^3 gas	180
Electrical heating	5.85	GWh$_e$	120
Methane pyrolysis reactor [b]	6 million	Nm^3 gas	380
Carbon handling	1950	mt C$_s$	760
Carbon transport	1950	mt C$_s$	-
Cooling [c]	9.6 million	Nm^3 H_2 rich gas	580
Compression for pipeline	9.6 million	Nm^3 H_2 rich gas	290
Total			**4660**
Total without current platform			2310

[a] Including 150 m^2 originally in place for entire methane pyrolysis facility

[b] The conversion rate increased from 81.0% to 81.4% between the flow design and reactor design phases. The necessary capacity could therefore be slightly higher in comparison to the numbers in Section 3.1.

[c] According to Setioputo et al.(2021), 1.66 m^2 is necessary to cool down 3300 Nm^3 /day 800 ˚C syngas with ambient air. This corresponds to 3020 m^2 for 6 million Nm^3 per day. This contact surface has been scaled to the flow of this flow design. Since the temperature of the system is expected to be around 1000 ˚C, an additional 50% contact surface is added.

Table 3.18: *Necessary offshore deck space for methane pyrolysis according to Flow Design-2, with a 66.6% conversion rate*

Installation	Maximum necessary daily capacity		Estimated deck space (m^2)
Gas processing equipment [a]	6 million	Nm^3 gas	2350
Decompression	6 million	Nm^3 gas	180
Nitrogen rejection	6 million	Nm^3 CH_4	700
Electrical heating	4.86	GWh_e	100
Methane pyrolysis reactor [b]	4.6 million	Nm^3 gas	200
Carbon handling	1600	mt C_s	400
Carbon transport	1600	mt C_s	-
Cooling [c]	7.5 million	Nm^3 H_2 rich gas	450
Compression for pipeline	7.5 million	Nm^3 H_2 rich gas	230
Total			**4610**
Total without current platform			2260

[a] Including 150 m^2 originally in place for entire methane pyrolysis facility

[b] The conversion rate increased from 62.5% to 69.7% between the flow design and reactor design phases. The necessary capacity could therefore be slightly higher in comparison to the numbers in Section 3.1.

[c] According to Setioputo et al.(2021), 1.66 m^2 is necessary to cool down 3300 Nm^3 /day 800 ˚C syngas with ambient air. This corresponds to 3020 m^2 for 6 million Nm^3 per day. This contact surface has been scaled to the flow of this flow design. Since the temperature of the system is expected to be around 1000 ˚C, an additional 50% contact surface is added.

Table 3.19: *Necessary offshore deck space for methane pyrolysis according to Flow Design-2+, with a 91.4% conversion rate*

Installation	Maximum necessary daily capacity		Estimated deck space (m^2)
Gas processing equipment [a]	6 million	Nm^3 gas	2350
Decompression	6 million	Nm^3 gas	180
Nitrogen rejection	6 million	Nm^3 CH_4	700
Electrical heating	6.66	GWh_e	130
Methane pyrolysis reactor	4.6 million	Nm^3 gas	660
Carbon handling	2190	mt C_s	1320
Carbon transport	2190	mt C_s	-
Cooling	8.6 million	Nm^3 H_2 rich gas	510
Compression for pipeline	8.6 million	Nm^3 H_2 rich gas	260
Total			**6110**
Total without current platform			3760

[a] Including 150 m^2 originally in place for entire methane pyrolysis facility

[b] The conversion rate increased from 90.0 % to 91.4% between the flow design and reactor design phases. The necessary capacity could therefore be slightly higher in comparison to the numbers in Section 3.1.

[c] According to Setioputo et al.(2021), 1.66 m^2 is necessary to cool down 3300 Nm^3 /day 800 ˚C syngas with ambient air. This corresponds to 3020 m^2 for 6 million Nm^3 per day.

Table 3.20: *Necessary offshore deck space for methane pyrolysis according to Flow Design-3, with a 91.4% conversion rate*

Installation	Maximum necessary daily capacity		Estimated deck space (m^2)
Gas processing equipment [a]	6 million	Nm^3 gas	2350
Decompression	6 million	Nm^3 gas	180
Nitrogen rejection	6 million	Nm^3 CH_4	700
Electrical heating	6.66	GWh_e	130
Methane pyrolysis reactor [b]	4.6 million	Nm^3 gas	720
Carbon handling	2190	mt C_s	1440
Carbon transport	2190	mt C_s	-
Cooling [c]	8.6 million	Nm^3 H_2 rich gas	510
Hydrogen purification	8.6 million	Nm^3 H_2 rich gas	1000
Second purification	1.4 million	Nm^3 H_2 rich gas	160
Compression for pipeline	8.0 million	Nm^3 H_2	220
Total			**7230**
Total without current platform			4880
Total without current platform incl. recycling [d]			5610

[a] Including 150 m^2 originally in place for entire methane pyrolysis facility

[b] The conversion rate increased from 90.0 % to 91.4% between the flow design and reactor design phases. The necessary capacity could therefore be slightly higher in comparison to the numbers in Section 3.1.

[c] According to Setioputo et al.(2021), 1.66 m^2 is necessary to cool down 3300 Nm^3 /day 800 ˚C syngas with ambient air. This corresponds to 3020 m^2 for 6 million Nm^3 per day. This contact surface has been scaled to the flow of this flow design. Since the temperature of the system is expected to be around 1000 ˚C, an additional 50% contact surface is added.

[d] With two steps of 90% recovery PSA, 0.6 million Nm^3 waste gas, with a high percentage methane is produced. Bringing this back into the system continuously has been assumed to increase the platform scale with 15%

In order to conclude the offshore design phase, the necessary deck space is expressed as percentage of the deck space N05-A has (2350 m^2). It provides reference and could be used as multiplication factor with cost form the gas production and processing installation in the levelized cost of hydrogen analysis. Since this deck space is necessary for processing This area 6 million Nm^3 with the offshore methane pyrolysis facility, linear scaling of the deck space to 150 m^2 would result in the maximum possible gas flow that can be converted on the N05-A platform that would meet the requirements.

Table 3.21: *Overview of total deck space and maximum possible flow on 150 m2 at each flow design*

Flow design	Necessary additional deck space at 6 million Nm^3 gas per day		Possible gas flow on 150 m^2 per day
	[m^2]	[%]	[million Nm3]
Flow Design-1	2310	100	0.39
Flow Design-2	2260	100	0.40
Flow Design-2+	3940	160	0.24
Flow Design-3	5820	240	0.18

Rounded to the nearest tens in square meters and tens of a percent.

3.6 Final results and discussion

The primary objective of the design phase was to present a comprehensive offshore design for a molten metal and salt reactor. To achieve this goal, an examination of the limitations and requirements of offshore designing was necessary. Utilizing this information, the most optimum design for the reactor was determined within the constraints imposed by these limitations and requirements. Additionally, an assessment of the required deck space for the reactor, as well as auxiliary equipment, was conducted to ensure the proposed design is functional and feasible.

3.6.1 Final results

A methane pyrolysis facility including auxiliary equipment demands much more deck space than the currently available 150 m2 on the N05-A platform to process the 6 million Nm3 of natural gas produced daily on the production plateau. As follow-up two aspects were examined. The minimum necessary deck space to process the entire 6 million daily Nm^3 natural gas production and the maximum possible gas volume a methane pyrolysis facility could process on the 150 m^2.

Extension of deck space

When adding the deck space of the reactor units and the auxiliary equipment together the total necessary deck space, on top of the current platform for gas production and processing, is at least 2260 m^2 which corresponds to the addition of a platform with the same size as the N05-A platform.

In this lowest flow design, the gas flow is rejected from the gas flow and vented to the atmosphere. This reduces the necessary capacity of the installations downstream as the volume flow of gas is reduced. Comparing the situation the Flow Design-1 with the least number of installations, it has no PSA for nitrogen rejection, the necessary deck space is slightly higher but comparable. The higher methane mol% in the gas, reduced the minimum methane conversion to reach the same hydrogen mol% in the outflow as steam methane reforming. This offers various benefits, such as a reduced demand for heat and a reduction in the amount of carbon that needs to be transported. Despite these benefits, it can be argued that flow scheme 1 still performs better as the absolute production of hydrogen is higher due to the higher conversion rate. This trade-off will be further evaluated in the economic analysis in the next chapter.

A high conversion rate with nitrogen rejection, indicated with Flow Design-2+, demands a significant extra amount of deck space. For a conversion rate of at least 90% a minimum of 3940 m^2 is needed on top of the current platform space. Producing hydrogen backbone quality, as in Flow Design-1, is the most space-demanding flow design. Including double purification steps and recycling of the waste stream from these steps, 5610 m^2 of extra deck space is required.

Current deck space

Downscaling the necessary deck spaces requirements, to the available 150 m^2 deck space on N05-A, results in a significant reduced maximum gas flow that could be processed without constructing platform(s) for extra deck space. When linearly scaling down the size, just 0.40 million Nm^3 of natural gas can be processed daily with Flow Design-2. With Flow Design-1, this barely decreases as 0.39 Nm^3 of natural gas can be processed daily. For high conversion with nitrogen rejection 0.24 Nm^3 can be processed.

The flow reduces further when producing high-purity hydrogen that meets the requirements of the hydrogen backbone. In addition to the nitrogen rejection step, a hydrogen must be purified with PSA installations to purify the hydrogen rich output. On top of this the waste flow from the PSA must be recycled. With this setup, it is estimated that 0.18 million Nm3 of natural gas could be processed daily.

3.6.2 Discussion

The current design has prioritized adhering to the production plan of N05-A, with the aim of processing a maximum of 6 million Nm^3 per day. However, it is not necessarily disadvantageous to only partially convert the flow into hydrogen, particularly when the flow decreases to a level that can be completely handled by the 150 m^2 installation. Over time, the hydrogen percentage in the gas mixture in the NGT pipeline will increase until the flow reaches the design flow of the methane pyrolysis installation. At that point, the installation with hydrogen purification on the platform will fully contribute to the flow of high purity hydrogen through the pipeline.

Nevertheless, the maximum flow possible within the available 150 m^2 is so limited, an installation would only produce a small volume of the entire flow of N05-A at any moment in time. When additional offshore deck space would be unfeasibly, it could be more reasonable to redirected to gas flow with an extra pipeline to another gas network to prevent mixing when hydrogen would significantly flow through the NGT-pipeline. Or the pipeline could be directly connected to shore since the platform is relative close to shore. This again prevents mixing but does offers the opportunity to convert natural gas into hydrogen with onshore methane pyrolysis, without involvement of other companies.

Installation performance and deck space uncertainty

The determination of the necessary deck space for auxiliary equipment and reactor units is based on gross estimates. It is important to note that this space may vary. Since the scaling of equipment is not always linear, as an installation that processes twice the flow may not necessarily require twice the size (Rasmussen, 2011). This applies in both directions; a smaller deck space may be sufficient for processing a maximum of 6 million Nm3, however, the maximum processable flow on 150 m2 would decrease.

Furthermore, assumptions regarding auxiliary equipment may not align with actual conditions. For instance, if the compression gauge of the current installation on N05-A would cover half of the pressure difference between the methane facility and the pipeline requirement, it would demand twice the number of installations, with linear scaling. Additionally, variations in the recovery rate of pressure swing adsorption can have a

significant impact on the system. A decrease from 90% to 80% could result in 10% more nitrogen remaining in the system, thus increasing the size of all downstream installations. This effect is further exacerbated when considering the implications of recycling in Flow Design-3.

The reactor performance has been calculated using the model outlined in Chapter 2. However, this model is subject to uncertainties such as the gas holdup, which has a margin of error of ±30%. As a result, a single reactor unit may perform differently than the results presented in Subsection 3.3.2. The current design is limited by the bounds established by experimental background of the correlations in the methane pyrolysis model, although it is possible that methane pyrolysis may perform effectively outside of these bounds. A deviation in reactor unit performance, whether an increase or decrease, would correspond in the opposite modification of the necessary number of reactor units.

However, the installation with the highest uncertainty is the carbon handling and separation. Just like the reactor units for methane pyrolysis this is a first-of-a-kind installation, yet has not been thoroughly investigated and designed. Metal has been assumed to be fully captured in the molten salt filter layer and the carbon handling and separation installation from C-ZERO is assumed to create an outflow with just 0.001 wt% salt as that has been indicated as economic threshold (Kang et al., 2019). Does the installation include the water washing that has been indicated in laboratory scale research or how clean is the reinjection of molten salt. The installations raise questions however the lack of reference material forced the writer to utilize this installation. In the worst-case scenario, it could even be a project limiting factor when the reactor fill outflow, stuck to the solid carbon, is larger than the feasibility of refilling the reactor columns. More (real-life pilot) research on this subject would therefore definitely be required.

Heating and electricity supply

Depending on the conversion rate of the methane pyrolysis facility a significant inflow of electricity will be necessary to provide the required heating. This has been taken into account by installing a transformer and rectifier on the platform to process and transform the electricity to the coil heating frequency, voltage and ampere. The cables are all assumed to be covered by the supplier of electricity and the cost are assumed to be part of the price of electricity.

The N05-A platform is currently planned to be entirely powered by the German Riffgat wind farm when it produces enough electricity. However, in full production, the total 108 MW wind turbines can only generate 2.59 GWh of electricity per day. This is inadequate to meet the electricity demand, even in flow scheme 2, which has the lowest demand of 4.86 GWh per day. A 203 MW wind farm would be necessary to satisfy peak electricity demand, and this requirement would only increase with higher conversion rates. Additionally, it is important to note that wind farms do not operate at maximum capacity throughout the year and may produce minimal electricity during periods of low wind. Therefore, an additional source of electricity, such as renewable energy sources non-dependent on wind or electricity from the German shore, like N05-A has for low wind periods, would be necessary to ensure adequate power supply. Important to take in mind has been de difficulties on the German electricity

grid with power to larger consumers (Kurmayer, 2022), therefore a secure and reliable large-scale electricity supply from the shore is no guarantee.

These issues can potentially be circumvented by utilizing hydrogen as a fuel source. Combusting hydrogen would provide the necessary heat and independence from an electricity source. However, this would require a redesign of the reactor units to accommodate burners, as well as the implementation of additional safety measures. Lastly, the two options could be integrated by converting the hydrogen into electricity in a fuel cell. However, the feasibility of this option is uncertain as it would require additional deck space and result in increased conversion losses of hydrogen

Material assumptions

The material properties of Centralloy G 4852 Micro R alloy are extrapolatd outside the Larson Miller parameter range. The behaviour is relative constant, so error margins beyond the range are expected to be small. However, to eliminate this uncertainty, the material should be tested beyond the maximum LMP = 36.8.

Further research on potential materials for the reactor walls would be of interest. The current material has been used in steam methane reformers, however, the design considerations for offshore applications differ from those of traditional SMR. While the temperature requirements are similar, the weight of the wall material for instance is of greater importance in this context than in standard SMR.

Maintenance and safety

For maintenance and safety considerations the reactor units are split into multiple installations, with a thick insulation layer. However, more measures are probably be required to create a safe operating environment. Due to lack of hydrogen legislation, more research on the dangers of such a high hydrogen installation should be executed.

The selection process for the maximum column configuration of maximum height could also be re-evaluated from a maintenance and safety perspective and arguably the maximum height would be better as the columns are further from each other. The maintenance could be done inside the reactor unit when turned off, this is impossible with the close configuration when maximizing the number of columns.

4. Economic analysis and levelized cost of hydrogen

The technical feasibility of offshore methane pyrolysis on N05-A requires the construction of additional deck space to accommodate the processing of the entire flow. This can be achieved through the use of one or multiple extra platforms. In order to determine if the additional deck space required for nitrogen rejection and hydrogen purification is a worthwhile investment, the levelized cost of hydrogen (LCOH) will be calculated for all offshore flow designs outlined in Section 3.1. Flow Scheme. The lowest LCOH will then be compared with conventional hydrogen production technologies such as steam methane reforming (SMR) and autothermal reforming (ATR) that include carbon capture and storage (CCS).

Because the offshore methane pyrolysis installation is connected to a natural gas production project, it becomes dependent on well extraction. As a result, the operational expenditure (OPEX) for the project will not be constant over its lifetime due to the yearly variance in production. Therefore, simply dividing the total cost by the total kilograms of hydrogen it not a suitable approach to calculate the LCOH (€.kg^{-1}). Instead, to accurately determine the LCOH it is necessary to calculate the cost and production of each year of the project and discount it to the start of the project (Tang et al., 2022):

$$LCOH = \frac{\sum_i^n \frac{Total\ cost\ in\ year\ i}{(1+r)^i}}{\sum_i^n \frac{kg\ of\ hydrogen\ produced\ in\ year\ i}{(1+\mathrm{r})^i}} = \frac{\sum_i^n \frac{C_i + O_i}{(1+r)^i}}{\sum_i^n \frac{E_i}{(1+r)^i}} \quad (4.1)$$

Where C represents the CAPEX (million €), O the OPEX (million €) and E the energy value of the produced hydrogen (million kg H_2). The i indicates the year, n the lifetime of the project and r the discount rate.

The discount rate is an important factor in levelized cost of hydrogen calculations because it affects the relative value of costs and benefits that occur at different points in time. For example, a higher discount rate will reduce the present value of future costs and benefits, making them less significant compared to costs and benefits that occur in the present. This can have a significant impact on the levelized cost of hydrogen, therefore the analysis will be executed for multiple percentages. In this research the discount rate will equal the weighted average cost of capital (WACC) of the entire project. The WACC is an important measure for decision-making as it reflects the desired rate of return for an investment. If a project is not expected to meet the WACC , it may not be worth pursuing and the investment capital can be directed towards other opportunities that offer higher potential profits. The equation takes into consideration the proportion of debt and equity financing and the required rate of return on those investments in the project and is shown below:

$$WACC = \frac{V_e}{V_e + V_d} \times C_e + \frac{V_d}{V_e + V_d} \times C_d \quad (4.2)$$

Where V_e is the market value of the firm's equity and V_d of the debt. The C_e indicate the cost of equity (%) and C_d the cost of debt (%). The WACC very much depends on the industry as more risky industries apply a higher percentage. IRENA for instance utilizes WACC = 6% for today's calculations on renewable electricity and 10% for hydrogen (Emanuele et al., 2020).

The economic analysis will therefore be run for a couple of WACC percentages to show the influence on LCOH.

In the rest of the chapter the build-up of the capital expenditure, operational expenditure and hydrogen production are first introduced. Afterwards, the LCOH is discussed including a comparison with the LCOH from SMR and ATR.

4.1 Capital expenditure

The capital expenditure (CAPEX) of the entire chain of installations necessary to make a methane pyrolysis facility work, will consist of the different installations present in the flow designs. The most important installations are the reactor units but without the auxiliary equipment the facility cannot exist. In the economic analysis therefore the CAPEX for the current gas processing equipment, reactor units and auxiliary equipment are included. Each of these installations will be discussed separately and at the end of the section, the total CAPEX breakdown will be stated. This breakdown will be corrected for uncertainties like market fluctuations and contingencies, creating a low, medium and high scenario.

4.1.1 Current gas production and process facilities

The methane pyrolysis facility is an extension of the current N05-A platform that will produce from the eponymous gas field and surrounding prospects. The CAPEX for the gas production does not only contains the cost of the platform but also drilling, exploration, etc. The cost upfront for ONE-Dyas are assumed to be 500 million € (Omrop Fryslan, 2022).

4.1.2 Reactor units

The CAPEX of the reactor units consist of two part. The material cost of the reactor units and a Lang factor. In previous research that took into account the cost of molten medium methane pyrolysis, the cost of the reactor was commonly estimated on the cost of the reactor fill (Parkinson et al., 2017). The same approach is therefore implemented, however, also in this case the wall material has been adopted in the total cost. The CAPEX of the reactor units for Flow Design-1 is shown below. The CAPEX of the other flow designs can be found in Appendix A7.1.

Table 4.1: *Cost of material for methane pyrolysis installation of Flow Design-1. It consist of 19 reactor units with 54 columns with an average gas holdup of 20.8%.. The columns are 0.25 m in height, 0.44 m diameter and have 0.056 m thick walls*

	Volume [m^3]	Weight [mt]	Price [a] [€/mt]	Cost [million €]
Salt reactor fill NaCl	7.72	11	100	0.00
Metal reactor fill CuBi	23.17	207	6,240	1.29
Wall material	10.81	85	13,270	1.13
Total				2.42

[a] See Appendix A2 for background on material prices. Conversion $ to € has assumed to be 1.

The Lang factor accounts for e.g. manufacturing, construction, piping, engineering, etc. Multiplying the Lang factor with the material cost should result in the total cost of the installations. There are multiple Lang factors available and they depend on the kind of installation. The standard factors are $F_L = 3.10$ for a facility processing solids, $F_L = 3.63$ for a

facility processing solid-fluids and $F_L = 4.74$ for a facility processing fluids (Wain, 2014). Arguable both 3.63 and 4.74 apply, the reactor units do considers a gas flow, however, they also produce solid in the process. Therefore, a range with factors is utilized. Additionally, literature has been found that increased the Lang factor further due to the first-of-a-kind situation of methane pyrolysis (Parkinson et al., 2017). They utilized a very high $F_L = 10$.

Table 4.2: *CAPEX of methane pyrolysis installation depending on flow design, based on material cost for reactor units and Lang factor*

	Low [a] [million €]	Base [b] [million €]	High [c] [million €]
Flow Design-1	9	11	24
Flow Design-2	5	6	13
Flow Design-2+	30	40	84
Flow Design-3 incl. recycling	35	46	96

[a] Lang factor for solid-fluid installations, $F_L = 3.63$

[b] Lang factor for fluid installations, , $F_L = 4.74$

[c] Lang factor for first-of-a-kind methane pyrolysis installation, , $F_L = 10$

4.1.3 Hydrogen production and processing equipment

For the CAPEX of the auxiliary equipment, the following machines have been considered: decompression, nitrogen rejection, transformer and rectifier unit, carbon handling, carbon transport and hydrogen purification. Depending on the flow design, some installations can be installed onshore. The cost for heating elements are assumed to be included in the Lang factor at the reactor units. The auxiliary equipment did not fit onto the designated 150 m^2, therefore also the additional cost of deck space should be taken into account. The complexity of the machinery on the N05-A platform and the auxiliary equipment on the extra deck space, are assumed to be comparable (Van Wijk, 2022). Thus, the assumption is made that the cost per m^2 deck space is approximately the same between the two. Only pricing of the transformer and rectifier unit has been considered separately, due to the complexity and need for high-grade materials, the cost are expected to be significantly higher.

Since the project should in the end produce high purity hydrogen, an onshore PSA-unit is necessary when no hydrogen purification is taken into account offshore. The cost of this installation is therefore also included when the purification does not happens offshore. This is the case for Flow Design-1, Flow Design-2 and Flow Design-2+.

Auxiliary equipment and extra deck space

The CAPEX of the current gas production and processing facility can be utilized as a reference, only the cost for components not related to the platform should be eliminated. These cost, exploration, drilling, pipeline to NGT, etc. are assumed to account for 60% of the cost. The cost of the platform with equipment therefore comes down to 200 million €. The CAPEX of the auxiliary equipment with additional deck space, is therefore calculated by multiplying the necessary additional deck space in percentage from Subsection 3.5 with 200 million €. Therefore, when the necessary additional increase in deck space is 150%, the CAPEX of auxiliary equipment will be 300 million €. The deck space necessary for the transformer and

rectifier unit and reactor units is included in the necessary additional deck space. The deck space should be accounted for, however not the equipment on the deck, as this will be done separately. This is solved by multiplying the deck space allocated to these two installations with one-third of the platform price, as per consult with structural experts from ONE-Dyas indicated a 1:2 ratio between the cost for structural and equipment on an offshore platform applies (Van Wijk, 2022).

Transformer and rectifier unit

The cost to build a transformation platform for offshore wind electricity is 60 million € for a capacity of 500 MW of wind turbines (Offshore Wind Programme Board, 2016), which translates to a cost of 60 million € per maximum daily production capacity of 12 GWh. Since, again the structural costs are estimated to make up one-third of the platform cost and equipment costs make up the remaining two-thirds, the 60 million € reduces to 40 million €. The capital expenditures for the platform therefore come down to 3.33 million €/GWh.

Pressure swing adsorption unit

According to Parkinson et al. (2017), the implementation of a pressure swing adsorption (PSA) unit in conjunction with a steam methane reformer (SMR) facility, which achieved an 80% conversion rate of methane and had the capacity to purify 200,000 mt of purified hydrogen annually, incurred a cost of 18 million €, resulting in a cost of 0.09 million € per kiloton of hydrogen (kta H_2). This cost is consistent with flow designs 1 and 2, however, Flow Design-2+ has a significantly higher hydrogen content than SMR present in the PSA feed. For Flow Design-3 all above does not apply as it has an offshore PSA unit and not onshore. The cost for hydrogen purification on a higher purity flow should therefore be found. In the same paper, implementation of a PSA unit in conjunction with a methane pyrolysis installation that achieved a 96% conversion rate resulted in a decrease in cost to 8 million € (0.04 million €/kta H_2). As the PSA process can be run at a smaller flow rate to reach the 200,000 mt annual capacity, the size and cost of the PSA could be reduced. Scaling the costs between the two scenarios, and taking into account the 90% conversion rate of Flow Design-2+, it can be estimated that the cost would be 0.06 million €/kta H_2. Therefore, for flow designs 1 and 2, a cost of 0.09 million €/kta H_2 will be used, while for Flow Design-2+, a cost of 0.06 million €/kta H_2 will be applied. Due to the comparable molar size of nitrogen and methane, the onshore hydrogen purification has been assumed to also reject the nitrogen for Flow Design-1.

Table 4.3: *Overview of auxiliary equipment CAPEX*

	Deck space, including auxiliary equipment [a] [million €]	Transformer and rectifier unit [million €]	Onshore pressure swing adsorption unit [million €]
Flow Design-1	172	20	20
Flow Design-2	183	16	17
Flow Design-2+	275	22	15
Flow Design-3 incl. recycling	423	25	-

4.1.4 Total CAPEX

Due to the early design phase of the facility, a range of 70% to 150% is applied to the CAPEX of the project to account for uncertainties, such as fluctuations in reference material costs and contingencies. (Wain, 2014). To capture the entire range of possibilities, the low scenario from the reactor unit has been multiplied with 70% and the high scenario with 150%. For flow scheme 1 this results in the following build-up of project CAPEX as seen in Table 4.4.

Table 4.4: *CAPEX for Flow Design-1*

	Low [million €]	Base [million €]	High [million €]
Gas processing	350	500	750
Reactor units	6	11	36
Auxiliary equipment & extra deck space	120	172	257
Transformer	14	20	29
Onshore PSA	14	20	31
Total CAPEX	**491**	**704**	**1,074**

The build-up for the other flow designs can be found in Appendix A6.2, however to compare the CAPEX of the various flow designs, the range for the total CAPEX of them are listed together.

Table 4.5: *CAPEX range for all flow designs*

	Flow design	Low [million €]	Base [million €]	High [million €]
Flow design	1	491	704	1,074
Flow design	2	493	706	1,069
Flow design	2+	573	828	1,309
Flow design	3 [a]	671	969	1,530

[a] Including recycling

The table illustrates the correlation between flow designs and the corresponding capital expenditure for low, base, and high scenarios. It demonstrates that as the flow in the designs increases, there is a tendency for higher values for low, base, and high. However, Flow Design-1 is an exception to this trend, as the combination of nitrogen and hydrogen rejection onshore reduces the need for offshore deck space and equipment, resulting in a larger flow for a comparable investment as Flow Design-2. Flow Design-3, despite having the same conversion ratio as Flow Design-2+, has a significantly higher price in all scenarios. This can be attributed to the increased offshore infrastructure required for hydrogen purification, including the additional deck space. Also, the increased flow resulting from the recycling of the waste stream from the hydrogen purification process necessitates additional cost for a size increase of equipment and deck space. This results in a higher CAPEX, however, the potential for increased hydrogen production may ultimately offset the additional costs

4.2 Operational expenditure

The operating expenditure (OPEX) are the cost related to the day-to-day operations of the project. It has been divided into three main parts that together define the variable cost of the project. All parts will depend on the inflow of natural gas and production of hydrogen and will be quantified in a low, base and high scenario, just like the CAPEX. The three parts that describe the OPEX are: (i) the cost of natural gas, (ii) the cost of electricity and (iii) the cost of carbon handling.

4.2.1 Natural gas

As ONE-Dyas in this research is assumed to both produce the gas and operate the methane pyrolysis plant, the natural gas operational cost are determined with the unit technical cost (UTC) instead of the market price. The UTC describes the cost relative to the gas flow and is set from 10 to 30 $.BOE^{-1}$. Approximately one-third of the unit technical cost are allocated to the operational cost, therefore dividing the UTC by three will create a identifier for the OPEX cost relative to the gas flow. The preferred unit for range calculations is €/MWh. Consequently, the conversion from US dollars to euros (at a rate of €1 : $1) and from barrels of oil equivalent (BOE) to megawatt-hours (MWh) (at a ratio of 1.7 MWh : BOE) is conducted. This results in the following range:

Table 4.6: *OPEX price for natural gas.*

	Low [€/MWh]	Base [€/MWh]	High [€/MWh]
Unit technical cost	3.33	6.67	10.00
Operational cost	1.96	3.92	5.88

4.2.2 Electricity

Electricity demand has a significant impact on the project operating expenses (OPEX) as it determines the amount of energy that must be purchased to meet the demand. The main demand comes from heating the reactor units but also the electricity demand for the gas processing and the auxiliary equipment has been taken into account.

Heating

The total demand of electricity for heating is based on the necessary heat to enable the reactions in the molten metal and salt column and keep the operating temperature at the set conditions. When operating at 100% efficiency the only energy demand would be the energy needed to empower the endothermic methane pyrolysis reaction, this cost 5.2 $MWh.mt^{-1}$ H_2. However, due to losses in the entire facility additional electricity is required. The efficiency of the facility is set to 58% which is based on papers on methane pyrolysis operations (Sánchez-Bastardo et al., 2020). Therefore, the energy demand of the installation increases from 5.2 to 9.0 $MWh.mt^{-1}$ H_2. The efficiency in the paper does apply to a molten medium reactor but, the complex set-up offshore is not considered. The auxiliary equipment, that is not necessarily present in a methane pyrolysis plant, should therefore be added separately. Next to the reactor with heating only the carbon separation and handling and the cooling were assumed to be

included. In addition, the decompression, compression and eventual nitrogen rejection and hydrogen purification should therefore be taken into account.

Gas production and processing

The calculated electricity comsumption of N05-A platform is 126.18 GWh per year including 115.92 GWh for compression. This compression is not necessary from day one. After a couple of year the reducing pressure from the well is compensated by the compression module. However as the drilling rig also utilizes electricity via N05-A, the 126.18 GWh has been included as electricity consumption for the gas production and processing over the entire lifespan of the project.

Decompression and compression

The electricity cost associated with decompression and compression is determined by the electricity demand for compression on N05-A. determined by the electricity demand for compression on N05-A. While it is possible that decompression may generate energy through the use of specialized installations (Bielka & Kuczyński, 2022), this possibility is beyond the scope of this analysis. In this context, a standard reducer is utilized, under the assumption that all recoverable energy is lost during the process. The electricity demand for compression is estimated to be 115.92 GWh when the installation operates to compress 6 million Nm3. This cost can be scaled proportionately to account for variations in operating flow. This could be due to a larger peak flow, for a different flow design or the decay in gas production.

Nitrogen rejection and hydrogen purification

For an operational cost determination for the nitrogen rejection and the hydrogen purification, the electricity demand for PSA on biogas has been used as a reference. According to Pertl et al. (2010), electricity consumption cost 0.72 $MJ.Nm^{-3}$ equivalent to 0.2 $kWh.Nm^{-3}$. The decaying flow has been taken into account, reducing the electricity consumption over time for nitrogen rejection and hydrogen purification.

Development of electricity prices is highly uncertain due to the supply disruptions in the gas market, as well as the high volatility of this commodity in trading. However, in time, the electricity price is expected to decrease to a situation with stable lower electricity prices. Prognos (2022) estimated this to reduce to 66-98 €/MWh by 2030 for electricity in Germany. Since this analysis includes the massive increase in price in 2022 and the N05-A platform is connected to German offshore wind and shore, the same range is implemented.

Table 4.7: *Electricity price range for determination of the electricity OPEX*

	Low [million €]	Base [million €]	High [million €]
Electricity price	66	84	99

The total electricity cost per installation discussed above are listed below in Table 4.8. As discussed in the introduction of Chapter 4, OPEX needs to be discounted to take into account the value of time. Hence, the discounted cost are also included for a discount rate r=10%.

Table 4.8: *OPEX total electricity OPEX per installation for Flow Design-1*

	Low [million €]	Base [million €]	High [million €]
Gas production	167	212	247
Discounted	*71*	*90*	*105*
Methane pyrolysis	752	957	1117
Discounted	*511*	*651*	*759*
(De)compression	57	72	84
Discounted	*46*	*59*	*69*
Pressure swing adsorption	311	396	462
Discounted	*212*	*269*	*314*
Total	**1286**	**1637**	**1910**
Discounted	***840***	***1069***	***1248***

The electricity OPEX for the electrical heating of the reactor units is the highest cost component of the listed electricity demanding installations. The cost for pressure swing adsorption are relative low in comparison to other Flow Designs, as there is not PSA installation for nitrogen rejection on the offshore platform therefore nitrogen rejection and hydrogen purification can be combined when the right adsorption bed is selected.

4.2.3 Carbon handling and transport

The operational costs associated with carbon handling primarily consist of the transportation of carbon. The separation and handling on the platform is considered to be part of the operational expenditure related to facilities' electricity. The shore has been designated as the transfer custody point, thus a separate party will be responsible for handling the solid carbon from that point onward. It is possible that the flow of solid carbon may generate revenue if it is processed appropriately, however, it is assumed that the carbon will be transferred at no cost for both parties. A roundtrip from the platform to Eemshaven and back is assumed to be 100 km long. Two ships have been identified for possible collection of the carbon black and transport to shore: (i) a small cargo carrier for coastal transport and (ii) an offshore supply vessel.

Table 4.9: *Carbon shipping properties based on maximum production of solid carbon*

Range	DWT [mt]	Maximum trips during peak production [year^{-1}]	Emissions per trip [mt CO_{2eq}/DWT]	Charter rate [a] [1000 €]
Coastal carrier [b]	10,000	68	0.00035	10 - 15
Supply vessel [c]	800	846	0.01200	10 - 15

[a] Assumed to include all cost

[b] Small cargo carrier capable of shipping 10,000 mt in close to shore regions (Handybulk, 2023)

[c] Offshore supply vessel can take 100 skips of 8 mt per trip (Van Wijk, 2022)

Since there should be a ship to receive the solid carbon at any time, a permanent charter rate of a single ship should be taken into account. However, when the cargo capacity of a ship is reached, it becomes necessary to secure an extra vessel in order to ensure a seamless flow of operations. On the days the current ship at the platform would sail back to shore to offload the carbon black, two ships would necessary. For the coastal carrier this would only happen 68 days a year at peak production. However for the supply vessel, two should be chartered on every day of the year as multiple trips are made each day. Since the platform is relative close to shore it, the time required for unloading and sailing is assumed to be less than the time needed for loading at the platform, thus making it unnecessary to charter more than two ships per day. Preferably, the transport is executed by the cargo carrier since it has a much larger deadweight tonnage (DWT) limiting the number of trips from the platform to shore and it can transport cargo at much less emissions compared to the offshore supply vessel relative to the transported cargo weight. However, the ship has not been designed for loading at an offshore platform, therefore, also the supply vessel has been considered. The charter rates of both ship are comparable between 10,000 and 15,000 € a day with the base case equalling the average of the range.

The emissions of shipping has been analysed, and it has been determined that during peak production, the emissions of CO2 would be approximately 8,000 metric tons per year in the high case scenario for offshore vessels. While this level of emissions is not desirable, in perspective, this is less than the average annual emissions of an individual in the Netherlands (Data common, 2019). Furthermore, with investments in carbon offset projects at a cost of 100 € per metric ton of CO_{2eq}, the total cost over the project life would be relatively minimal, at less than 5 million €. As a result, this flow of emissions has been disregarded in the operational expenses calculations.

4.2.4 Total OPEX

All operational cost of the project can be broken down to the three main categories: Natural gas, electricity and carbon handling. In Table 4.10 they are listed and for each category, the table shows both the absolute cost in million € as the discounted cost with a 10% discount.

Table 4.10: *Build-up of OPEX for Flow Design-1 consisting of natural gas, electricity and carbon handling*

OPEX	Low [million €]	Medium [million €]	High [million €]
Natural gas	187	375	562
Discounted	*127*	*255*	*382*
Electricity	1286	1637	1910
Discounted	*832*	*1059*	*1236*
Carbon handling	77	116	155
Discounted	*34*	*55*	*76*
Total	**1551**	**2128**	**2627**
Discounted	***993***	***1369***	***1694***

The operating expenses of a methane pyrolysis project have been analysed for different scenarios, and have been broken down into several categories for comparative purposes. The analysis revealed that the cost for electricity represents the largest proportion of the total OPEX. On the other hand, the cost for natural gas is relatively low compared to conventional reforming technologies. This can be attributed to several factors. Firstly, the heating process in the methane pyrolysis project is executed using electricity, thus eliminating the need to burn natural gas and resulting in the allocation of these costs to electricity. Additionally, the natural gas OPEX is based on the technical costs of operations rather than the market price of natural gas, as the company ONE-Dyas operates both the gas production and processing and the methane pyrolysis facility. At last, from a cost perspective the shipping transport of carbon is feasible as in comparison to natural gas and electricity the expenses are limited. In order to compare the different flow designs for the total OPEX, both absolute and discounted values are shown.

Table 4.11: *OEPX range for all flow designs*

	Flow design	Low [million €]	Base [million €]	High [million €]
Flow design	1	1,551	2,128	2,627
Discounted cost		993	1,369	1,694
Flow design	2	1,488	2,000	2,434
Discounted cost		949	1,280	1,561
Flow design	2+	1,741	2,356	2,880
Discounted cost		1,123	1,524	1,865
Flow design	3 [a]	1,978	2,660	3,237
Discounted cost		1,274	1,718	2,094

[a] Including recycling

A comparison of the different flow designs reveals a similar trend as observed in the overview of the capital expenses (CAPEX). The operational costs of Flow Design-2 are the smallest and those of Flow Design-3 are the highest. The OPEX increases with an increasing conversion ratio, as more electricity is required for heating and the installations have to process a larger hydrogen mixture flow and solid carbon. However, it should be noted that the operational cost of natural gas remains constant across all installations, as the flow designs are based on the same production scheme with a maximum daily production capacity of 6 million Nm^3.

4.3 Hydrogen production

In order to determine the levelized cost of hydrogen (LCOH), it is necessary to divide the total cost by the total hydrogen production in kilograms. The hydrogen production is influenced by several factors. The largest driver is the inflow of natural gas produced and processed by the N05-A platform. Additionally, the chosen flow design also plays a significant role, as it affects the conversion ratio of the reactor and the potential recycling of the waste stream from hydrogen purification. Given that the hydrogen production and value of time are subject to variation, the final hydrogen production, similar to the OPEX, should be discounted. This is because the LCOH should reflect the cost of hydrogen and, with the same amount of money today, less hydrogen can be purchased in the future.

4.3.1 Natural gas production

The offshore natural gas production consist of a couple of phases. In the begin period no natural gas is produced as the installations needs to be constructed, afterwards the first wells are drilled increasing the production. The combined production of all the wells will reach the maximum capacity (6 million Nm^3 per day) of the natural gas installation after two year. The plateau represents the timespan that consist of the maximum production. After two years the combined production of all wells can be kept at the maximum production anymore and the decline phase begins, the production will slowly decline over the lifetime of the project, up to abandonment when the economic limit is achieved. Even though, in the decline phase the production slowly decreases, it has been interpretated as yearly steps, to simply implementation in the model. In Figure 4.1, the daily production of the project is shown. The production is generalized however it represents the behaviour of production in a gas project (Van Wijk, 2022). For the entire yearly flow the daily production should be multiplied with operational days in a year. The number of operational days is set to 95% of 365 days to account for maintenance and unexpected downtime.

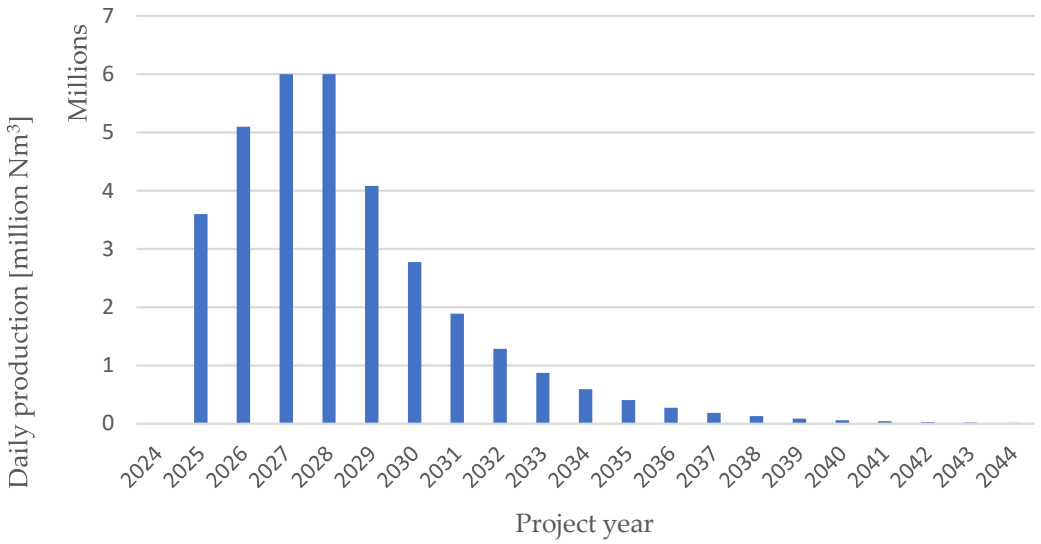

Figure 4.1: *Gas production on the N05-A platform from the eponymous gas field and surrounding prospects*

4.3.2 Conversion from natural gas to hydrogen

Due to the direct connection between the offshore natural gas operations and the onshore methane pyrolysis plant, the hydrogen production of the facility becomes non-uniform over the project lifetime.

The production therefore will have a comparable profile, however the methane conversion in the reactor units in combination with onshore or offshore hydrogen purification determines the final profile.

Conversion rate

In the offshore design phase, the minimum conversion rate of methane was determined at the peak of production. However, it is anticipated that as pressure decreases, there will be an increase in conversion within the reactor units outside of the peak production period. This behaviour is illustrated in Figure 4.2.

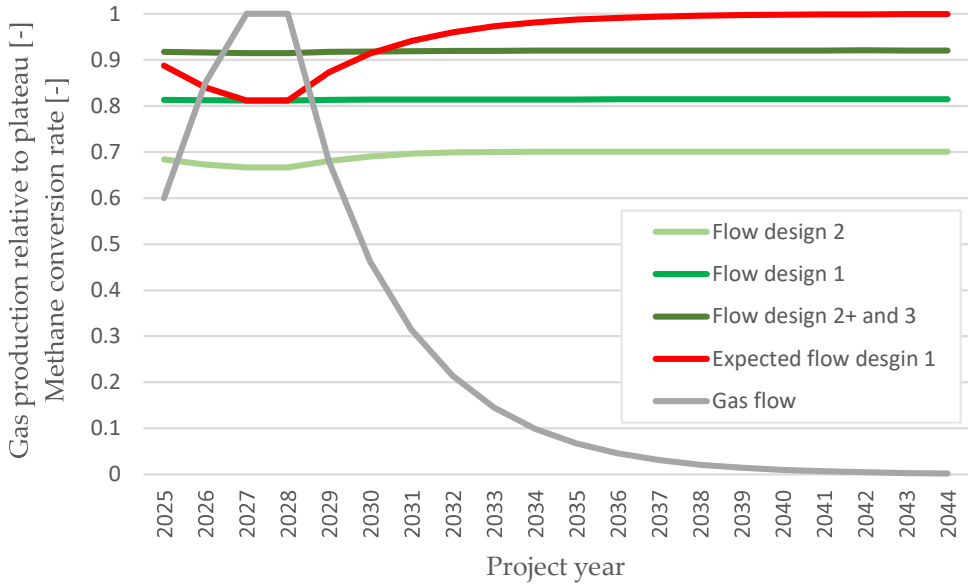

Figure 4.2: *Methane conversion over the project lifetime for the different flow designs, and the expected conversion when the pressure would be flow dependent.*

The results indicate a minimal increase in methane conversion for the various flow designs examined. This can be explained by the fact that the reactor units are already operating near their maximum conversion potential under the established pressure and temperature conditions. This also accounts for the greater increase in methane conversion observed in Flow Design-2, as it operates further from equilibrium.

As the flow rate decreases, the operating pressure within the reactor units may potentially be reduced, depending on the operational ranges of the auxiliary installations. This is expected to result in a methane conversion profile that is inversely proportional to the production profile. This can be observed in the red line for Flow Design-1. Thus, for Flow Design-1, the methane conversion will meet the specified requirements at peak production (81%), and

outside of this period, conversion could potentially approach 100% depending on the feasibility of reducing pressure.

Production

The production of the hydrogen, including nitrogen and unconverted methane, is obtained through the combination of natural gas production and the conversion rate in the reactor units. The flow design of the process can have a significant impact on both the flow volume and composition of the produced hydrogen mixture. The total amount of produced hydrogen mixture can be calculated using the equation:

$$Q_{hydrogen-mixture} = 2\,Q_{CH4}X_{CH4} + Q_{CH4}(1 - X_{CH4}) + Q_{nitrogen}$$

Where Q_{CH4} and $Q_{nitrogen}$ together are the inflow natural gas flow, equalling daily 6 million Nm^3 or 4.6 million Nm^3 when 90% of the nitrogen is removed through a pressure swing adsorption (PSA) process before being processed in the reactor units. X_{CH4} is the conversion rate related to the reactor units setup of the flow design. The resulting hydrogen flow, which is transported to shore, will vary depending on the flow design, with the exception of Flow Design-3, which includes a PSA process for hydrogen purification.

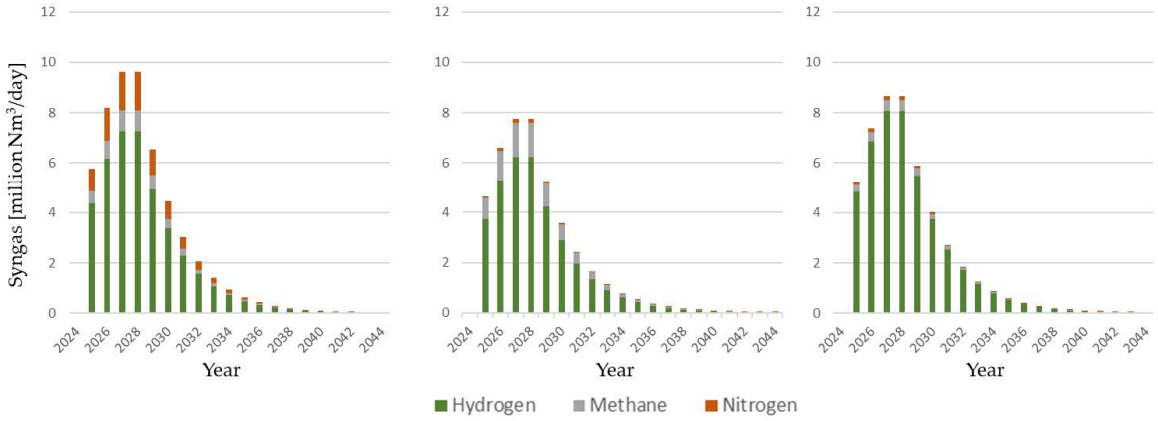

***Figure 4.3**: Initial daily produced hydrogen mixture production over project lifetime (a) Flow Design-1, (b) Flow Design-2, (c) Flow Design-2+ and 3*

Recycling

The implementation of Flow Design-3 for offshore hydrogen purification allows for the recycling of the waste stream, which includes hydrogen, methane, and nitrogen. To accommodate for this increased capability, the size of the installations have been augmented by 15%. As a result, the offshore facility is able to completely convert all methane into hydrogen and the flow of hydrogen is maximally enhanced. The daily flow of hydrogen is illustrated in Figure 4.4, already in kg, as this is the unit for energy value of hydrogen in the LCOH.

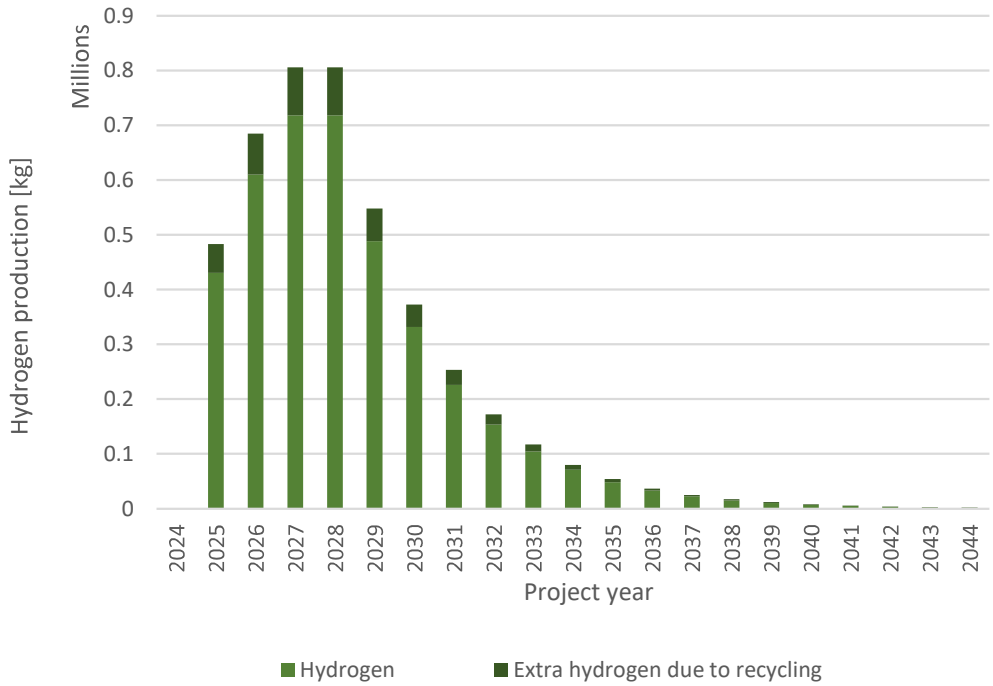

Figure 4.4: *offshore hydrogen production from PSA for Flow Design-3*

4.3.3 Total hydrogen production

The total production in million kg H_2 for the different flow designs is presented in Table 4.12, to summarize Section 4.3. The data is derived from the combination of natural gas production, conversion rate, and potential recycling processes. Next to the absolute production, also the discounted production with a discount rate r=10% for each flow design is showed.

Table 4.12: *Hydrogen production by different flow designs, both absolute and discounted with a discount rate r=10%*

		Production [million kg H_2]
Flow design	1	1,266
Discounted		861
Flow design	2	1,058
Discounted		717
Flow design	2+	1,428
Discounted cost		971
Flow design	3 [a]	1,558
Discounted cost		1,060

[a] Including recycling

It can be determined that the variation in conversion rate among the various flow designs is the primary factor in determining the hydrogen production. Since the daily natural gas production and operational days in a year are the same. Analysis reveals that Flow Design-2, with a conversion rate of 66.6%, exhibits the lowest production. This is followed by Flow Design-1, which has a conversion rate of 81.1%. The highest efficiency is displayed by flow designs 2+ and 3, which both have a conversion rate of 91.4%. It should be noted that Flow Design-3 includes an additional recycling step, resulting in an increased relative natural gas inflow. As the conversion rate for Flow Designs 2+ and 3 is identical, the difference in efficiency can be attributed to the recycling process. Over the project lifetime, this results in an additional 130 million kg of hydrogen production.

4.4 Levelized cost of hydrogen

Since all components of the levelized cost of hydrogen (LCOH) are determined, subsequently the LCOH for the entire project can be calculated. By comparing these designs, the best-performing flow design in terms of LCOH can be identified. Additionally, the build-up and the effect of various modifications on the LCOH for the best performing flow design are quantified. The study was extended to reforming technologies in the same conditions and by comparing the technologies with methane pyrolysis. This way the solution space was established. This analysis is a crucial step in evaluating the potential of methane pyrolysis as an alternative method for hydrogen production and answering the research question.

4.4.1 Best performing flow design

The table provided below shows the LCOH for all flow designs in the analysis, with the variation between the low, base and high scenario visualized in the three columns with results.

Table 4.13: *levelized cost of hydrogen overview for the various flow designs and scenarios. Both the cost and production are discounted with r=10% to include the value of time.*

		Low [€/kg]	Base [€/kg]	High [€/kg]
Flow design	1	1.74	2.43	3.25
Flow design	2	2.03	2.79	3.70
Flow design	2+	1.76	2.45	3.31
Flow design	3 [a]	1.85	2.56	3.46

[a] Including recycling

According to the data presented in the table, it can be observed that the low investment and production approach adopted by Flow Design-2 does not result in a low LCOH. In fact, it is the most expensive flow design among the options presented. On the other hand, the limited offshore installations in Flow Design-1 proves to be a cost-effective strategy, as it has the lowest LCOH among all the flow designs.

When comparing the low, base and high cost scenarios, it can be noted that there is a percentage range of -0.28% to +34% for Flow Design-1. A similar percentage range can also be observed for the other flow designs, indicating that the cost variations across the different scenarios are consistent across all the designs.

Since Flow Design-1 exhibits the most favourable cost-performance characteristics, it will serve as the primary focus for the remaining part of the LCOH analysis.

4.4.2 Levelized cost build-up

A waterfall chart is a useful tool for visualizing the breakdown of costs associated with the production of hydrogen in a specific flow design. It displays the different components as bars, with the height indicating the LCOH of the component, that together sum to the total LCOH. The use of a waterfall chart in LCOH analysis is particularly useful as it allows for the identification of the primary cost drivers, highlighting which components contribute a significant portion of the total LCOH. Additionally, the chart includes subtotals for both capital expenditure (CAPEX) and operating expenditure (OPEX), providing a clear understanding of the ratio between these two major cost components.

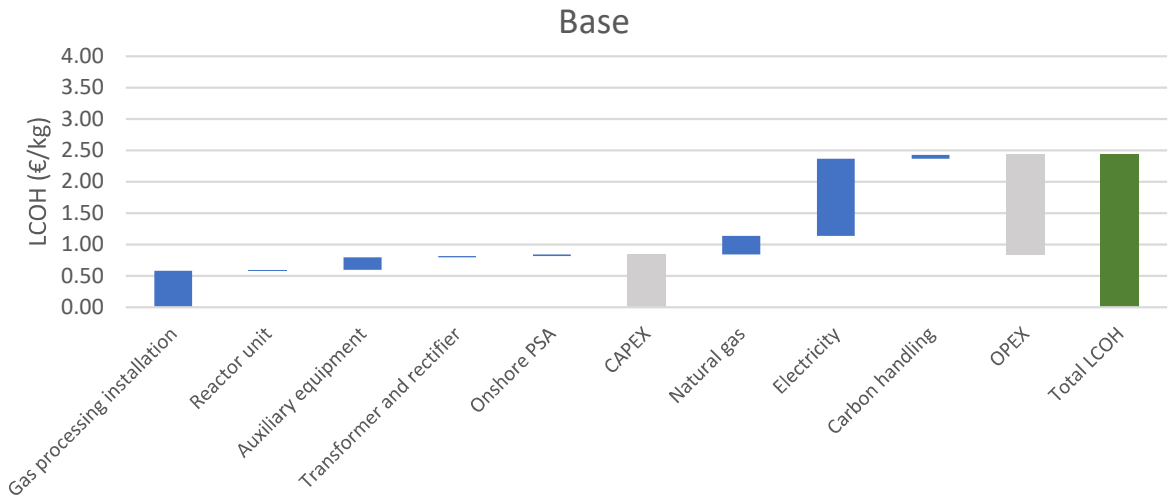

Figure 4.5: *Waterfall chart for base scenario of Flow Design-1, as graphical representation of incremental contributions of different cost.*

Analysing the waterfall chart it can be observed that electricity and gas processing are among the most substantial contributors to the total LCOH. Specifically due to heating and the auxiliary electricity consumption, the electricity OPEX account for 1.23 €/kg of the 2.43 €/kg and the gas production and processing for 0.58 €/kg. The waterfall charts for low and high, and the background data for the three scenarios can be found in Appendix A6.5, complemented with the same charts and data for the other flow designs.

4.4.3 Effect of scenarios and conditions

The tornado chart illustrates the consequences of the low, base, and high scenarios. It is no surprising that the range for the larger contributors exhibits a greater span than the smaller components, as the uncertainties are multiplied with a larger portion of the levelized cost of hydrogen. The impact on LCOH variations for specific installations associated with methane pyrolysis, such as reactor units, transformer and rectifier, and carbon handling, is limited. The deck space and the carbon separation installations are gathered in the auxiliary equipment.

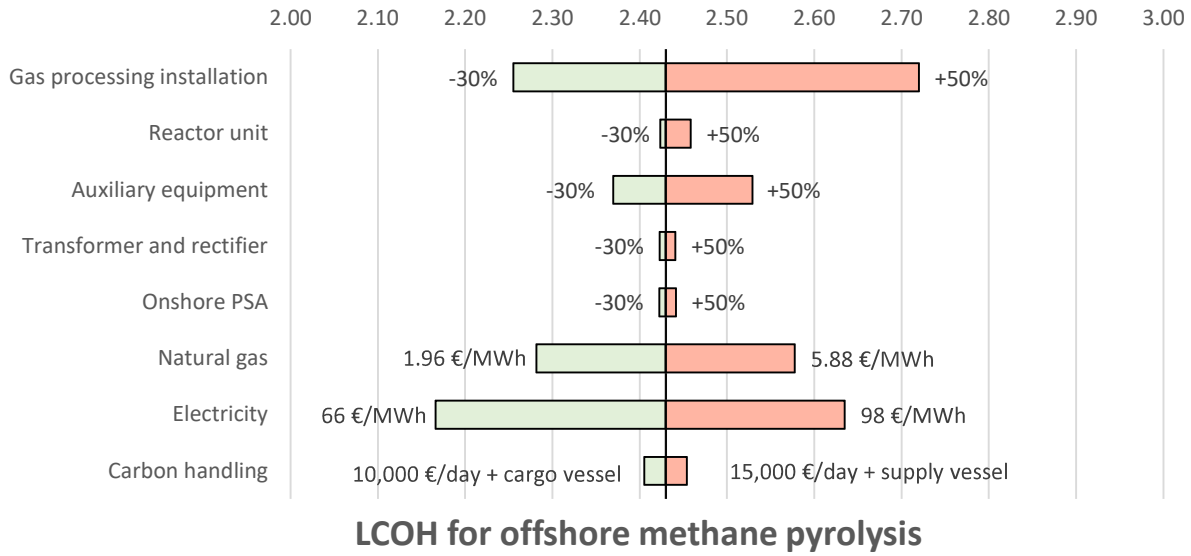

***Figure 4.6**: Tornado chart to show sensitivity of different aspects of methane pyrolysis for Flow Design-1*

WACC variations

The LCOH analysis has been executed with a discount rate r=10%, based on the WACC of hydrogen projects, and also oil and gas projects (Emanuele et al., 2020). However, for other renewable energy projects, commonly a lower discount rate is utilized. As the discount rate decreases, the present value of the future cash flows increases, the LCOH will therefore also decrease.

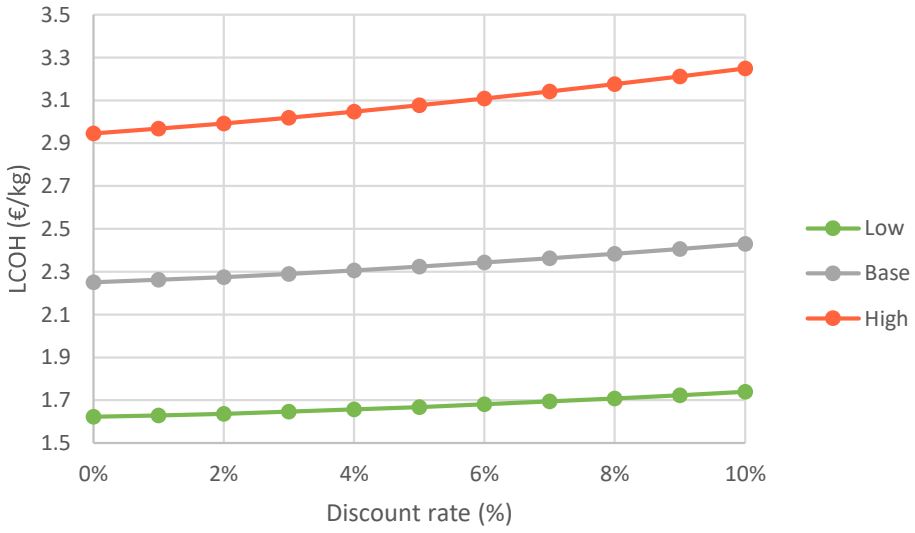

***Figure 4.7:** Effect of varying discount rate on the LCOH of Flow Design-1*

The reduction in the levelized cost of hydrogen (LCOH) is limited when the discount rate is decreased. For instance, in the high scenario with the greatest discrepancy, the LCOH decreases by only 8.6% when the discount rate is set to 2% instead of 10%. This is in contrast with other potential hydrogen production technologies with a LCOH that arises much more from CAEPX. For instance solar PV, where the LCOH can decrease by over 60% for the same adjustment to the discount rate (Coppitters et al., 2019). This is due to the fact that a significant proportion of the LCOH for methane pyrolysis originates from operating expenses (OPEX), which increases when the discount rate is decreased. Therefore, the substantial increase in hydrogen gets partly offset due to the increase in OPEX when the discount rate is reduced. Whereas, the LCOH of solar PV primarily depends on the capital expenses, it is more responsive to adjustments in the discount rate.

Other conditions

A couple interesting conditions are brought forward, to test the LCOH in different situations. They will be discussed and eventually summarized in a table containing the low, medium high LCOH for Flow Design-1.

As discussed in Subsection 4.3.2, the methane conversion can be optimized for the project lifetime by adjusting the operating pressure in reactor, and therefore entire system. This results in much higher conversion ratios outside the peak production project time.

Despite the presence of a significant quantity of nitrogen in the waste stream produced by the pressure swing adsorption process, it is still possible to monetize this gas by selling it based on its heating value. To keep the gas price and the LCOH separate, the remaining heating value is subtracted from the gas stream. As a result, the OPEX associated with natural gas will decrease, as these expenses are also calculated based on the heating value of the gas flow injected into the methanol pyrolysis reactor unit

Presently, it is assumed that ONE-Dyas operates both the gas production and processing operations, as well as the offshore methane facility. However, it would be intriguing to examine the effect on the Levelized Cost of Hydrogen (LCOH) if the offshore methane pyrolysis facility were to be a separate project, distinct from the gas production and processing operations. In order to assess the impact on the LCOH, the CAPEX and OPEX for gas production and processing are excluded from the analysis and a range for the market price for natural gas is incorporated into the model as the OPEX for natural gas. The range is set at 15 to 35 €/ MWh (Prognos, 2022).

Initially the system efficiency has been set to 58% according to (Sánchez-Bastardo et al., 2020) what determined the electricity demand per kg of H_2 to 9 MWh. Towever this efficiency was for an onshore facility and arguably offshore facility would have more difficulty reaching this efficiency. The LCOH is therefore also determined for a reduced efficiency of 50%.

The model from Chapter 2 and the design phase in Chapter 3, could have resulted in an overestimation of the methane conversion rate possible within he utilized designs for the Flow Designs. The effect of a 5% reduction is tested, to determine the effect of an actual reduced conversion rate on the LCOH of offshore methane pyrolysis. Table 4.15 on next page.

Table 4.14: *Effect of varying conditions on the LCOH of Flow Design-1. In the last column the difference is indicated with a – for a reduction in LCOH (advantageous) and a + for an increase in LCOH (disadvantageous)*

	Low [€/kg]	Base [€/kg]	High [€/kg]	Base difference [Δ€/kg]
Lifetime pressure adjustment	1.68	2.34	3.12	- 0.09
Sell remaining gas	1.71	2.37	3.17	- 0.06
Separate natural gas project	2.23	3.33	4.45	+ 0.90
50% system efficiency	1.83	2.55	3.39	+ 0.12
5% lower conversion rate	1.81	2.54	3.40	+ 0.11

4.4.4 Conventional hydrogen production levelized cost of hydrogen

In order to gain a more comprehensive understanding of the value of the LCOH, a comparison with conventional large-scale hydrogen technologies is conducted. Steam methane reforming (SMR) and autothermal reforming (ATR) are both considered, with and without carbon, capture and storage (CCS). To ensure a fair comparison, the electricity price in both LCOH should be the same. The natural gas price for the LCOH of SMR or ATR was based on the market price of gas. And last, the CO_2, which is really important as it amplifies the benefit of adding CCS to the technology. To give an idea of the LCOH range for the conventional technologies the LCOH is calculated with an electricity price of 84 €/MWh and gas price of 25 €/MWh. The LCOH for both a scenario with and without CO_2 tax will be listed, to indicate the mitigating effect of CCS on the increase in LCOH.

Table 4.15: *levelized cost of hydrogen for the conventional hydrogen production technologies SMR and ATR including and excluding carbon capture and storage (CCS)*

	Price [a]	SMR [€/kg]	SMR+CCS [€/kg]	ATR [€/kg]	ATR+CCS [€/kg]
Natural gas [b]	25 €/MWh	1.25	1.53	1.04	1.04
Electricity	84 €/MWh	0.08	0.11	0.20	0.30
CO_2 Tax [c]	81 €/mt $CO_{2eq.}$	0.92	0.66	0.89	0.32
Total LCOH excl. CO_2 tax		1.33	1.64	1.24	1.34
Total LCOH		**2.25**	**2.30**	**2.13**	**1.66**

[a] All information on technologies from (Oni et al., 2022), more background on the rate per component and technology can be found in Appendix A6.6

[b] Estmiated natural gas price in 2030 (Prognos, 2022)

[c] Assumed average CO_2 price based on data from Statista (Tiseo, 2022)

Initially, the addition of CCS is less profitable when no CO_2 tax is in place. However, when the CO_2 tax increases CCS becomes more attractive, especially for ATR as CCS can achieve a higher capture rate. It would prevent more CO_2 emissions and therefore most CO_2 tax. Already from 15 €/mt CO_{2eq}, ATR+CCS is cost competitive with an electricity price of 84 €/MWh and gas price of 25 €/MWh. For SMR the application of CCS is less interesting from an economical perspective, as for the same conditions, the CO_2 tax should increase to 100 €/mt CO_{2eq} to make SMR+CCS less expensive than standard SMR. Since ATR and with an increasing CO_2 tax

ATR+CCS, have the lowest LCOH these will be the in main technologies to compare the LCOH of offshore methane pyrolysis with.

4.5 Results and discussion

A sensitivity analysis is a method in the field of energy economics that allows for the examination of how variations in cost components affect the total. In the context of comparing the levelized cost of hydrogen from different technologies, a sensitivity analysis can be employed to determine the primary drivers that in the end bring offshore methane pyrolysis and reforming technologies closer together to gain an understanding of the comparative performance of different technologies under varying conditions.

The identified cost components that will be varied are: gas price, electricity price, CO_2 tax, carbon product value and CAPEX. The range of each component will be discussed to finally show the results of the most beneficial case in a sensitivity plot.

Gas price

The gas price is an important driver for the LCOH of ATR and ATR+CCS, as the natural gas is not only as feedstock but also used as fuel for the installation. It does not influence the LCOH of offshore methane pyrolysis, as this is determined according to the technical cost of production and determined by ONE-Dyas as operator of the N05-A gas field. A high gas price, would therefore push the LCOH of ATR and ATR+CCS upwards towards offshore methane pyrolysis. The range for gas price is set from 15 to 35 €/MWh , in line with the cost analysis on electricity and gas from Prognos (2022).

Electricity price

The effect of electricity is the opposite of gas, since the offshore methane pyrolysis installation is heated with electricity. The demand for electricity is high for offshore methane pyrolysis and a low electricity price would reduce the LCOH more than for ATR and ATR+CCS. The range for electricity is set from 66 to 98 €/MWh.

The current range for electricity price is based on the marketprice, however it would be interesting to test what a pure supply of renewable electricity would do with the sensitivity analysis, to see what would be the potential when all electricity comes from surrounding offshore wind. Therefore, the sensitivity analysis is also executed for the levelized cost of electricity of offshore wind by 2030, 50 €/MWh (DNV, 2021).

CO_2 tax

The key capability of offshore methane pyrolysis is that the carbon is pre-combustion captured by turning it into solid carbon. This results in a possible sellable product and direct CO_2 emissions are prevented. A CO_2 tax on emissions would therefore be very beneficial for the business case of methane pyrolysis as it would not be effect, but the ATR directly and the ATR+CCS in limited fashion. The necessary CO_2 tax to make offshore methane pyrolysis cost competitive with ATR and afterwards ATR+CCS is first determined. However, the price is expected not to rise much further than 100 €/mt CO_2.

Carbon product value

In the current calculation for LCOH for offshore methane pyrolysis, the carbon product is transferred for no cost to a process facility, that could generate revenue after purifying the material. However possible a fee could be charged, or the product could be purified by ONE-Dyas. The carbon product value is therefore included on top of the maximum CO_2 tax, to meet the LCOH of offshore methane pyrolysis.

CAPEX

To include all cost components of the offshore methane pyrolysis design, the uncertainty in CAPEX as a total has been included. The effect of a 30% CAPEX reduction has been taken into account as example, to show the reduction in necessary carbon product value.

4.5.1 final solution space

Since the LCOH for the conventional technologies is given for discount rate r=0%, the same discount rate is applied to offshore methane pyrolysis to make a far comparison possible. The study found that within the range of initial gas and electricity prices, the optimal scenario is characterized by high gas prices and low electricity prices, as the LCOH of methane pyrolysis is the closest to ATR and ATR+CCS. When a 33 €/mt CO_2 carbon tax would be in place the LCOH of ATR would increase to 1.72, equalling the LCOH of offshore methane pyrolysis. For ATR+CCS this should be 69 €/mt CO_2. Alternatively, the carbon product value alone could reduce the LCOH to match that of ATR and ATR+CCS. In this case, ATR would be less expensive, therefore, a carbon product value of 91 €/mt C_s would be necessary for ATR+CCS and 121 €/mt C_s for standard ATR. The two could also be becomes, for instance a combination of 50€/mt CO_2 and 29 €/mt C_s would make offshore methane pyrolysis cost competitive. A reduction in CAPEX would bring the LCOH closer together and therefore reduce the necessary CO_2 tax and carbon product value. With a 70% reduction the necessary carbon product value would drop to 64 €/mt C_s. The results are illustrated in the sensitivity plot in Figure 4.8. The data tables and sensitivity plots of the other scenarios can be found in Appendix A6.7.

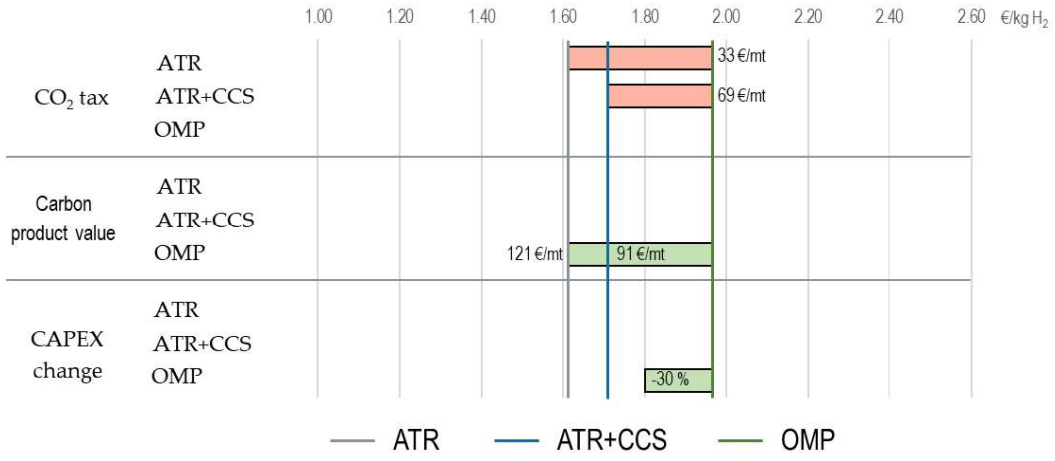

Figure 4.8: *Sensitivity plot for a LCOH comparison between ATR, ATR+CCS and offshore methane pyrolysis with a 35 €/MWh gas price and 66 €/MWh electricity price*

Extending the range for electricity to an electricity price based on offshore wind for the entire project lifetime (50 €/MWh), would further reduce the difference. Already from a 13 €/mt CO_2 carbon tax, ATR become more expensive and the same occurred for ATR+CCS from 21 €/mt CO_2. The gap in LCOH could also be closed with the carbon product value. From 28 €/mt C_s, offshore methane pyrolysis was cost-competitive with ATR+CCS and for 48 €/mt C_s this was the case for ATR. At last the influence of a reduction in CAPEX has been considered. This reduces the LCOH from 1.72 to 1.64 €/kg H_2. Hence, the necessary carbon product value dropped to only 20 €/mt C_s to be completely cost-competitive.

4.5.2 Interpretation

With the uncertainties from modelling in Chapter 2 and the offshore design in Chapter 3 in mind, the effect on the cost should be defined to interpretate the results and possible variation on the final LCOH.

To largest components of the LCOH for offshore methane pyrolysis are the natural gas production and processing CAPEX, the natural gas OPEX and the electricity OPEX. The variation in reactor unit size and related deck space would therefore be relative small, even when extending these size effects on the carbon separation and handling station. The reactor unit design, in combination with the direct related equipment has assumed a heat efficiency of 58% what results in a electricity demand of 9 MWh/mt H_2. The precise efficiency of the design is however unsure. The effect of a reduced efficiency to 50% was tested in the economic model and only increased the LCOH for the base scenario for Flow Design-1 with 0.12 €/kg H_2, and was therefore manageable.

Next, to the physical aspects of the design, the performance could also differ. Various things in the end result in the maximum methane conversion at the top of the reactor units within the four Flow Designs. Examples are the achievable heating temperature of the coil heating elements or the methane conversion when gas holdup would actually differ 30% in gas holdup from the correlation. The effect of a various in conversion rate was therefore tested. The possibilities for a larger conversion rate are limited, due to the near equilibrium conditions within the operating pressure and temperature, therefore, a large reduction in LCOH is not foreseen. When the methane conversion would be 5% lower than expected, the LCOH would increase from 2.43 to 2.55 €/kg H_2 for the base scenario for Flow Design-1.

The most significant source of uncertainty in the calculation of the LCOH is related to the carbon by-product of the methane pyrolysis process. The carbon product could be a project enable depending on the quality but large salt contamination in the outgoing carbon product could result in the oppositive. Currently, the efficiency of the carbon separation and handling station is assumed to be so high, due to a large recycling stream of salt into the reactor, only a minor percentage of salt is present in the carbon product when shipped to shore. However, when this efficiency would decrease, a large outgoing flow of salt from the platform arises. This is disadvantageous in two ways, an additional inflow of salt to the platform should be created to guarantee reactor performance and the product value of the shipping carbon decreases. This uncertainty is a limitation of the current research and therefore more research should be necessary to define the precise possibilities for continuous separation and salt recycling. On the other side, the carbon product value could decrease the LCOH significantly as seen in Subsection 4.4.5, depending on the product and quality. Possible, products from molten metal reactors includes carbon black, which can range in sales price from $500 to $1500

per metric ton depending on quality (Made-in-China, 2023). Additionally, market perspective also plays a role in determining the value of the carbon product. While a singular facility may use market prices in their calculations, the deployment of methane pyrolysis on a global scale could significantly decrease the price due to increased production. It is important to realise that the carbon product value is market price buyers are willing to pay for the carbon product. All the previous mentioned factors should therefore be considered.

4.5.3 Validate results

Since previous research specifically on offshore methane pyrolysis does not exist, the sensitivity analysis on the LCOH was compared to onshore methane pyrolysis. TNO executed a sensitivity analysis on methane pyrolysis, including steam methane reforming (SMR) and Polymer electrolyte membrane electrolysis (PEM). As the latter as not been discussed in this report it will be not be considered for the moment. To make a comparison possible, the same base case values should be implemented. The important values, that are also represented in the economic model for offshore methane pyrolysis are: 50 €/MWh, gas price of 21.6 €/MWh, CO_2 tax and carbon credit of 25.96 €/mt and no initial carbon product value has been taken into account. Also the discount rate was set to r=0%. Their sensitivity analysis is represented in Figure 4.9.

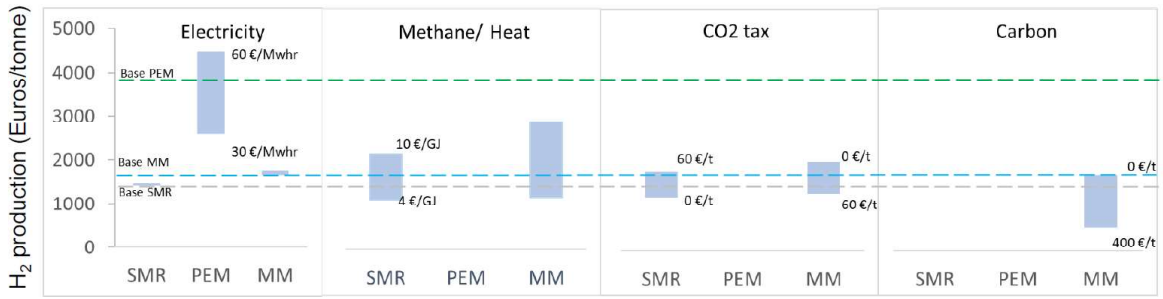

Figure 4.9: Sensitivity analysis from TNO on the cost competitiveness of onshore methane pyrolysis (Bhardwaj et al., 2021)

To determine the LCOH of offshore hydrogen in the same conditions, the impact of natural gas should be into account. Therefore, from Subsection 4.4.3, the situation with a separate operator has been taken with a electricity price of 50 €/MWh. Only the carbon credits are not considered as revenue. It resulted in a LCOH 3.05 €/kg H_2. When the LCOH without carbon credits, is considered this is around 1.90 €/ kg H_2. Resulting in a cost ratio between offshore and onshore of 1.6. This is a plausible ratio for cost between offshore and onshore installations. Taken into account the cost calculation for SMR in Subsection 4.4.4, the cost was 1.42 €/ kg H_2. Both figures fit nicely in Figure 4.9.

In the sensitivity analysis onshore methane pyrolysis needed much more carbon product value and less CO_2 tax to become cost competitive with SMR, than offshore methane pyrolysis with ATR+CCS. This is due to a couple of reasons. Firstly the LCOH for the offshore installation in this research is low, 1.72 €/ kg H_2 for the same electricity price. This is due to the fact that the natural gas OPEX is based on the technical cost of gas production and processing instead of the market price, reducing the LCOH. Secondly the onshore methane pyrolysis is compared to SMR and in this research offshore is compared to ATR. Since ATR emits less CO_2 than SMR, especially in combination with CCS, the influence of a CO_2 tax is

much larger in the sensitivity analysis from Figure 4.9 than in this research. On top of this, also carbon credits are allocated with an equal value to the CO_2 tax doubling the effect of the CO_2 tax.

Since the identified differences are explainable, overall, the LCOH of offshore methane pyrolysis fits in well with the sensitivity analysis of figure X.

4.5.4 Limitations

The final LCOH for offshore methane pyrolysis has been based on a multitude of assumptions, to shed some light on the limitations that flow forward from these assumptions the most important are discussed in this section.

Price of auxiliary equipment

By assuming the complexity of the auxiliary equipment had comparable complexity to the equipment on the N05-A platform for gas production and processing, the CAPEX for auxiliary equipment could be determined. This was done to prevent a cost analysis for every installation in the chain. However, for a precise determination of the CAPEX it would be necessary to access all installation separate. The uncertainty is the largest for the carbon separation and handling station, as the process inside the installation is defined but not the specific machinery.

Production profile

The offshore methane pyrolysis installation was directly connected to the gas production and processing and therefore followed the gas production profile. This research was limited to a single gas production profile. However, possibly a different profile would benefit the feasibility and LCOH of offshore methane pyrolysis. Even though the net present value of the production flow would reduce, the installation could be downsized by spreading out the production flow over the lifetime of the project.

The methane pyrolysis could also have been designed to process a part of the natural gas flow. In this scenario the installation could be downscaled, and operates at the methane pyrolysis maximum capacity for a longer amount of time while keeping the production profile in place that maximize the net present value of the natural gas in the field.

Actual natural gas composition

To ease the analysis, the natural gas has been assumed to consist of 74.7 mol% CH_4 and 25.3 mol% N_2 however when taking into account the substances in the natural gas. The problem becomes more difficult.

Even though, the present of CO_2 is small. The assumption that is was lumped into N_2 does lead to CO_2 emissions when rejecting the nitrogen from the natural gas stream and venting the PSA waste stream. For Flow Design-2, Flow Design-2+ and Flow Design-3, arguably an additional pipeline should be in place to get N_2 + CO_2 mixture to shore when a completely CO_2 perspective is the aim of these designs.

Also the condensate with higher hydrocarbons can be processed by a methane pyrolysis, this is not been examined for the other installations. In the original design, the condensate is added

to the natural gas and transported to shore in the NGT. However it would be undesirable to mix the condensate with high purity hydrogen, therefore, in that scenario also a smaller pipeline to shore would be necessary.

Influence of weather on transport

The transport of carbon has been assumed to continue day and night, every day a week except for the 5% a year (unexpected) maintenance takes place. The effect of weather conditions on the transport is therefore not included. Extreme waves and wind would especially prevent transport with the offshore supply vessels, as they have to transport multiple time a day. The methane pyrolysis operations should be stopped in this case. With the cargo vessel, transport could be scheduled around heavy weather as the number of trips are more moderate, however when loading at the platform would be impossible due to the weather operations have to stop for both ships. This could be a major limitation for offshore methane pyrolysis when the off day become abundant. It hard to believe that turning the installation on and off continuously would be beneficial for the OPEX so not only the technical feasibility would be effected also the LCOH.

Gas and electricity price variations

Even though the low electricity price and high gas price would result in the most beneficial LCOH, this scenario is debatable due to the dependence on gas for the production of electricity (De Boer & Stet, 2022). Since natural gas is the last source for electricity, the overall electricity price would be determined by the electricity price of gas fired power plants, when electricity demand exceeds the production by all other technologies (solar and wind, hydrogen, nuclear, etc.).

5 Conclusions

Hydrogen production offshore from natural gas could give significant benefits as the current pipeline infrastructure could be utilized for hydrogen transport and it would provide offtakes with a large supply immediately. Where conventional reforming technologies do produce gaseous CO_2 in the process, the new emerging technology methane pyrolysis would provide the necessary hydrogen without gaseous CO_2. The carbon from methane would be converted into solid carbon. The potential of methane pyrolysis to produce offshore hydrogen was therefore investigated to answer the following research question in this thesis:

"Define the solution space that represents cost-competitive offshore methane pyrolysis in the Netherlands and what challenges methane pyrolysis should overcome?"

A model has been used to determine the conversion rate of an installation depending on the properties of the molten metal reactor. However, this model did not include the initial small bubbles that occur at the bottom of a reactor due to injection of natural gas through the small pores. The model was extended to include this behaviour as these small bubbles create a large reaction surface which results in important early conversion at the bottom of the reactor. This behaviour has been replicated in the model. Additionally, the model had been assessed for molten salt as it was intended for metal. The model did indicate that the conversion in the salt layer was extremely limited but due to jumps in the modelled gas percentage, the model did not apply to salt as reactor fill. Therefore, the molten metal and salt reactor was dimensioned by applying the model over the metal fill and assuming the conversion did not varied in the salt layer any more.

With the model as tool, an offshore design could be made to access the technical feasibility of deploying methane pyrolysis. The N05-A platform from ONE-Dyas was utilized as case which let to multiple limitations. The deck was designed for a maximum load of 3.5 mt/m^2. On the platform 150 m^2 deck space was available with a height limitation of 5.2 m. Next, the requirements of the hydrogen were defined for two scenarios. In the first scenario, the outgoing gas had to meet the hydrogen mol% of steam methane reforming. In the second scenario, the outgoing gas had to meet the hydrogen purity of the hydrogen backbone. The limitations let to a design that maximized the number of short columns on a surface to evenly distribute the weight of the reactors and use the high conversion rates at the bottom of a methane pyrolysis reactor in the model. These columns were combined in a reactor unit on 5m x 4m deck space. To convert the flow of natural gas, the reactor unit also needed multiple auxiliary installations. The auxiliary installations depended on the scenario but demanded significant deck space.

Methane pyrolysis on the available 150 m2 at offshore methane pyrolysis would only be able to process 0.39 million Nm3, which is a minor part of the peak production of 6 million Nm^3. However, to meet the hydrogen requirements of one of the two scenarios, it is necessary to allocate additional deck space. The size of this additional area is contingent upon the requirements for the pipeline used in transporting hydrogen. The size can range from being

equivalent to the size of a single platform for a hydrogen mxiture flow with a similar hydrogen composition to that of steam methane reforming, to 2.5 times the deck space of a platform for producing hydrogen with a high hydrogen backbone quality. This is in addition to the 150 square meters of deck space at the N05-A platform that is currently available.

With the minimum necessary deck space defined, the levelized cost of hydrogen (LCOH) for the entire offshore methane pyrolysis facility could be defined. The LCOH (€/kg) is determined by dividing the capital and operational expenditure related to the gas production and processing, the reactor units and the auxiliary equipment by the production of hydrogen. The design with the lowest base LCOH could produce hydrogen at 2.25 €/kg, and 2.43 €/kg when a discount rate of 10% was taken into account. A comparison with conventional technologies for producing hydrogen showed that a CO_2 and the carbon product value would be enablers of a cost-competitive offshore methane pyrolysis installation. With CO_2 tax of 69 €/mt CO_2 or carbon product value 121 €/mt C_s levels the LCOH of offshore methane pyrolysis with ATR and ATR+CCS. Between these two values a large space exist that combines the two, an example would be 50€/mt CO_2 and 29 €/mt C_s.

For offshore methane pyrolysis to become a cost competitive production technology for hydrogen the LCOH should be reduced. The most promising solutions for achieving this are sales of the carbon product and a governmental induced CO_2 tax on emissions.

6 Recommendations

The recommendations are separated into three sections for clarity: methane pyrolysis model, reactor design and economic model. They address considerations for further research on all sections.

Methane pyrolysis model

The transition zone is included in the model based on data obtained in a different medium than the molten metal applied in this research. Experimental testing of the height and behaviour in the transition zone in the conditions of the model would be an applicable method to validate and improve this part of the model. Ideally, a new correlation for the Sauter diameter is developed and added to the model that works both in the transition zone and the rest of the reactor depending on the gas inflow and the properties of the reactor. This would not only improve the description of the bubble size and reaction surface in the transition zone, but also other properties related to the bubble size such as the bubble velocity in the tank could be defined.

The applicability of the model at the moment limited by the experimental ranges corresponding to the various correlation in the model. New experimental research to define the correlations outside these ranges would benefit the applicability of the model. Especially for the range for Froude number, as this is currently the most limiting parameter in the model. Validating the behaviour of the correlation for d_{vs} beyond the current $N_{fr} = 0.135$ limit, would make the model applicable to more conditions.

The model was validated for molten salt, however, the results for especially the gas holdup did not align. Therefore, a better representation for the gas holdup that would work in both molten metal and molten salt would make it possible to analyse the molten metal and salt reactor with a single model.

Reactor design

One of the largest uncertainties was the continuous separation and handling of the carbon product. A real-life pilot with a continuous installation that would remove the carbon from the top of the molten medium and improves the quality of the carbon product would provide valuable information to narrow the uncertainties. It should prove the effectiveness of continuous separation of carbon and salt and what percentage of salt should be resupplied.

This research has focussed on the technical side of the designing an offshore methane pyrolysis facility, however the safety measures and a maintenance strategy have not been thoroughly investigated. Future research could focus on a safety and maintenance plan that would make safe and continuous offshore methane pyrolysis possible in an extension to the finding of this report.

Heating with electricity creates a dependence on an electricity supply. Therefore, it would be interesting to look at the technical feasibility of heating with hydrogen in the current design. It would offer flexibility regarding the offshore location and make the project independent on a supplier. Additionally, hydrogen burners could reduce the LCOH as burning produced hydrogen could be economically more attractive than buying electricity.

Economic model

Carbon black sales could be a project enabler for methane pyrolysis. However, with a world scale application of methane pyrolysis the supply of carbon would exceed the current demand for it. A market research to identify new sectors and possible prices, depending on the quality, would narrow down and possible reduce the LCOH for methane pyrolysis when a reasonable sales price for large scale production can be established.

7 Bibliography

Aberdeen Business News. (2022). North Sea pipelines Nogat and Noordgastransport are first to receive Certificate of Fitness to transport hydrogen at sea. *North Sea News*. Retrieved 6 October, from https://aberdeenbusinessnews.co.uk/north-sea-pipelines-nogat-and-noordgastransport-are-first-to-receive-certificate-of-fitness-to-transport-hydrogen-at-sea/

Akita, K., & Yoshida, F. (1973). Gas holdup and volumetric mass transfer coefficient in bubble columns. Effects of liquid properties. *Industrial & Engineering Chemistry Process Design and Development, 12*(1), 76-80.

Akita, K., & Yoshida, F. (1974). Bubble size, interfacial area, and liquid-phase mass transfer coefficient in bubble columns. *Industrial & Engineering Chemistry Process Design and Development, 13*(1), 84-91.

Ali, F., Khan, M. A., Qurashi, M. A., Shah, S. A. R., Khan, N. M., Khursheed, Z., Rahim, H. S., Arshad, H., Farhan, M., & Waseem, M. (2020). Utilization of pyrolytic carbon black waste for the development of sustainable materials. *Processes, 8*(2), 174 %@ 2227-9717.

Andreini, R., Foster, J., & Callen, R. (1977). Characterization of gas bubbles injected into molten metals under laminar flow conditions. *Metallurgical Transactions B, 8*(4), 625-631.

Antzara, A., Heracleous, E., Bukur, D. B., & Lemonidou, A. A. (2014). Thermodynamic analysis of hydrogen production via chemical looping steam methane reforming coupled with in situ CO2 capture. *Energy Procedia, 63*, 6576-6589.

Argus. (2023). *Bismuth prices*. Argus. Retrieved 14 Januari from https://www.argusmedia.com/metals-platform/metal/minor-and-specialty-metals-bismuth

Ashik, U. P. M., Wan Daud, W. M. A., & Abbas, H. F. (2015). Production of greenhouse gas free hydrogen by thermocatalytic decomposition of methane – A review. *Renewable and Sustainable Energy Reviews, 44*, 221-256.

Asian insulations. (2017). *Ceramic Fibre Paper*. Retrieved 15 November from https://asianinsulations.com/product/ceramic-fibre-paper/

BASF. (2021). *ESG Engagement Meeting with ShareAction* https://www.basf.com/global/documents/en/investor-relations/calendar-and-publications/presentations/2022/220112_BASF-ESG_ShareAction.pdf

Basha, O. M., & Morsi, B. I. (2017). Effects of Sparger and Internals Designs on the Local Hydrodynamics in Slurry Bubble Column Reactors Operating under Typical Fischer-Tropsch Process Conditions - I. *International Journal of Chemical Reactor Engineering, 16*.

Bauto, L. (2022). *Factor of Safety Definition*. SafetyCulture. https://safetyculture.com/topics/factor-of-safety/

Bhardwaj, R., Frens, W., Linders, M., & Goetheer, E. (2019). Ember: Pyrolysis technology for hydrogen and carbon. https://www.ureaknowhow.com/ukh2/images/stories/Partners/wfrens/ember_pyrolyse.pdf

Bhardwaj, R., Koneman, J. W., & Goetheer, E. (2021). Turquoise hydrogen: the potential for combined hydrogen and carbon production via methane cracking. Retrieved March 02, from https://dgmk.de/en/app/uploads/2021/02/Abstract_Goetheer.pdf/

Bielka, P., & Kuczyński, S. (2022). Energy Recovery from Natural Gas Pressure Reduction Stations with the Use of Turboexpanders: Static and Dynamic Simulations. *Energies, 15*(23), 8890.

Burgess, J. (2021). Infrastructure biggest hurdle to hydrogen economy as investments gather pace: DNV.

Business Insider. (2022). *Nickel price today*. Retrieved 24 Novmber 2022 from https://markets.businessinsider.com/commodities/nickel-price

Business Insider. (2023). *Copper price today*. Business Insider. Retrieved 14 January from https://markets.businessinsider.com/commodities/copper-price

Catalan, L. (2022, 02 June). *Model for Molten Metal and Salt Reactor - Methane Pyrolysis* [Interview].

Catalan, L. J., & Rezaei, E. (2020). Coupled hydrodynamic and kinetic model of liquid metal bubble reactor for hydrogen production by noncatalytic thermal decomposition of methane. *International Journal of Hydrogen Energy, 45*(4), 2486-2503.

Catalan, L. J., & Rezaei, E. (2022). Modelling the hydrodynamics and kinetics of methane decomposition in catalytic liquid metal bubble reactors for hydrogen production. *International Journal of Hydrogen Energy, 47*(12), 7547-7568.

Chou, M.-S., Hei, C.-M., & Huang, Y.-W. (2007). Regenerative thermal oxidation of airborne N, N-dimethylformamide and its associated nitrogen oxides formation characteristics. *Journal of the Air & Waste Management Association, 57*(8), 991-999.

Coppitters, D., De Paepe, W., & Contino, F. (2019). Surrogate-assisted robust design optimization and global sensitivity analysis of a directly coupled photovoltaic-electrolyzer system under techno-economic uncertainty. *Applied energy, 248*, 310-320.

Daily metal prices. (2023). https://www.dailymetalprice.com/metalprices.php?c=ni&u=lb&d=20

Daliah, R. (2021). *Technology landscape: Key players in methane pyrolysis*.

Data common. (2019). *CO2 emissions per capita Netherlands*. Retrieved 9 January from https://datacommons.org/tools/timeline#&place=country/NLD&statsVar=Amount_Emissions_CarbonDioxide_PerCapita

De Boer, S., & Stet, C. (2022). *The Basics of Electricity Price Formation*. https://www.rabobank.com/knowledge/d011318792-the-basics-of-electricity-price-formation

DNV. (2021). *Wind energy – going offshore*. Retrieved 14 January from https://www.dnv.com/to2030/technology/wind-energy-going-offshore.html

Emanuele, T., Herib, B., & Raul, M. (2020). Green hydrogen cost reduction. *Abu Dhabi: International Renewable Energy Agency*.

Energy Transition Commission. (2018). *Mission Possible: Reaching net-zero carbon emissions from harder-to-abate sectors*. https://www.energy-transitions.org/publications/mission-possible/

Engineering Toolbox. (2005). *Stress in Thick-Walled Cylinders or Tubes*. https://www.engineeringtoolbox.com/stress-thick-walled-tube-d_949.html

Engineering ToolBox. (2014). *Circles within a Rectangle - Calculator*. Retrieved 22 September from https://www.engineeringtoolbox.com/circles-within-rectangle-d_1905.html

[Record #145 is using a reference type undefined in this output style.]

Gemhold tranding. (2023). *Industrial grade high purity sodium bromide*. Retrieved 13 January from https://gemhold.en.alibaba.com/search/product?SearchText=sodium%20bromide

Globe metals and mining. (2022). *Niobium*. Retrieved 4 November from https://www.globemm.com/niobium-markets

Goetheer, E. (2022a). *Molten metal and salt reactor design discussion* [Interview].

Goetheer, E. (2022b). *Sparger Plate Discussion* [Interview].

H-Vision. (2019). Blauwe waterstof als versneller en wegbereider van de energietransitie in de industrie.

Handybulk. (2023). *Ship charter rates*. Retrieved 15 January from https://www.handybulk.com/ship-charter-rates/

Hibiki, T., Saito, Y., Mishima, K., Tobita, Y., Konishi, K., & Matsubayashi, M. (2000). Study on flow characteristics in gas-molten metal mixture pool. *Nuclear engineering and design, 196*(2), 233-245.

Hydrogen Council. (2020). Path to hydrogen competitiveness: a cost perspective.

IndexBox. (2022). *Chromium Market Outlook 2022: Rising Energy Costs to Accelerate Price Growth - IndexBox*. GlobeNewswire. Retrieved 24 November from https://www.globenewswire.com/en/news-release/2022/02/24/2390990/0/en/Chromium-Market-Outlook-2022-Rising-Energy-Costs-to-Accelerate-Price-Growth-IndexBox.html

Ishii, M. (1977). *One-dimensional drift-flux model and constitutive equations for relative motion between phases in various two-phase flow regimes*.

Ismail, A. F., Khulbe, K. C., & Matsuura, T. (2015). Gas separation membranes. *Switz. Springer, 10*, 973-978.

Jamialahmadi, M., Zehtaban, M., Müller-Steinhagen, H., Sarrafi, A., & Smith, J. (2001). Study of bubble formation under constant flow conditions. *Chemical Engineering Research and Design, 79*(5), 523-532.

Janz, G. J. (1988). Thermodynamic and transport properties for molten salts: correlation equations for critically evaluated density, surface tension, electrical conductance, and viscosity data. *Journal of Physical and Chemical Reference Data, 17*.

Jones, Z. (2021, June 23). *Co-producing Hydrogen and Valuable Solid Carbon from Natural Gas* [Interview]. SoCalGas.

Kalman, V., Voigt, J., Jordan, C., & Harasek, M. (2022). Hydrogen Purification by Pressure Swing Adsorption: High-Pressure PSA Performance in Recovery from Seasonal Storage. *Sustainability, 14*(21), 14037.

Kang, D., Rahimi, N., Gordon, M. J., Metiu, H., & McFarland, E. W. (2019). Catalytic methane pyrolysis in molten MnCl2-KCl. *Applied Catalysis B: Environmental, 254*, 659-666.

Karlberg, B., & Pacey, G. E. (1989). *Flow injection analysis: a practical guide*. Elsevier.

Kataoka, I., & Ishii, M. (1987). Drift flux model for large diameter pipe and new correlation for pool void fraction. *International Journal of Heat and Mass Transfer, 30*(9), 1927-1939.

Keipi, T., Li, T., Løvås, T., Tolvanen, H., & Konttinen, J. (2017). Methane thermal decomposition in regenerative heat exchanger reactor: Experimental and modeling study. *Energy, 135*, 823-832.

Korányi, T. I., Németh, M., Beck, A., & Horváth, A. (2022). Recent Advances in Methane Pyrolysis: Turquoise Hydrogen with Solid Carbon Production. *Energies, 15*(17), 6342.

Kurmayer, N. (2022). *German electricity grid upgrade 'will be expensive', experts warn*. Retrieved 10 January from https://www.euractiv.com/section/electricity/news/german-electricity-grid-upgrade-will-be-expensive-experts-warn/

Leal Pérez, B. J., Medrano Jiménez, J. A., Bhardwaj, R., Goetheer, E., van Sint Annaland, M., & Gallucci, F. (2020). Methane pyrolysis in a molten gallium bubble column reactor for sustainable hydrogen production: Proof of concept & techno-economic assessment. *International Journal of Hydrogen Energy, 46*(7), 4917-4935.

Liu, Z.-K., Ågren, J., & Hillert, M. (1996). Application of the Le Chatelier principle on gas reactions. *Fluid phase equilibria, 121*(1-2), 167-177.

Made-in-China. (2023). *Carbon Black Granular manufacturers & suppliers*. https://www.made-in-china.com/products-search/hot-china-products/Carbon_Black_Granular.html?acc=8642081837&cpn=15233612281-&tgt=&net=x&dev=c-&gid=CjwKCAiAzp6eBhByEiwA_gGq5NHWdx2TRZgQW9ybhclwtfQvKzNnbPTLrgFsu0YNGFANSfwtQy2KdBoCSxcQAvD_BwE&kwd=&mtp=&gclid=CjwKCAiAzp6eBhByEiwA_gGq5NHWdx2TRZgQW9ybhclwtfQvKzNnbPTLrgFsu0YNGFANSfwtQy2KdBoCSxcQAvD_BwE

Micopyretics Heaters International. (n.d.). *Free Radiating Heating Coil & Panels*. Micopyretics Heaters International. https://mhi-inc.com/free-radiating-heating-coil-panels-up-to-1900c/

Molloy, P., & Baronett, L. (2019). The Truth About Hydrogen. https://rmi.org/the-truth-about-hydrogen/

Mott Corporation. (2022). *Ultra High Purity Porous Ceramics*. https://mottcorp.com/product/ultra-high-purity-products/uhp-porous-alumina-ceramics/

Murphy, C. (2018). *High Temperature Insulation Materials & Applications*. Thermaxx jackets. Retrieved 15 November from https://blog.thermaxxjackets.com/high-temperature-insulation-materials-applications

Noh, Y.-G., Lee, Y. J., Kim, J., Kim, Y. K., Ha, J., Kalanur, S. S., & Seo, H. (2022). Enhanced efficiency in CO2-free hydrogen production from methane in a molten liquid alloy bubble column reactor with zirconia beads. *Chemical Engineering Journal, 428*, 131095.

Noordgastransport. (2022). *A sustainable future*. https://noordgastransport.nl/a-sustainable-future/

[Record #21 is using a reference type undefined in this output style.]

Offshore Wind Programme Board. (2016). Transmission Cost for Offshore Wind.

Omrop Fryslan. (2022). *ONE-Dyas steekt definitief 500 miljoen in gasveld ten noorden van Schiermonnikoog*. https://www.omropfryslan.nl/nl/nieuws/1169277/one-dyas-steekt-definitief-500-miljoen-in-gasveld-ten-noorden-van-schiermonnikoog

ONE-Dyas. (2020). N05-A Wabo-Vergunningsaanvraag: Bijlage 1 Technische beschrijving.

Oni, A., Anaya, K., Giwa, T., Di Lullo, G., & Kumar, A. (2022). Comparative assessment of blue hydrogen from steam methane reforming, autothermal reforming, and natural gas decomposition technologies for natural gas-producing regions. *Energy Conversion and Management, 254*, 115245.

Ostrowicki, S. (2021, 23 February). *Guidance on the carriage of coal*. Britannia. https://britanniapandi.com/2021/02/carriage-of-coal/#:~:text=Coal%20cargo%20should%20not%20be,cargo%2C%20as%20defined%20in%20MSC.

Palmer, C., Tarazkar, M., Kristoffersen, H. H., Gelinas, J., Gordon, M. J., McFarland, E. W., & Metiu, H. (2019). Methane pyrolysis with a molten Cu–Bi alloy catalyst. *ACS Catalysis, 9*(9), 8337-8345.

Parkinson, B., Matthews, J. W., McConnaughy, T. B., Upham, D. C., & McFarland, E. W. (2017). Techno-economic analysis of methane pyrolysis in molten metals: decarbonizing natural gas. *Chemical Engineering & Technology, 40*(6), 1022-1030.

Parkinson, B., Patzschke, C. F., Nikolis, D., Raman, S., Dankworth, D. C., & Hellgardt, K. (2021). Methane pyrolysis in monovalent alkali halide salts: Kinetics and pyrolytic carbon properties. *International Journal of Hydrogen Energy, 46*(9), 6225-6238.

Parkinson, B., Patzschke, C. F., Nikolis, D., Raman, S., & Hellgardt, K. (2021). Molten salt bubble columns for low-carbon hydrogen from CH4 pyrolysis: Mass transfer and carbon formation mechanisms. *Chemical Engineering Journal, 417*, 127407.

Pertl, A., Mostbauer, P., & Obersteiner, G. (2010). Climate balance of biogas upgrading systems. *Waste management, 30*(1), 92-99.

Phillips, W. C., Gakhar, R., Horne, G. P., Layne, B., Iwamatsu, K., Ramos-Ballesteros, A., Shaltry, M. R., LaVerne, J. A., Pimblott, S. M., & Wishart, J. F. (2020). Design and performance of high-temperature furnace and cell holder for in situ spectroscopic, electrochemical, and radiolytic investigations of molten salts. *Review of Scientific Instruments, 91*(8), 083105.

Pijkeren, G. v. (2020). Webinar hydrogen infrastructure.

[Record #22 is using a reference type undefined in this output style.]

Prognos. (2022). *Strompreisprognose*.

Rahimi, N., Kang, D., Gelinas, J., Menon, A., Gordon, M. J., Metiu, H., & McFarland, E. W. (2019). Solid carbon production and recovery from high temperature methane pyrolysis in bubble columns containing molten metals and molten salts. *Carbon, 151*, 181-191.

Rasmussen, S. (2011). Economies of scale and size. In *Production Economics* (pp. 111-120). Springer.

Ross, T., Aceves, S., & Espinosa-Loza, F. (2021). *Safety Note: Demonstration of a Hydrogen Hybrid Vehicle with a Cryogenic Capable Pressure Vessel*.

Rostrup-Nielsen, J. R. (1993). Production of synthesis gas. *Catalysis Today, 18*(4), 305-324.

Sada, E., Katoh, S., Yoshii, H., Yamanishi, T., & Nakanishi, A. (1984). Performance of the gas bubble column in molten salt systems. *Industrial & Engineering Chemistry Process Design and Development, 23*(1), 151-154.

Saito, M. (1998). Dispersion characteristics of gas-liquid two-phase pools. Proc. 6th Int. Conf. Nucl. Eng,(ICONE-6), San Diego, USA,(1998-5),

Sánchez-Bastardo, N., Schlögl, R., & Ruland, H. (2020). Methane Pyrolysis for CO2-Free H2 Production: A Green Process to Overcome Renewable Energies Unsteadiness. *Chemie Ingenieur Technik, 92*(10), 1596-1609.

Saniere, A., Hénaut, I., & Argillier, J. F. (2004). Pipeline transportation of heavy oils, a strategic, economic and technological challenge. *Oil & gas science and technology, 59*(5), 455-466 %@ 1294-4475.

Scheiblehner, D., Neuschitzer, D., Wibner, S., Sprung, A., & Antrekowitsch, H. (2022). Hydrogen production by methane pyrolysis in molten binary copper alloys. *International Journal of Hydrogen Energy*.

Schmidt + Clemens Group. (2013). *Centralloy® G 4852 R material data sheet*. https://dl.asminternational.org/alloy-digest/article-pdf/62/3/SS-1137/374555/ad_v62_03_ss-1137.pdf

Schneider, S., Bajohr, S., Graf, F., & Kolb, T. (2020). State of the Art of Hydrogen Production via Pyrolysis of Natural Gas. *ChemBioEng Reviews, 7*(5), 150-158.

Serban, M., Lewis, M. A., Marshall, C. L., & Doctor, R. D. (2003). *Hydrogen Production by Direct Contact Pyrolysis of Natural Gas*.

Setioputro, N. T., Kosasih, D. P., Sukwadi, R., & Widjaja, W. (2021). The cooling system design of biomass gasification in direct-flow reactor. *J. Mech. Eng. Res. Dev, 44*(1).

Shenzhen Honyantech. (2023). *Industrial Salt*. Retrieved 13 January from https://honyan.en.alibaba.com/productgrouplist-823166694/Industrial_Salt.html?spm=a2700.shop_index.74.4.e3ec7eb2TT6HTp

Siemens. (2017). *High performance at a compact size: Transformers for the offshore transformer module (OTM®) made by Siemens*. https://www.google.com/url?sa=t&rct=j&q=&esrc=s&source=web&cd=&cad=rja&uact=8&ved=2ahUKEwjiy7XLirj8AhXX7rsIHUi_CZsQFnoECDIQAQ&url=https%3A%2F%2Fwww.midel.com%2Fapp%2Fuploads%2F2018%2F08%2FSiemens-offshore-transformer.pdf&usg=AOvVaw08cSeWUhy6QgIsMT-6x_vY

[Record #105 is using a reference type undefined in this output style.]

Sun, Z., Parkinson, B., Agbede, O. O., & Hellgardt, K. (2020). Noninvasive differential pressure technique for bubble characterization in high-temperature opaque systems. *Industrial & Engineering Chemistry Research, 59*(13), 6236-6246.

Tang, O., Rehme, J., & Cerin, P. (2022). Levelized cost of hydrogen for refueling stations with solar PV and wind in Sweden: On-grid or off-grid? *Energy, 241*, 122906.

Thorat, B., Shevade, A., Bhilegaonkar, K., Aglawe, R., Veera, U. P., Thakre, S., Pandit, A., Sawant, S., & Joshi, J. (1998). Effect of sparger design and height to diameter ratio on fractional gas hold-up in bubble columns. *Chemical Engineering Research and Design, 76*(7), 823-834.

Tiseo, I. (2022). *Weekly European Union Emission Trading System (EU-ETS) carbon pricing in 2022*. Statista. Retrieved 15 January from https://www.statista.com/statistics/1322214/carbon-prices-european-union-emission-trading-scheme/

Towler, G., & Sinnott, R. (2008). Principles, practice and economics of plant and process design. *Chemical Engineering Design: Butterworth-Heinemann (December 10, 2007)*.

Trading economics. (2022a). *Steel*. Retrieved 4 November from https://tradingeconomics.com/commodity/steel

Trading economics. (2022b). *Titanium*. Retrieved 4 November from

Upham, D. C., Agarwal, V., Khechfe, A., Snodgrass, Z. R., Gordon, M. J., Metiu, H., & McFarland, E. W. (2017). Catalytic molten metals for the direct conversion of methane to hydrogen and separable carbon. *Science*, 917-921.

Van Wijk, C. (2022). *Expert advise* [Interview].

Wain, Y. (2014). Updating the Lang factor and testing its accuracy, reliability and precision as a stochastic cost estimating method. *PM World Journal, 3*(10).

Weidenfeller, D., Kulik, R., Rothenpieler, K., Stückrath, K., & Hetzer, J. (2016). Design, Simulation and Practical Experience of the Largest Syngas Cooler in Operation for Coal Gasification. Proceedings of the 8th International Freiberg Conference, Cologne, Germany,

Xebec. (2016). *Pressure Swing Adsorption (PSA) Systems for Ultra-Pure Hydrogen & Other Industry Gas Purification*. Xebec. https://www.google.com/url?sa=t&rct=j&q=&esrc=s&source=web&cd=&cad=rja&uact=8&ved=2ahUKEwjC-czLkLj8AhUfh_0HHb_RAOAQFnoECBEQAQ&url=https%3A%2F%2Fxebecinc.com%2Fwp-content%2Fuploads%2F2020%2F03%2FH2X_Hydrogen_2016_Web.pdf&usg=AOvVaw1EPz3GN0EhG8QSciZnLKkl

Xiao, G., Saleman, T. L., Zou, Y., Li, G., & May, E. F. (2019). Nitrogen rejection from methane using dual-reflux pressure swing adsorption with a kinetically-selective adsorbent. *Chemical Engineering Journal, 372*, 1038-1046.

8 Appendices

Appendix A1: The equilibrium constant for partial pressure

Appendix A2: Material properties and cost

Appendix A3: Natural gas composition

Appendix A4: 3D and the 3 orthographic views of a reactor unit design

Appendix A5: Results integration methane pyrolysis and offshore design models

Appendix A6: Economic analysis background

Appendix A1: The equilibrium constant for partial pressure

The equilibrium constant of an equation is the ratio between reactants (A and B) and products (C and D) at equilibrium at a certain pressure and temperature. For the equation, $aA + bB \rightleftharpoons cC + dD$, Kp is determined by dividing the partial pressure of the products by the partial pressure of the reactants in the following fashion:

$$K_p = \frac{(P_C)^c (P_D)^d}{(P_A)^a (P_B)^b} \tag{A1.1}$$

Since partial pressure only applies to gasses, the solid carbon is not taken into account for determination of the equilibrium constant for methane pyrolysis ($CH_4(g) \rightleftharpoons C(s) + 2H_2(g)$). The partial pressures for hydrogen and methane are shown below:

$$P_{H_2} = x_{H_2} P_{total} = \frac{2\, X_{CH_4}}{1 + X_{CH_4}}\, P_{total} \tag{A1.2}$$

$$P_{CH_4} = x_{CH_4} P_{total} = \frac{1 - X_{CH_4}}{1 + X_{CH_4}}\, P_{total} \tag{A1.3}$$

Where, x indicates the mole fraction of the respective molecule, X_{CH_4} the methane conversion rate, and P_{total} the total pressure of the system. Since the equilibrium constant is influenced by the temperature, $K_P(T)$, filling the partial pressures in the equation for the equilibrium constant, makes it possible to determine the maximum conversion at a certain temperature and pressure.

$$K_p(T) = \frac{{P_{H_2}}^2}{P_{CH_4}} = \frac{P_{total} \cdot \left(4{X_{CH_4}}^2\right)/\left({X_{CH_4}}^2 + 2X_{CH_4} + 1\right)}{\left(1 - X_{CH_4}\right)/\left(1 + X_{CH_4}\right)} \tag{A1.4}$$

Appendix A2: Material properties and cost

In Appendix A2, the properties of the various materials utilized in this research are listed.

A2.1 $Cu_{0.45}Bi_{0.55}$

The Cu0.45Bi0.55 alloy consist of the metals copper and bismuth, in a 45:55 mol% distribution. The copper serves as catalytic metal to foster conversions at lower temperatures. Bismuth makes sure that the metal layer is molten at the operational temperature due to its relative low liquidus temperature.

Table A8.1: *Material properties CuBi*

Property	Abbreviation	Unit	Correlation
Density	ρ	$kg.m^{-3}$	$10341 - 1.1154 \times T$
Surface tension	σ	$N.m^{-1}$	$0.4458 - 0.00003606 \times T$
Dynamic viscosity	μ	$kg.m^{-1}.s^{-1}$	$A \times exp\left(\frac{B}{RT}\right)$
- Empirical parameter	A	$\frac{kg.m^{-1}.s^{-1}}{exp(J \times K^{1.27}.mol^{-1})}$	$\frac{1.7 \times 10^{-7} \rho^{2/3} T_m^{1/2} M^{-1/6}}{exp\left(\frac{B}{RT_m}\right)}$
- Empirical parameter	B	$K^{1.27}$	$2.65\ T_m^{1.27}$
- Molar mass	M	$kg.mol^{-1}$	$\frac{63.5460 \times .27 + 208.9804 \times .55}{1000}$
- Liquidus temperature	T_m	K	1087
Kinematic viscosity	ν	$m^2.s^{-1}$	$\frac{\mu}{\rho}$

All data comes from Catalan and Rezaei (2022). They combined results from multiple experiments to come to the following correlations and extrapolated the range to fit their research range 950 – 1150 ˚C. This work can be found in the Supplementary Material belonging to the report . In this research, the range is assumed to apply to the range 900 – 1200 ˚C.

Table A8.2: *Material cost CuBi*

Material composition	[mol%]	Price [a] [$.mt^{-1}]	Source [$.mt^{-1}]
Copper	45	9,100	(Business Insider, 2023)
Bismuth	55	3,900	(Argus, 2023)
Total		6,240 [b]	

[a] rounded to hundreds for materials

[b] the price is wrongly calculated based on mol%, where this should be wt%. As the effect of the reactor units cost on the LCOH has been limited. This effect will also be limited

A2.2 Ni0.27Bi0.73

The Ni0.27Bi0.73 alloy is composed of nickel and bismuth in a 27:73 mol% ratio. Nickel serves as a catalytic metal, promoting conversions at lower temperatures, although it is a relatively expensive metal. Bismuth is included in the alloy to ensure that the metal layer remains molten at the operational temperature, due to its relatively low liquidus temperature.

Table A8.3: *Material properties for NiBi*

Property	Abbreviation	Unit	Correlation
Density	ρ	$kg.m^{-3}$	$10539 - 1.159 \times T$
Surface tension	σ	$N.m^{-1}$	$0.4277 - 0.00005134 \times T$
Dynamic viscosity	μ	$kg.m^{-1}.s^{-1}$	$A \times exp\left(\frac{B}{RT}\right)$
- Empirical parameter	A	$\frac{kg.m^{-1}.s^{-1}}{exp(J \times K^{1.27}.mol^{-1})}$	$\frac{1.7 \times 10^{-7} \rho^{2/3} T_m^{1/2} M^{-1/6}}{exp\left(\frac{B}{RT_m}\right)}$
- Empirical parameter	B	$K^{1.27}$	$2.65\ T_m^{1.27}$
- Molar mass	M	$kg.mol^{-1}$	$\frac{58.6934 \times .27 + 208.9804 \times .73}{1000}$
- Liquidus temperature	T_m	K	1013
Kinematic viscosity	ν	$m^2.s^{-1}$	$\frac{\mu}{\rho}$

The data used in this study was obtained from Catalan and Rezaei (2022), who combined the results of multiple experiments to formulate the following correlations. These correlations were extrapolated to fit the temperature range of 950 - 1150°C in their research. This information can be found in the supplementary material accompanying the report. For the purposes of the current study, it is assumed that these correlations apply to the temperature range of 900 - 1200°C.

Table A8.4: *Material cost NiBi*

Material composition	[%]	Price [a] [$.mt^{-1}]	Source [$.mt^{-1}]
Nickel	27	22,900	(Business Insider, 2022)
Bismuth	73	3,900	(Argus, 2023)
Total		10,200	

[a] rounded to hundreds

[b] the price is wrongly calculated based on mol%, where this should be wt%

A2.3 NaCl

Sodium chloride (NaCl) is a salt composed of sodium and chlorine atoms. It will serve as salt layer for separating the metal that stick to the carbon particles to prevent metal contamination. The properties of NaCl are suitable separate the metal in a molten metal and salt reactor, it has low wettability regarding the carbon particles and the density is between the metal and carbon density in operating conditions.

Table A8.5: *Material properties NaCl*

Property	Abbreviation	Unit	Correlation
Density	ρ	$kg.m^{-3}$	$2138.9 - 0.5426 \times T$
Surface tension	σ	$N.m^{-1}$	$(191.16 - 0.07188 \times T) \times 10^{-3}$
Dynamic viscosity	μ	$kg.m^{-1}.s^{-1}$	$0.089272 \times exp\left(\frac{21960.0914}{RT}\right)$
Kinematic viscosity	ν	$m^2.s^{-1}$	$\frac{\mu}{\rho}$

In the study conducted by Janz (1988), the most limiting temperature range has been set to the viscosity, with an upper limit of 1210 K. Further analysis showed that the correlation between temperature and viscosity was relatively flat, indicating that no sudden changes in behaviour of the salt is expected. Hence, the correlations are assumed to apply to the 900 – 1050 ˚C temperature range in this research

Table A8.6: *Material cost NaCl*

Material composition		Price [a]	Source
	[mol%]	[$.mt^{-1}]	[$.mt^{-1}]
NaCl	100	100	(Shenzhen Honyantech, 2023)
Total		100	

[a] Rounded to hundredths

A2.4 NaBr

Sodium bromide (NaBr) is a salt composed of sodium and bromine atoms. It is being used as a salt layer in this study to separate the metal that tends to adhere to carbon particles, in order to prevent metal contamination. The properties of NaBr make it suitable for use in separating metal in a molten metal and salt reactor due to its low wettability with respect to carbon particles, and its density which lies between that of the metal and the carbon in operating conditions.

Table A8.7: *Material properties NaBr*

Property	Abbreviation	Unit	Correlation
Density	ρ	$kg.m^{-3}$	$3174.8 - 0.8169 \times T$
Surface tension	σ	$N.m^{-1}$	$(191.16 - 0.07188 \times T) \times 10^{-3}$
Dynamic viscosity	μ	$kg.m^{-1}.s^{-1}$	$0.1034 \times exp\left(\frac{20478.303}{RT}\right)$
Kinematic viscosity	v	$m^2.s^{-1}$	$\frac{\mu}{\rho}$

According to data from Janz (1988), again the correlation on viscosity of the salt is most limited by the temperature and can be described be the stated correlation until a maximum temperature of 1184 K. However, the correlation remains relatively flat within this range, indicating that the salt's behavior does not exhibit sudden changes as the temperature exceeds the boundaries. As a result, it is reasonable to assume that the correlations can be applied to the temperature range of 900 - 1050 °C in the current study.

Table A8.8: *Material cost NaBr*

Material composition		Price [a]	Source
	[%]	[$.mt^{-1}]	[$.mt^{-1}]
NaBr	100	1,500	(Gemhold tranding, 2023)
Total		1,500	

[a] Rounded to hundredths

A2.5 Centralloy G4852 R alloy

Special alloys containing high concentrations of nickel and chromium, are used for steam methane reformer installation. These installations are heated up to 1050°C, what makes the material excellent for the research purpose. A relative new and, therefore, strong material for these installations is the HP-40 grade Centralloy G4852 Micro R produced by (Schmidt + Clemens Group, 2013). This material is applied, and their material information comes from the material sheet belonging to the material.

Table 8.9: *Properties of Centralloy G4852 R alloy*

Property	Abbreviation	Unit	Correlation
Density	ρ	kg.m^{-3}	7900
Conductivity	q	$W.m^{-1}.K^{-1}$	14.6

Data on the wall material for the reactor comes from (Schmidt + Clemens Group, 2013)

Table A8.10: *Material cost NaBr*

Material composition [a] [wt%]	Price [a] [$.mt^{-1}]	Source [$.mt^{-1}]
Steel 38.1	3,700	(Trading economics, 2022a)
Nickel 35.0	22,900	(Business Insider, 2022)
Chromium 25.0	12,500	(IndexBox, 2022)
Niobium 1.5	45,000	(Globe metals and mining, 2022)
Titanium 0.45	11,000	(Trading economics, 2022b)
Total	13,270	

[a] Assumed composition (Schmidt + Clemens Group, 2013)

[a] Rounded to hundreds for all materials

Appendix A3: Natural gas composition from the N05-A gas field

Component	Mol%
Methane (C1)	69.600
Ethane (C2)	3.455
Propane (C_3)	0.864
i-Butane (iC_4)	0.135
n-Butane (nC_4)	0.220
neo-Pentane (C_5)	0.007
i-Pentane (iC_5)	0.055
n-Pentane (nC_5)	0.076
Hexane (C_6)	0.076
Me-Cyclopentane	0.003
Benzeene	0.068
Cyclohexane	0.022
Heptane	0.041
Me-Cycloheptane	0.019
Toluene	0.010
Octane	0.056
Nitrogen	23.995
Carbondioxide (CO_2)	1.288
Hydrogen sulphide (H_2S)	-
Total	**100.000**

Maximum extra flows	$m^3.d^{-1}$
Water	150
Condensate	80
Total	**230**

Note. Data from Permit application N05-A (ONE-Dyas, 2020)

Appendix A4: 3D and the 3 orthographic views of a reactor unit design

A4.1: 3D view of the reactor unit design

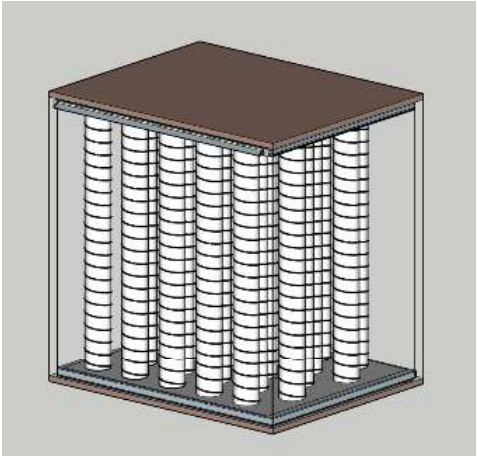

Note. to understand the reactor unit design better the insulation and shell are hidden.

A4.2: Orthographic views of the reactor unit design

Side view

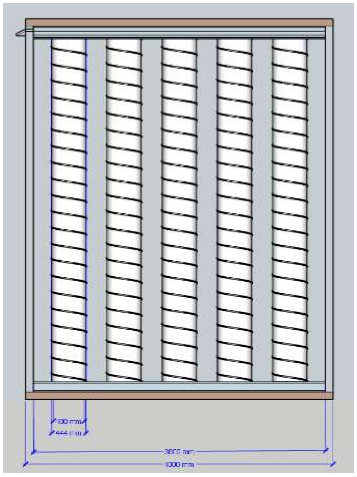

Front view

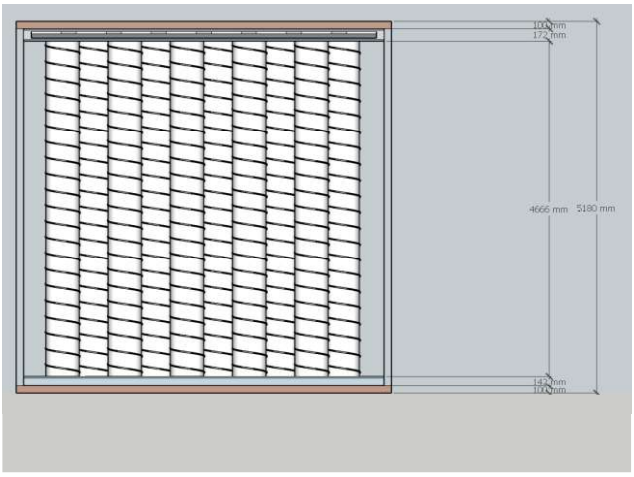

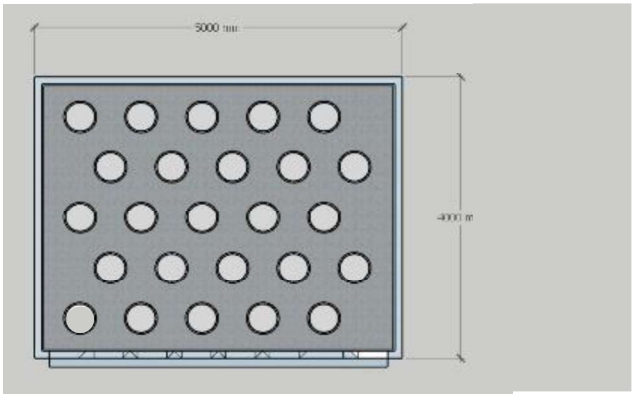

Top view

Note. to understand the front and side view of the reactor unit design better, the insulation and shell are hidden. For the top view the upper chamber is hidden to understand the column configuration better and see the uniform distribution.

Appendix A5: Results integration methane pyrolysis and offshore design models

A5.1: Single reactor unit results

Table 8.11: *Performance of single reactor unit at 1050 ˚C for 6 million Nm^3 flow natural gas (no nitrogen rejection) and a max column configuration.*

Configuration	NRA	N_{units} [-]	T [°C]	P [bar]	D [m]	N [-]	Hc [m]	X_{CH4} [%]	t_{wall} [m]
Max columns	**No**	**1**	**1050**	**5**	**0.45**	**65**	**0.74**	**73.9**	**0.035**
Max columns	No	1	1050	10	0.38	68	0.28	68.2	0.066
Max columns	No	1	1050	12	0.3	96	0.29	65.2	0.063
Max columns	No	1	1050	15	0.24	126	0.27	60.7	0.064
Max columns	No	1	1050	18	0.22	132	0.21	57.2	0.070
Max columns	No	1	1050	20	0.2	150	0.20	55.6	0.071
Max columns	No	1	1050	25	0.2	117	0.08	43.6	0.088
Max columns	No	1	1050	30	0.46	0	0.10	0.3	0.240
Max columns	No	1	1050	35	0.46	0	0.10	0.4	0.276
Max columns	No	1	1050	40	0.46	0	0.10	0.5	0.310
Max columns	No	1	1050	45	0.46	0	0.10	0.6	0.344
Max columns	No	1	1050	50	0.46	0	0.10	0.7	0.376

Configuration	NRA	N_{units} [-]	T [°C]	P [bar]	D [m]	N_{fr} [-]	Jg+ [-]	$\alpha_{average}$ [%]	α_{top} [%]
Max columns	**No**	**1**	**1050**	**5**	**0.45**	**5.014**	**72.7**	**75.3**	**76.5**
Max columns	No	1	1050	10	0.38	3.473	46.3	72.8	74.1
Max columns	No	1	1050	12	0.3	3.647	43.2	72.5	73.8
Max columns	No	1	1050	15	0.24	3.790	40.1	72.3	73.6
Max columns	No	1	1050	18	0.22	3.675	37.3	72.0	73.3
Max columns	No	1	1050	20	0.2	3.661	35.4	71.8	73.0
Max columns	No	1	1050	25	0.2	3.505	33.9	72.2	73.1
Max columns	No	1	1050	30	0.46	322.625	4731	83.6	83.6
Max columns	No	1	1050	35	0.46	276.602	4056	83.6	83.6
Max columns	No	1	1050	40	0.46	242.291	3553	83.6	83.6
Max columns	No	1	1050	45	0.46	215.440	3159	83.6	83.6
Max columns	No	1	1050	50	0.46	193.961	2844	83.7	83.7

Table 8.12: *Performance of single reactor unit at 1050 ˚C for 6 million Nm³ flow natural gas (no nitrogen rejection) and a max height configuration.*

Configuration	NRA	N_{units} [-]	T [°C]	P [bar]	D [m]	N [-]	Hc [m]	X_{CH4} [%]	t_{wall} [m]
Max height	**No**	**1**	**1050**	**5**	**0.39**	**15**	**4.66**	**44.0**	**0.030**
Max height	No	1	1050	10	0.25	16	4.62	34.2	0.043
Max height	No	1	1050	12	0.22	16	4.61	30.9	0.046
Max height	No	1	1050	15	0.22	9	4.57	24.1	0.058
Max height	No	1	1050	18	0.2	6	4.56	16.9	0.064
Max height	No	1	1050	20	0.21	4	4.53	14.6	0.074
Max height	No	1	1050	25	0.23	1	4.45	6.6	0.101
Max height	No	1	1050	30	0.46	0	-	-	0.240
Max height	No	1	1050	35	0.46	0	-	-	0.276
Max height	No	1	1050	40	0.46	0	-	-	0.310
Max height	No	1	1050	45	0.46	0	-	-	0.344
Max height	No	1	1050	50	0.46	0	-	-	0.376

Configuration	NRA	N_{units} [-]	T [°C]	P [bar]	D [m]	N_{fr} [-]	Jg+ [-]	$\alpha_{average}$ [%]	α_{top} [%]
Max height	**No**	**1**	**1050**	**5**	**0.39**	**29.693**	**400.9**	**81.9**	**82.1**
Max height	No	1	1050	10	0.25	37.420	404.5	82.2	82.4
Max height	No	1	1050	12	0.22	40.680	412.5	82.4	82.4
Max height	No	1	1050	15	0.22	55.546	563.3	82.7	82.8
Max height	No	1	1050	18	0.2	82.323	795.9	83.0	83.1
Max height	No	1	1050	20	0.21	97.602	967.0	83.2	83.2
Max height	No	1	1050	25	0.23	235.094	2438	83.5	83.5
Max height	No	1	1050	30	0.46	-	-	-	-
Max height	No	1	1050	35	0.46	-	-	-	-
Max height	No	1	1050	40	0.46	-	-	-	-
Max height	No	1	1050	45	0.46	-	-	-	-
Max height	No	1	1050	50	0.46	-	-	-	-

Table 8.13: *Performance of single reactor unit at 1050 ˚C for 4.6 million Nm^3 flow natural gas (90% nitrogen rejection from the original stream) and a max columns configuration.*

Configuration	NRA	N_{units} [-]	T [°C]	P [bar]	D [m]	N [-]	Hc [m]	X_{CH4} [%]	t_{wall} [m]
Max columns	**No**	**1**	**1050**	**5**	**0.45**	**65**	**0.71**	**77.9**	**0.035**
Max columns	No	1	1050	10	0.38	68	0.28	72.3	0.066
Max columns	No	1	1050	12	0.3	96	0.28	69.4	0.063
Max columns	No	1	1050	15	0.24	126	0.26	65.1	0.064
Max columns	No	1	1050	18	0.22	132	0.21	61.6	0.070
Max columns	No	1	1050	20	0.2	150	0.20	60.0	0.071
Max columns	No	1	1050	25	0.2	117	0.08	48.4	0.088
Max columns	No	1	1050	30	0.46	0	-	-	0.240
Max columns	No	1	1050	35	0.46	0	-	-	0.276
Max columns	No	1	1050	40	0.46	0	-	-	0.310
Max columns	No	1	1050	45	0.46	0	-	-	0.344
Max columns	No	1	1050	50	0.46	0	-	-	0.376

Configuration	NRA	N_{units} [-]	T [°C]	P [bar]	D [m]	N_{fr} [-]	Jg+ [-]	$\alpha_{average}$ [%]	α_{top} [%]
Max columns	**No**	**1**	**1050**	**5**	**0.45**	**4.368**	**63.3**	**73.1**	**74.8**
Max columns	No	1	1050	10	0.38	3.017	40.2	70.1	72.0
Max columns	No	1	1050	12	0.3	3.163	37.5	69.8	71.6
Max columns	No	1	1050	15	0.24	3.273	34.7	69.5	71.3
Max columns	No	1	1050	18	0.22	3.173	32.2	69.2	71.0
Max columns	No	1	1050	20	0.2	3.148	30	68.9	70.6
Max columns	No	1	1050	25	0.2	2.992	29	69.4	70.8
Max columns	No	1	1050	30	0.46	-	-	-	-
Max columns	No	1	1050	35	0.46	-	-	-	-
Max columns	No	1	1050	40	0.46	-	-	-	-
Max columns	No	1	1050	45	0.46	-	-	-	-
Max columns	No	1	1050	50	0.46	-	-	-	-

Table 8.14: *Performance of single reactor unit at 1050 ˚C for 4.6 million Nm³ flow natural gas (90% nitrogen rejection from the original stream) and a max height configuration.*

Configuration	NRA	N_{units} [-]	T [°C]	P [bar]	D [m]	N [-]	Hc [m]	X_{CH4} [%]	t_{wall} [m]
Max height	**No**	**1**	**1050**	**5**	**0.39**	**15**	**4.66**	**49.7**	**0.030**
Max height	No	1	1050	10	0.25	16	4.62	39.3	0.043
Max height	No	1	1050	12	0.22	16	4.61	35.8	0.046
Max height	No	1	1050	15	0.22	9	4.57	28.4	0.058
Max height	No	1	1050	18	0.2	6	4.56	20.3	0.064
Max height	No	1	1050	20	0.21	4	4.53	17.7	0.074
Max height	No	1	1050	25	0.23	1	4.45	8.2	0.101
Max height	No	1	1050	30	0.46	0	-	-	0.240
Max height	No	1	1050	35	0.46	0	-	-	0.276
Max height	No	1	1050	40	0.46	0	-	-	0.310
Max height	No	1	1050	45	0.46	0	-	-	0.344
Max height	No	1	1050	50	0.46	0	-	-	0.376

Configuration	NRA	N_{units} [-]	T [°C]	P [bar]	D [m]	N_{fr} [-]	Jg+ [-]	$\alpha_{average}$ [%]	α_{top} [%]
Max height	**No**	**1**	**1050**	**5**	**0.39**	**25.739**	**347.5**	**81.5**	**81.8**
Max height	No	1	1050	10	0.25	31.622	341.8	81.8	82.0
Max height	No	1	1050	12	0.22	34.970	354.6	82.0	82.2
Max height	No	1	1050	15	0.22	46.249	469.0	82.5	82.6
Max height	No	1	1050	18	0.2	67.845	656.0	82.9	82.9
Max height	No	1	1050	20	0.21	78.577	778	83.0	83.0
Max height	No	1	1050	25	0.23	181.915	1886	83.4	83.4
Max height	No	1	1050	30	0.46	-	-	-	-
Max height	No	1	1050	35	0.46	-	-	-	-
Max height	No	1	1050	40	0.46	-	-	-	-
Max height	No	1	1050	45	0.46	-	-	-	-
Max height	No	1	1050	50	0.46	-	-	-	-

A5.2: Multiple reactor unit results

Table 8.15: *Reactor unit design for Flow Design-1 for the right amount of reactor units and minimum conversion of 81.0% within methane pyrolysis model limits*

Configuration	NRA	N_{units} [-]	T [°C]	P [bar]	D [m]	N [-]	Hc [m]	X_{CH4} [%]	t_{wall} [m]
Max columns	No	19	1000	6	0.46	65	0.46	88.9	0.027
Max columns	No	19	1000	8	0.44	68	0.39	86.1	0.036
Max columns	No	19	1000	10	0.46	54	0.31	83.6	0.048
Max columns	**No**	**19**	**1000**	**12**	**0.44**	**54**	**0.25**	**81.1**	**0.056**
Max columns	No	19	1000	14	0.4	65	0.23	79.0	0.061
Max columns	No	19	1000	16	0.38	68	0.19	77.0	0.066
Max columns	No	19	1000	18	0.34	77	0.19	75.1	0.067

Configuration	NRA	N_{units} [-]	T [°C]	P [bar]	D [m]	N_{fr} [-]	Jg+ [-]	$\alpha_{average}$ [%]	α_{top} [%]
Max columns	No	19	1000	6	0.46	0.219	3.21	25.29	28.2
Max columns	No	19	1000	8	0.44	0.170	2.44	22.28	24.6
Max columns	No	19	1000	10	0.46	0.150	2.20	21.62	23.7
Max columns	**No**	**19**	**1000**	**12**	**0.44**	**0.134**	**1.97**	**20.79**	**22.6**
Max columns	No	19	1000	14	0.4	0.122	1.68	19.35	20.9
Max columns	No	19	1000	16	0.38	0.115	1.53	18.76	20.2
Max columns	No	19	1000	18	0.34	0.118	1.49	18.78	20.2

Table 8.16: *Reactor unit design for Flow Design-2 for the right amount of reactor units and mminimum conversion of 62.5% within methane pyrolysis model limits*

Configuration	NRA	N_{units} [-]	T [°C]	P [bar]	D [m]	N [-]	Hc [m]	X_{CH4} [%]	t_{wall} [m]
Max columns	Yes	10	950	5	0.46	68	0.59	76.0	0.016
Max columns	Yes	10	950	10	0.45	65	0.40	74.7	0.035
Max columns	Yes	10	950	12	0.46	54	0.34	72.9	0.044
Max columns	Yes	10	950	15	0.45	54	0.27	70.3	0.055
Max columns	Yes	10	950	18	0.4	65	0.24	67.4	0.059
Max columns	**Yes**	**10**	**950**	**19**	**0.39**	**68**	**0.23**	**66.6**	**0.061**
Max columns	Yes	10	950	20	0.39	65	0.21	65.7	0.064
Max columns	Yes	10	950	25	0.36	68	0.15	61.6	0.074
Max columns	Yes	10	950	30	0.27	105	0.19	58.1	0.067
Max columns	Yes	10	950	35	0.26	105	0.14	55.3	0.075
Max columns	Yes	10	950	40	0.22	132	0.16	52.8	0.072
Max columns	Yes	10	950	45	0.21	132	0.13	50.5	0.077
Max columns	Yes	10	950	50	0.20	132	0.11	48.3	0.081

Configuration	NRA	N_{units} [-]	T [°C]	P [bar]	D [m]	N_{fr} [-]	Jg+ [-]	$\alpha_{average}$ [%]	α_{top} [%]
Max columns	Yes	10	950	5	0.46	0.376	5.52	33.8	37.7
Max columns	Yes	10	950	10	0.45	0.198	2.87	24.9	27.5
Max columns	Yes	10	950	12	0.46	0.184	2.71	24.7	27.1
Max columns	Yes	10	950	15	0.45	0.153	2.22	22.6	24.7
Max columns	Yes	10	950	18	0.4	0.139	1.90	21.3	23.1
Max columns	**Yes**	**10**	**950**	**19**	**0.39**	**0.134**	**1.80**	**20.8**	**22.5**
Max columns	Yes	10	950	20	0.39	0.132	1.78	20.8	22.5
Max columns	Yes	10	950	25	0.36	0.120	1.56	20.0	21.5
Max columns	Yes	10	950	30	0.27	0.130	1.46	19.9	21.3
Max columns	Yes	10	950	35	0.26	0.120	1.33	19.3	20.6
Max columns	Yes	10	950	40	0.22	0.125	1.27	19.3	20.5
Max columns	Yes	10	950	45	0.21	0.123	1.22	19.2	20.4
Max columns	Yes	10	950	50	0.2	0.123	1.19	19.3	20.5

Table 8.17: *Reactor unit design for Flow Design-2+ and 3 for the right amount of reactor units and mminimum conversion of 90.0% within methane pyrolysis model limits*

Configuration	NRA	N_{units} [-]	T [°C]	P [bar]	D [m]	N [-]	Hc [m]	X_{CH4} [%]	t_{wall} [m]
Max columns	Yes	33	1000	2	0.46	77	0.63	94.5%	0.005
Max columns	Yes	33	1000	3	0.46	72	0.56	93.9%	0.011
Max columns	Yes	33	1000	4	0.46	68	0.51	92.7%	0.016
Max columns	**Yes**	**33**	**1000**	**5**	**0.46**	**68**	**0.47**	**91.4%**	**0.022**
Max columns	Yes	33	1000	6	0.46	65	0.43	90.1%	0.027

Configuration	NRA	N_{units} [-]	T [°C]	P [bar]	D [m]	N_{fr} [-]	Jg+ [-]	$\alpha_{average}$ [%]	α_{top} [%]
Max columns	Yes	33	1000	2	0.46	0	4.92	25.3	29.8
Max columns	Yes	33	1000	3	0.46	0	3.21	20.7	23.7
Max columns	Yes	33	1000	4	0.46	0	2.43	18.2	20.4
Max columns	**Yes**	**33**	**1000**	**5**	**0.46**	**0**	**1.89**	**16.2**	**17.8**
Max columns	Yes	33	1000	6	0.46	0	1.61	15.2	16.6

Appendix A6: Economic analysis background

A6.1: Reactor material cost

Table A8.18: Reactor material cost for Flow Design-1

	Volume [M³]	Weight [mt]	Price [a] [€/mt]	Cost [million €]
Salt reactor fill NaCl	2.8	4	100	0.00
Metal reactor fill CuBi	8.5	76	6,240	0.42
Wall material	64.3	508	13,270 [c]	0.70
Total				**1.12**

[a] Prices can be found in Appendix A2

Table A8.19: Reactor material cost for Flow Design-2

	Volume [M³]	Weight [mt]	Price [€/mt]	Cost [million €]
Salt reactor fill NaCl	3.70	5	100	0.00
Metal reactor fill CuBi	11.10	100	6,240	0.62
Wall material	6.46	51	13,270 [c]	0.68
Total				**1.30**

[a] Prices can be found in Appendix A2

Table A8.20: Reactor material cost for Flow Design-2+ and Flow Design-3

	Volume [M³]	Weight [mt]	Price [€/mt]	Cost [million €]
Salt reactor fill NaCl	36.72	53	100	0.00
Metal reactor fill CuBi	110.16	983	6,240	6.13
Wall material	21.30	168	13,270	2.23
Total				**8.37**
Total with recycling [b]				9.63

[a] Prices can be found in Appendix A2

A6.2: Capital expenditure overview

Table A8.21

CAPEX	Flow design	Low [million €]	Base [million €]	High [million €]
Gas processing	1	350	500	750
	2	350	500	750
	2+	350	500	750
	3 [a]	350	500	750
Reactor units	1	6	11	36
	2	3	6	19
	2+	21	40	126
	3 [a]	24	46	144
Deck space & auxiliary equipment	1	120	172	257
	2	128	183	274
	2+	193	275	413
	3 [a]	297	424	635
Transformer	1	14	20	29
	2	11	16	24
	2+	15	22	33
	3 [a]	18	25	38
Onshore PSA	1	14	20	31
	2	12	17	25
	2+	11	15	23
	3 [a]	-	-	-
Total	**1**	**491**	**704**	**1,074**
	2	**493**	**706**	**1,069**
	2+	**575**	**830**	**1,311**
	3 [a]	**671**	**969**	**1,530**

[a] Including recycling

A6.3: Overview operational expenditure

Table A8.22: *Build-up of OPEX for Flow Design-1*

OPEX	Low [million €]	Medium [million €]	High [million €]
Natural gas	187	375	562
Discounted	*127*	*255*	*382*
Electricity	1286	1637	1910
Discounted	*832*	*1059*	*1236*
Carbon handling	77	116	155
Discounted	*34*	*55*	*76*
Total	**1551**	**2128**	**2627**
Discounted	***993***	***1369***	***1694***

Table A8.23: *Build-up of OPEX for Flow Design-2*

OPEX	Low [million €]	Medium [million €]	High [million €]
Natural gas	122	245	367
Discounted	*83*	*166*	*249*
Electricity	1289	1641	1914
Discounted	*833*	*1060*	*1237*
Carbon handling	76	114	153
Discounted	*33*	*54*	*75*
Total	**1488**	**2000**	**2434**
Discounted	***949***	***1280***	***1561***

Table A8.24: *Build-up of OPEX for Flow Design-2+*

OPEX	Low [million €]	Medium [million €]	High [million €]
Natural gas	167	334	501
Discounted	*113*	*227*	*340*
Electricity	1497	1906	2223
Discounted	*975*	*1242*	*1448*
Carbon handling	77	117	156
Discounted	*34*	*55*	*77*
Total	**1741**	**2356**	**2880**
Discounted	***1123***	***1524***	***1865***

Table A8.25: *Buildup of OPEX for Flow Design-3*

OPEX	Low [million €]	Medium [million €]	High [million €]
Natural gas	167	334	501
Discounted	*113*	*227*	*340*
Electricity	1722	2191	2557
Discounted	*1122*	*1428*	*1666*
Carbon handling	89	134	180
Discounted	*39*	*64*	*88*
Total	**1978**	**2660**	**3237**
Discounted	***1274***	***1718***	***2094***

A6.5: Levelized cost of hydrogen build-up in waterfall charts and background data

Flow Design-1

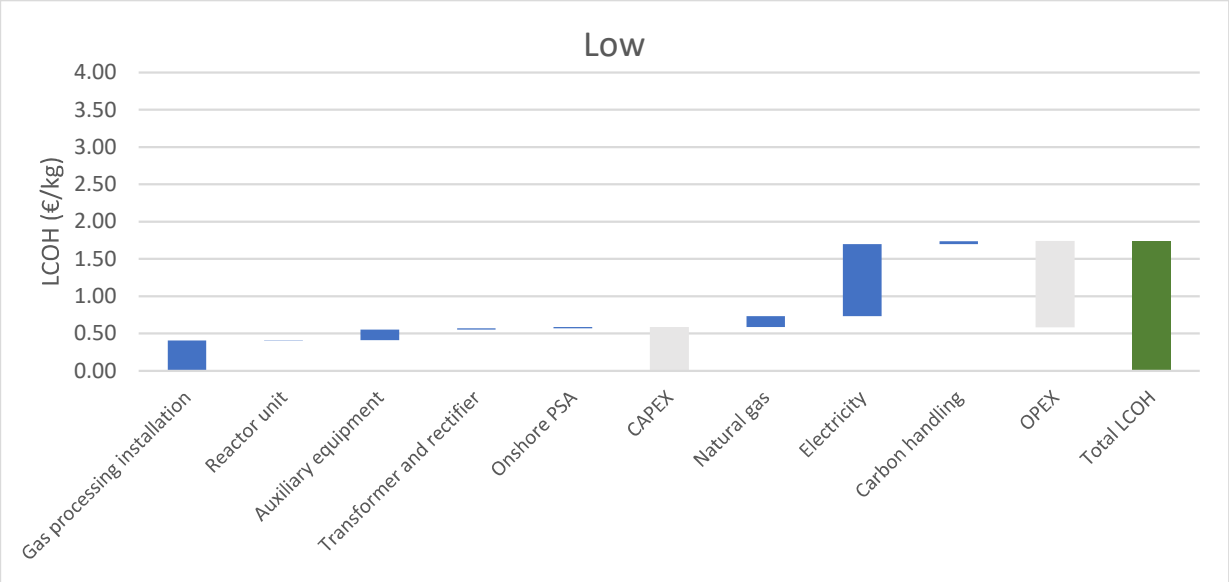

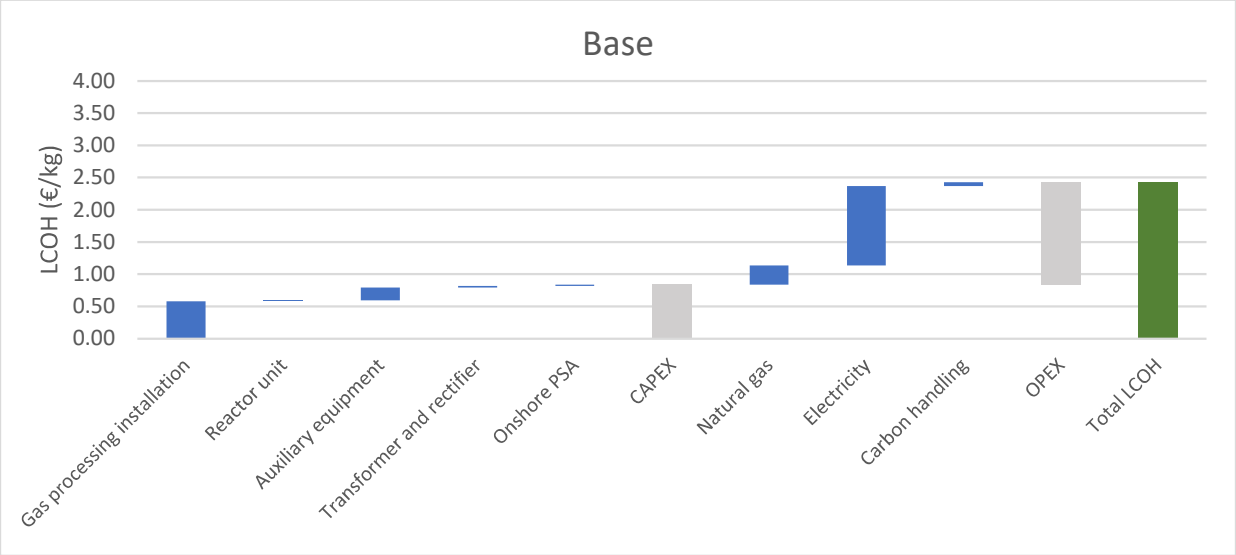

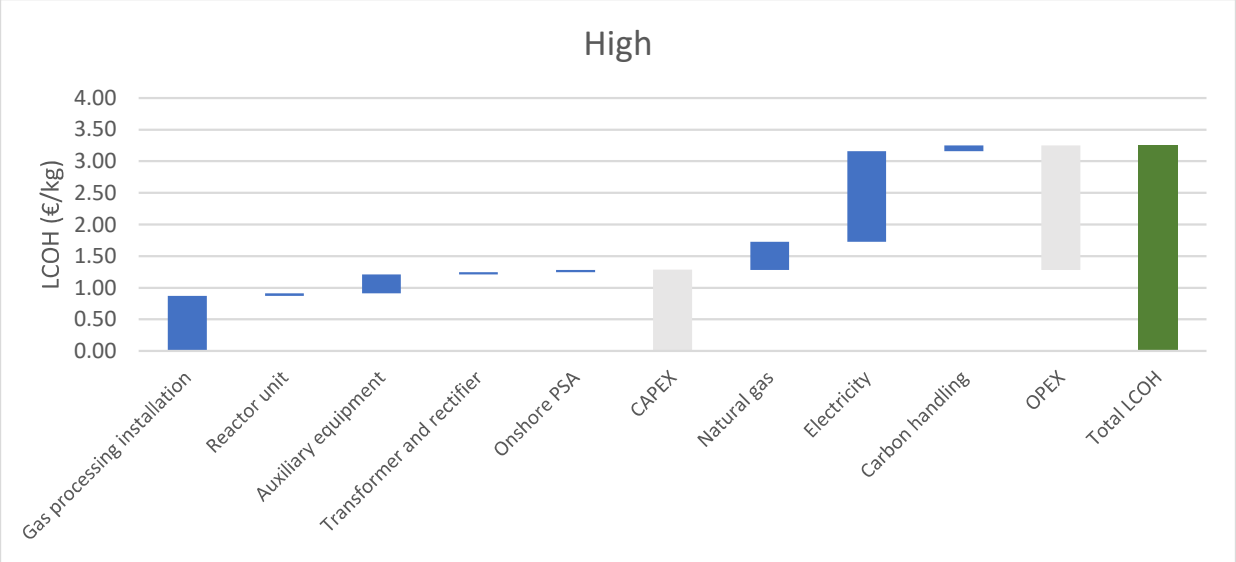

***Table A8.26**: Background data for waterfall chart Flow Design-1*

	Low [€/kg]	Base [€/kg]	High [€/kg]
Gas processing installation	0.41	0.58	0.87
Reactor unit	0.01	0.01	0.04
Auxiliary equipment	0.14	0.20	0.30
Transformer and rectifier	0.02	0.02	0.03
Onshore PSA	0.02	0.02	0.04
CAPEX	**0.59**	**0.84**	**1.28**
Natural gas	0.15	0.30	0.44
Electricity	0.97	1.23	1.44
Carbon handling	0.04	0.06	0.09
OPEX	**1.15**	**1.59**	**1.97**
Total LCOH	**1.74**	**2.43**	**3.25**

Flow Design-1 with adjusted installation pressure for optimum conversion

When the pressure would be adjusted according to the gas production, the methane conversion in the reactor units could be increased. This results in a higher methane production which can be seen in the following table.

***Table A8.27**: Background data for waterfall chart Flow Design-1 with adjusted installation pressure for optimum conversion*

	Low [€/kg]	Base [€/kg]	High [€/kg]
Gas processing installation	0.38	0.55	0.82
Reactor unit	0.01	0.01	0.04
Auxiliary equipment	0.13	0.19	0.28
Transformer and rectifier	0.02	0.02	0.03
Onshore PSA	0.02	0.02	0.03
CAPEX	**0.55**	**0.79**	**1.21**
Natural gas	0.14	0.28	0.42
Electricity	0.95	1.20	1.41
Carbon handling	0.04	0.06	0.08
OPEX	**1.12**	**1.55**	**1.91**
Total LCOH	**1.68**	**2.34**	**3.12**

Flow Design-1 with subtracted gas cost for resulting natural gas flow from hydrogen purification

Even though the waste stream from the pressure swing adsorption will contain a significant part nitrogen, the gas could be sold based on the heating value of the gas. To keep the gas price and the LCOH separate, the remaining heating value is subtracted form the gas stream. The OPEX for natural gas will therefore decrease, as this is also determined on the heating value of the flow injected in the methane pyrolysis reactor units.

Table A8.28: *Background data for waterfall chart Flow Design-1 with subtracted gas cost for resulting natural gas flow from hydrogen purification*

	Low [€/kg]	Base [€/kg]	High [€/kg]
Gas processing installation	0.41	0.58	0.87
Reactor unit	0.01	0.01	0.04
Auxiliary equipment	0.14	0.20	0.30
Transformer and rectifier	0.02	0.02	0.03
Onshore PSA	0.02	0.02	0.04
CAPEX	**0.59**	**0.84**	**1.28**
Natural gas	0.12	0.24	0.36
Electricity	0.97	1.23	1.44
Carbon handling	0.04	0.06	0.09
OPEX	**1.13**	**1.53**	**1.88**
Total LCOH	**1.71**	**2.37**	**3.17**

Flow Design-1 with external operator of gas production and processing

When the gas production and processing would be a separate operator the CAPEX and OPEX for gas production and processing and would disappear, however, as a replacement the market price for gas should be paid. When the market price is set to 15-25-35 €/MWh, the composition of the LCOH looks as followed:

***Table A8.29**: Background data for waterfall chart Flow Design-1 with external operator of gas production and processing*

	Low [€/kg]	Base [€/kg]	High [€/kg]
Gas processing installation	0.00	0.00	0.00
Reactor unit	0.01	0.01	0.04
Auxiliary equipment	0.14	0.20	0.30
Transformer and rectifier	0.02	0.02	0.03
Onshore PSA	0.02	0.02	0.04
CAPEX	**0.18**	**0.26**	**0.41**
Natural gas	1.13	1.88	2.64
Electricity	0.88	1.13	1.31
Carbon handling	0.04	0.06	0.09
OPEX	**2.05**	**3.07**	**4.04**
Total LCOH	**2.23**	**3.33**	**4.45**

Flow Design-1 with reduced system efficiency to 50%

The assumption has been made that the system efficiency of the methane pyrolysis installations equals 58% and therefore the electricity demand specifically for the methane pyrolysis related installations was set to 9 MWh/mt H_2. However, when the system efficiency would reduce to 50%, the electricity demand per produced hydrogen would increase. The effect is depicted in the table below:

Table A8.30: *Background data for waterfall chart Flow Design-1 with reduced system efficiency to 50%*

	Low [€/kg]	Base [€/kg]	High [€/kg]
Gas processing installation	0.41	0.58	0.87
Reactor unit	0.01	0.01	0.04
Auxiliary equipment	0.14	0.20	0.30
Transformer and rectifier	0.02	0.02	0.03
Onshore PSA	0.02	0.02	0.04
CAPEX	**0.59**	**0.84**	**1.28**
Natural gas	0.15	0.30	0.44
Electricity	1.06	1.35	1.57
Carbon handling	0.04	0.06	0.09
OPEX	**1.25**	**1.71**	**2.10**
Total LCOH	**1.83**	**2.55**	**3.39**

Flow Design-1 with 5% reduced conversion rate

Due to the uncertainties of Chapter 2 and Chapter 3, the methane conversion could be overestimated. The effect of a 5% reduction in conversion rate is taken into account in the model.

Table A8.31*: Background data for waterfall chart Flow Design-1 with 5% reduced conversion rate*

	Low [€/kg]	Base [€/kg]	High [€/kg]
Gas processing installation	0.43	0.62	0.93
Reactor unit	0.01	0.01	0.05
Auxiliary equipment	0.15	0.21	0.32
Transformer and rectifier	0.02	0.02	0.03
Onshore PSA	0.02	0.02	0.04
CAPEX	**0.62**	**0.89**	**1.36**
Natural gas	0.16	0.32	0.47
Electricity	0.99	1.26	1.47
Carbon handling	0.04	0.07	0.09
OPEX	**1.19**	**1.64**	**2.04**
Total LCOH	**1.81**	**2.54**	**3.40**

Flow Design-2

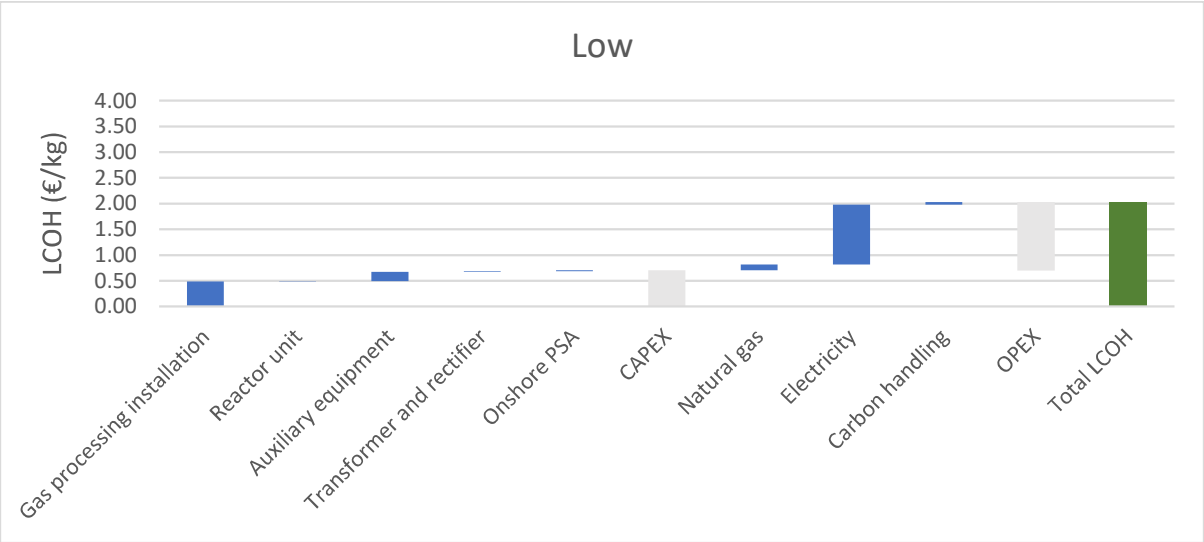

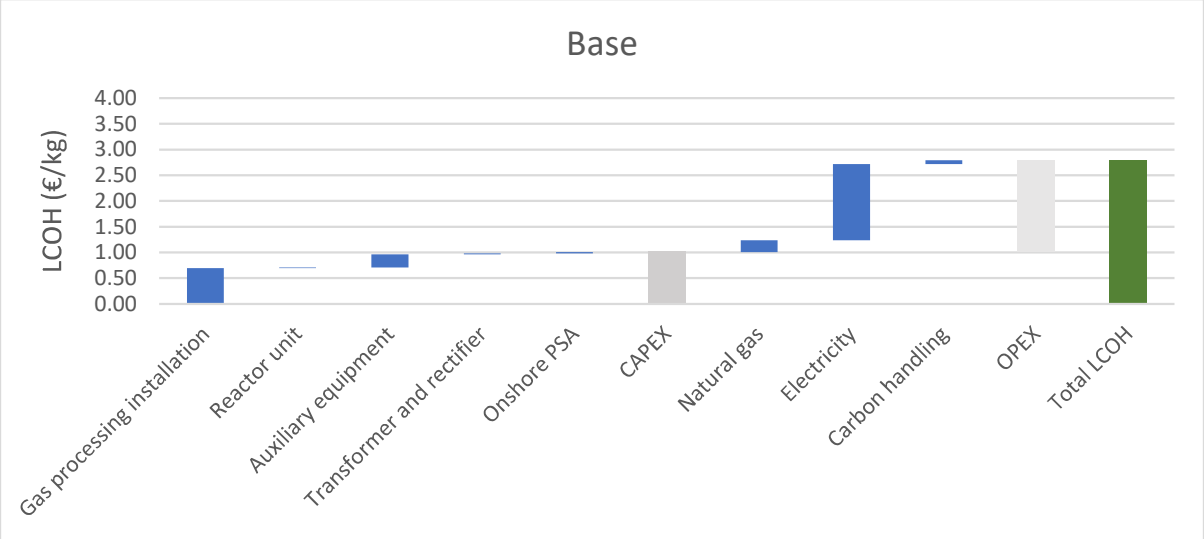

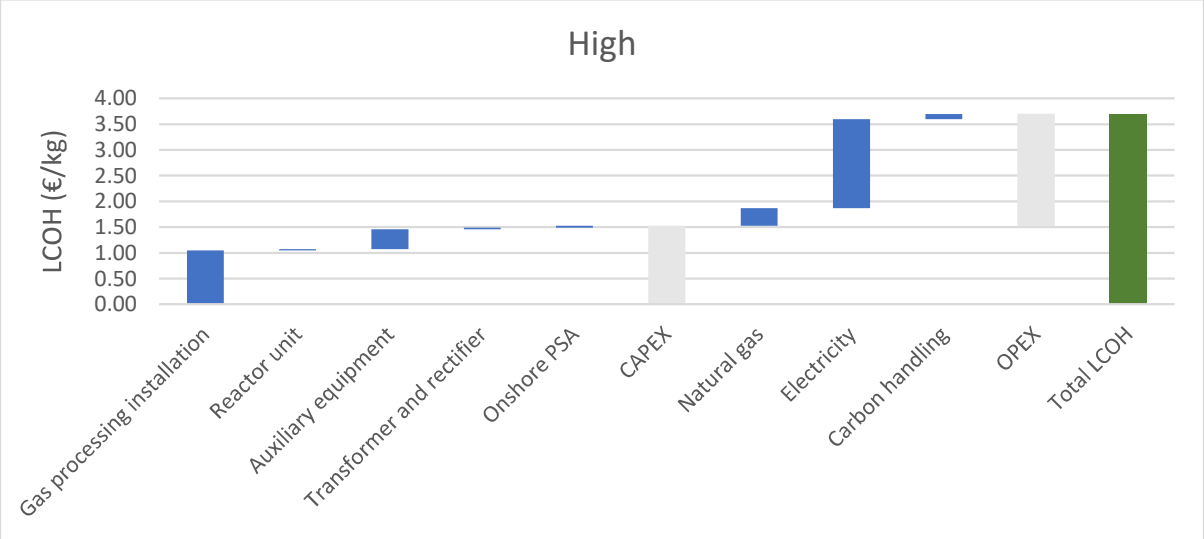

***Table A8.32**: Background data for waterfall chart Flow Design-2*

	Low [€/kg]	Base [€/kg]	High [€/kg]
Gas processing installation	0.49	0.70	1.05
Reactor unit	0.00	0.01	0.03
Auxiliary equipment	0.18	0.26	0.38
Transformer and rectifier	0.02	0.02	0.03
Onshore PSA	0.02	0.02	0.04
CAPEX	**0.70**	**1.01**	**1.52**
Natural gas	0.12	0.23	0.35
Electricity	1.16	1.48	1.72
Carbon handling	0.05	0.08	0.10
OPEX	**1.32**	**1.78**	**2.18**
Total LCOH	**2.03**	**2.79**	**3.70**

Flow Design-2+

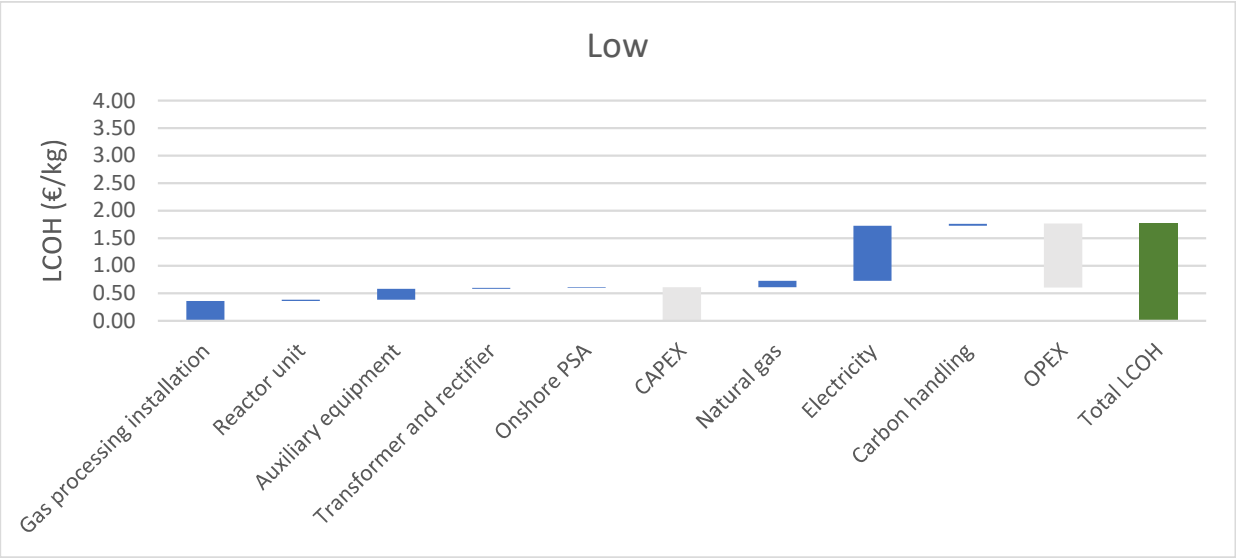

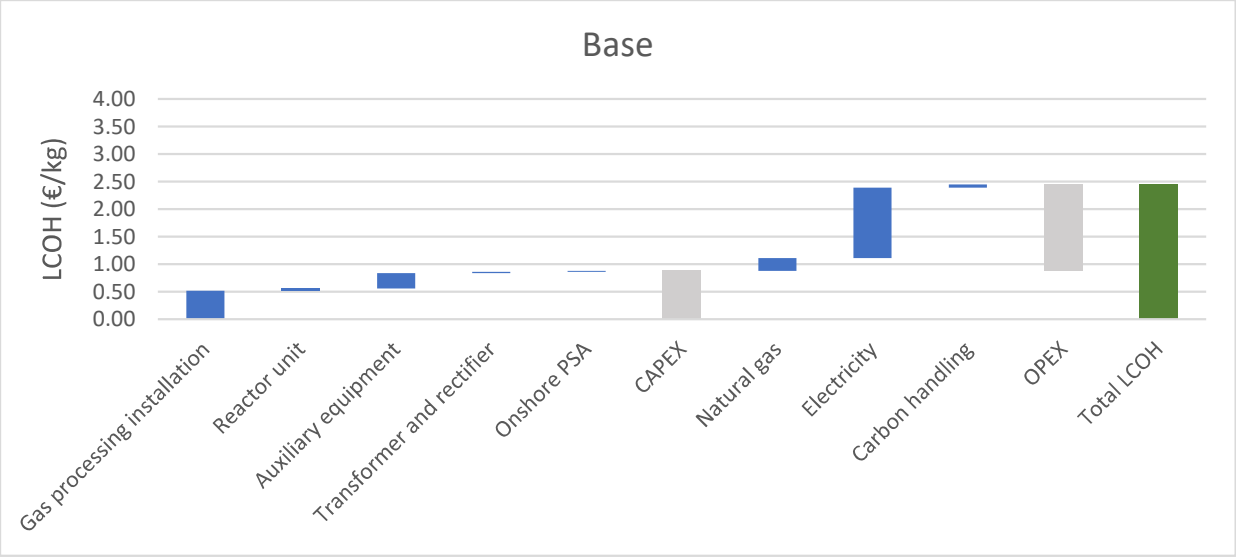

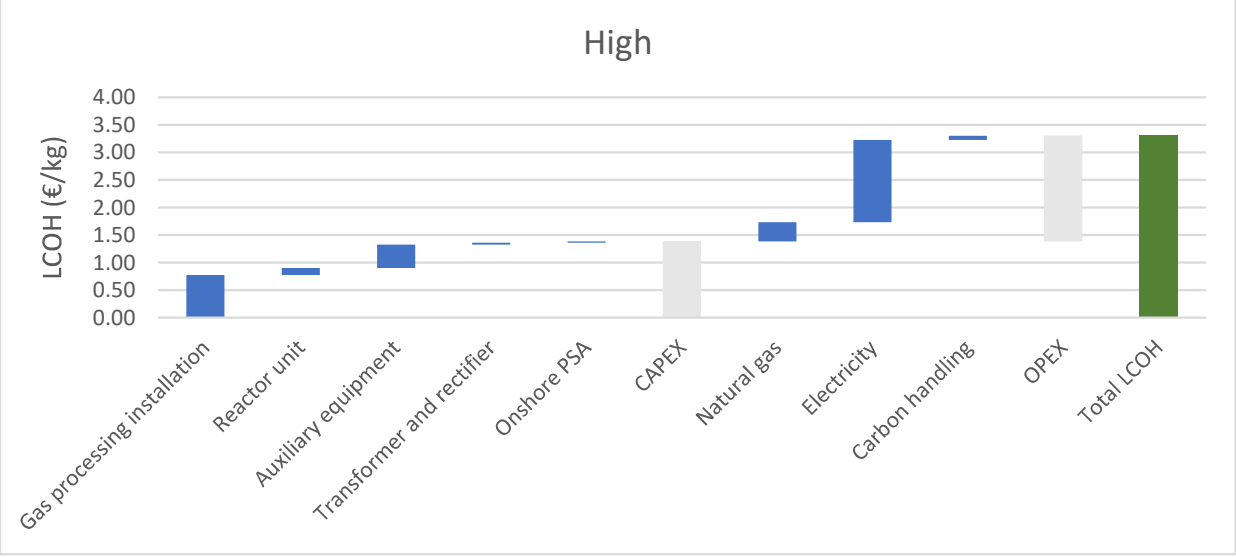

Table A8.33: *Background data for waterfall chart Flow Design-2+*

Electricity demand	Low [€/kg]	Base [€/kg]	High [€/kg]
Gas processing installation	0.36	0.51	0.77
Reactor unit	0.02	0.04	0.13
Auxiliary equipment	0.20	0.28	0.43
Transformer and rectifier	0.02	0.02	0.03
Onshore PSA	0.01	0.02	0.02
CAPEX	**0.61**	**0.88**	**1.38**
Natural gas	0.12	0.23	0.35
Electricity	1.00	1.28	1.49
Carbon handling	0.03	0.06	0.08
OPEX	**1.16**	**1.57**	**1.92**
Total LCOH	**1.76**	**2.45**	**3.31**

Flow Design-3

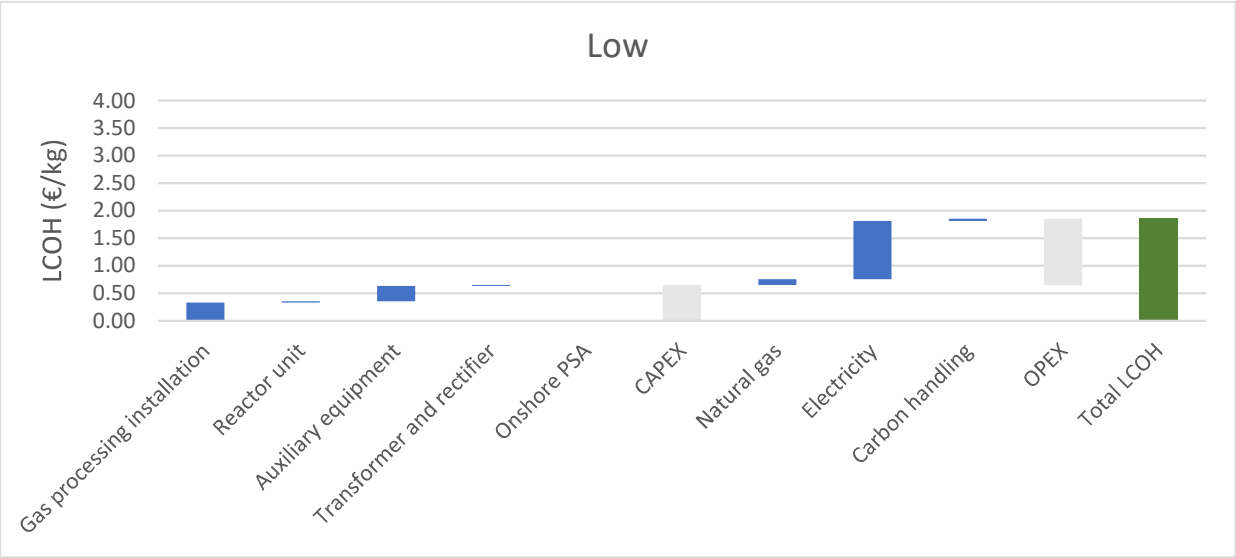

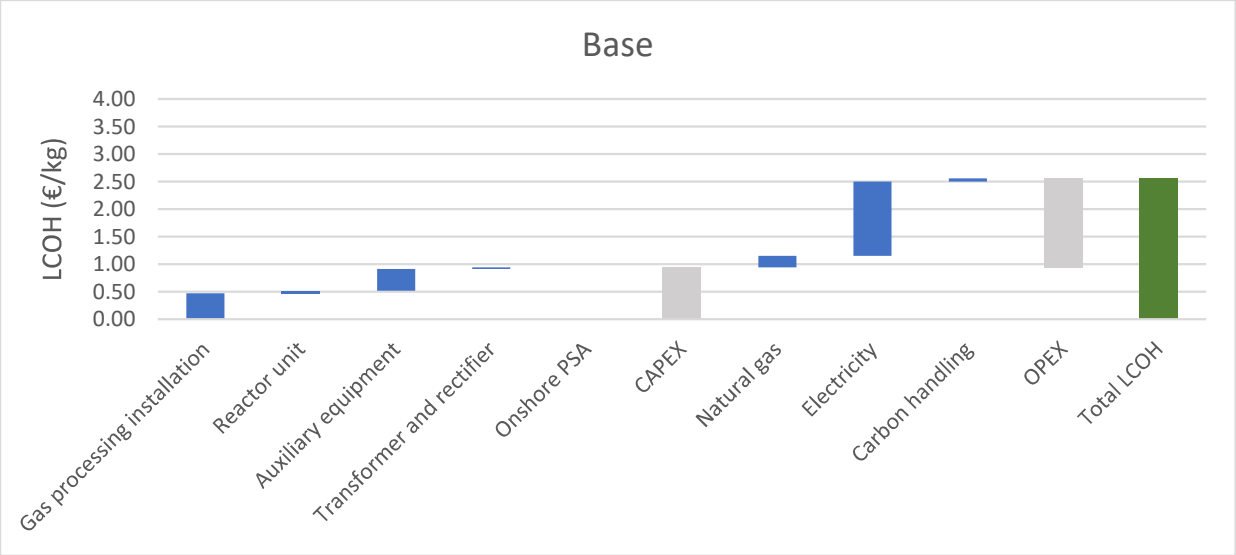

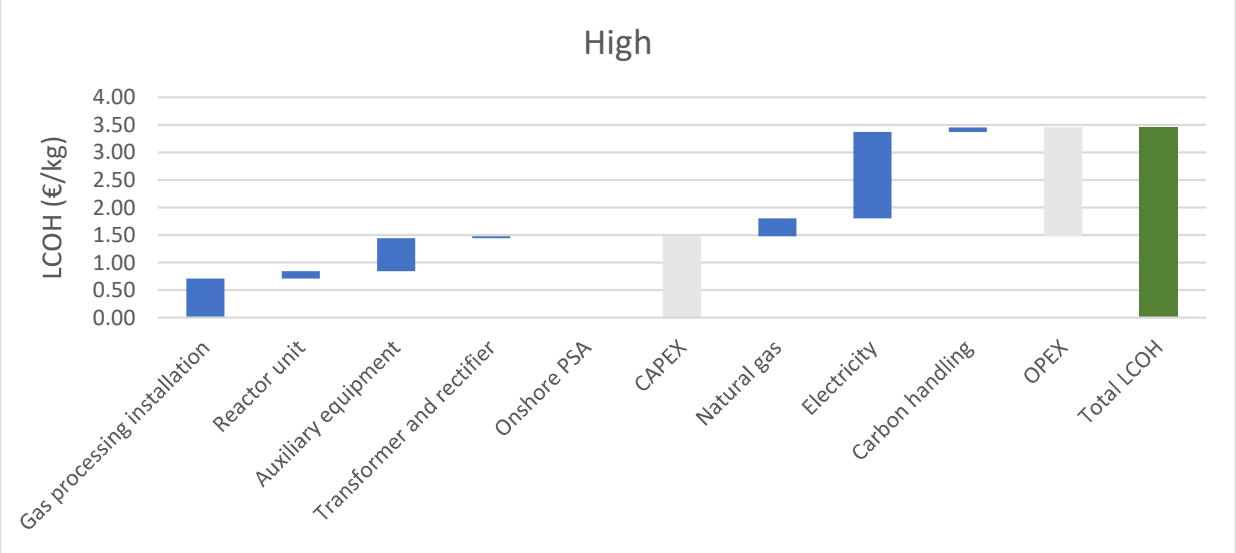

Table A8.34: *Background data for waterfall chart Flow Design-2+*

	Low [€/kg]	Base [€/kg]	High [€/kg]
Gas processing installation	0.33	0.47	0.71
Reactor unit	0.02	0.04	0.14
Auxiliary equipment	0.28	0.40	0.60
Transformer and rectifier	0.02	0.02	0.04
Onshore PSA	0.00	0.00	0.00
CAPEX	**0.65**	**0.94**	**1.48**
Natural gas	0.11	0.21	0.32
Electricity	1.06	1.35	1.57
Carbon handling	0.04	0.06	0.08
OPEX	**1.20**	**1.62**	**1.98**
Total LCOH	**1.85**	**2.56**	**3.46**

A6.6: Levelized cost of conventional natural gas hydrogen production technologies

***Table A8.35**: Build-up of LCOH of conventional hydrogen production technologies form natural gas*

Electricity demand	Unit	SMR	SMR+CCS	ATR	ATR+CCS
Natural gas	MWh/kg H_2	0.050	0.061	0.042	0.042
Electricity	MWh/kg H_2	0.001	0.001	0.002	0.004
CO_2 Tax	mt CO_2/kg H_2	0.011	0.008	0.011	0.004

[a] All information from (Oni et al., 2022)

[b] CCS in combination with SMR reduces the on-site emission from 9.17 to 5.52 kg CO2eq./kg H_2

[c] CCS in combination with ATR reduces the on-site emission from 8.39 to 0.62 kg CO2eq./kg H_2

A6.7: Sensitivity plots and data for cost-competitive offshore methane pyrolysis with ATR and ATR+CCS

The sensitivity analysis is executed based on four scenarios for gas price and electricity therefore this the structure of this Appendix will follow the same. The sensitivity analysis is both showed in a data table and a plot, to visualise the data. The order of the listed scenario is increasingly beneficial for the cost-competitiveness of the LCOH for offshore methane pyrolysis.

Table 8.36: *Data for sensitivity analysis for gas price = 25 €/MWh and electricity price = 66 €/MWh*

Components					LCOH		
Gas price	Electricity price	CO_2 tax	Carbon product value	CAPEX	ATR	ATR+CCS	OMP
[€/MWh]	[€/MWh]	[€/mt CO2]	[€/mt Cs]	[%]	[€/kg H2]	[€/kg H2]	[€/kg H2]
25	66	70	0	100	1.97	1.55	1.97
25	66	178	0	100	3.16	1.97	1.97
25	66	100	-101	100	2.30	1.67	1.67
25	66	100	-43	70	2.30	1.67	1.67

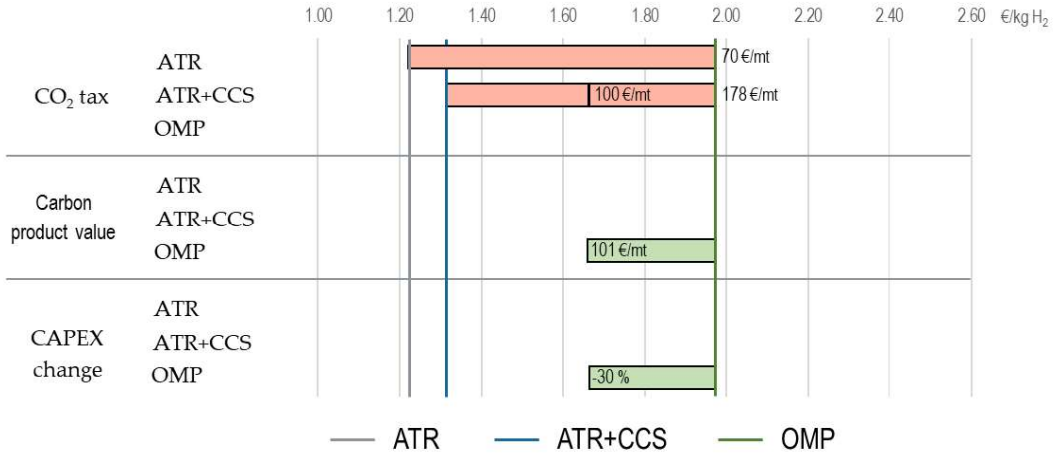

Figure 8.1: *Sensitivity plot for gas price = 25 €/MWh and electricity price = 66 €/MWh*

Table 8.37: *Data for sensitivity analysis for gas price = 35 €/MWh and electricity price = 84 €/MWh*

Components					LCOH		
Gas price	Electricity price	CO_2 tax	Carbon product value	CAPEX	ATR	ATR+CCS	OMP
[€/MWh]	[€/MWh]	[€/mt CO2]	[€/mt Cs]	[%]	[€/kg H2]	[€/kg H2]	[€/kg H2]
35	84	54	0	100%	2.25	1.97	2.25
35	84	126	0	100%	3.04	2.25	2.25
35	84	100	-34	100%	2.76	2.15	2.15
35	84	0	-165	100%	1.66	1.76	1.76
35	84	0	-198	100%	1.66	1.76	1.66
35	84	83	0	70%	2.57	2.08	2.08
35	84	0	-140	70%	1.66	1.76	1.66

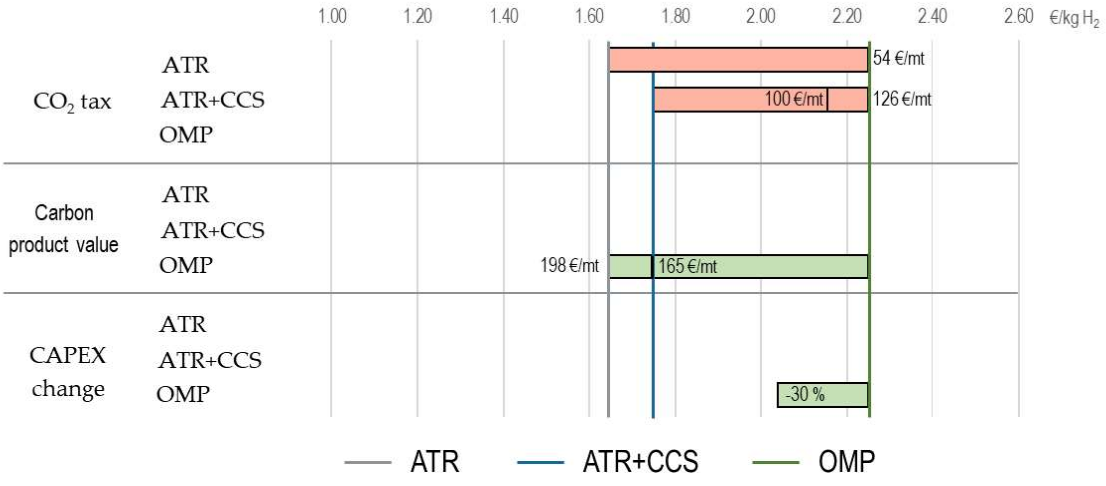

Figure 8.2: *Sensitivity plot for gas price = 35 €/MWh and electricity price = 84 €/MWh*

Table 8.38: *Data for sensitivity analysis for gas price = 35 €/MWh and electricity price = 66 €/MWh*

Components					LCOH		
Gas price	Electricity price	CO_2 tax	Carbon product value	CAPEX	ATR	ATR+CCS	OMP
[€/MWh]	[€/MWh]	[€/mt CO2]	[€/mt Cs]	[%]	[€/kg H2]	[€/kg H2]	[€/kg H2]
35	66	33	0	100%	1.97	1.82	1.97
35	66	69	0	100%	2.37	1.97	1.97
35	66	50	-26	100%	2.16	1.89	1.89
35	66	0	-91	100%	1.61	1.70	1.70
35	66	0	-121	100%	1.61	1.70	1.61
35	66	0	-64	70%	1.61	1.70	1.61

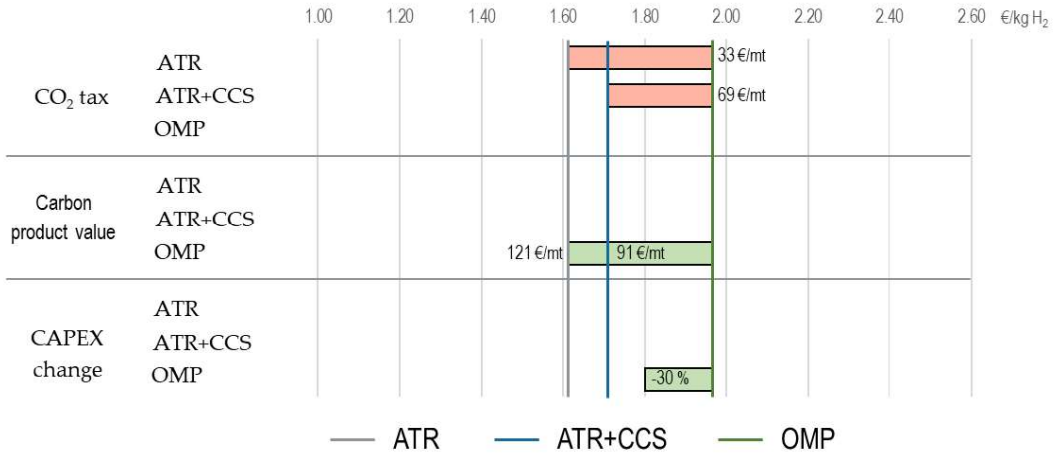

Figure 8.3: *Sensitivity plot for gas price = 35 €/MWh and electricity price = 66 €/MWh*

Table 8.39: *Data for sensitivity analysis for gas price = 35 €/MWh and electricity price = 50 €/MWh*

Components					LCOH		
Gas price	Electricity price	CO_2 tax	Carbon product value	CAPEX	ATR	ATR+CCS	OMP
[€/MWh]	[€/MWh]	[€/mt CO_2]	[€/mt C_s]	[%]	[€/kg H_2]	[€/kg H_2]	[€/kg H_2]
35	50	13	0	100%	1.72	1.69	1.72
35	50	21	0	100%	1.81	1.72	1.72
35	50	10	-14	100%	1.69	1.68	1.68
35	50	0	-28	100%	1.58	1.64	1.64
35	50	0	-48	100%	1.58	1.64	1.58
35	50	0	-20	70%	1.58	1.64	1.58

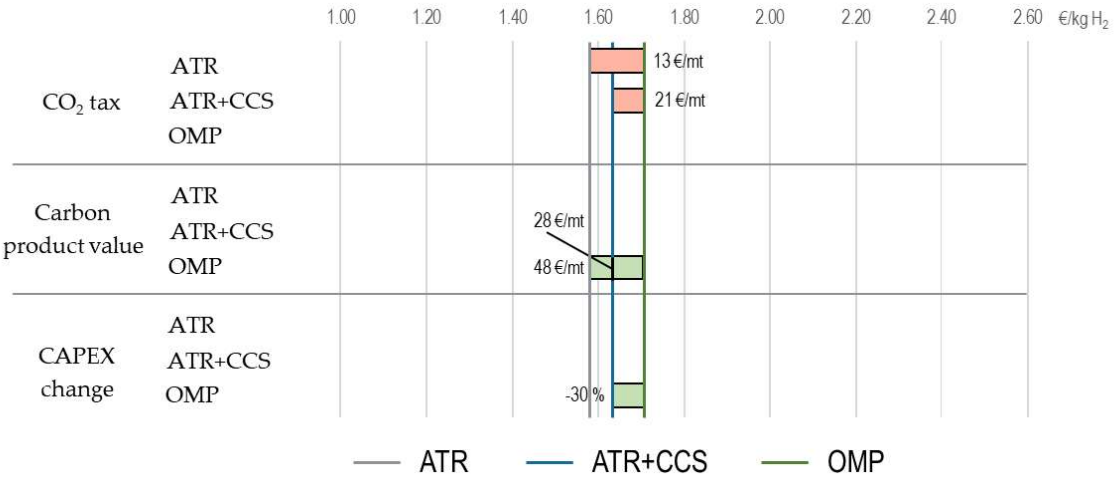

Figure 8.4: *Sensitivity plot for gas price = 35 €/MWh and electricity price = 50 €/MWh*